NORTHWESTERN UNIVERSITY

Computational Investigations into Plasmonic Excitations, Catalytic Reactions and Surface Doping

A DISSERTATION

SUBMITTED TO THE GRADUATE SCHOOL

IN PARTIAL FULFILLMENT OF THE REQUIREMENTS

for the degree

DOCTOR OF PHILOSOPHY

Field of Chemistry

By

Adam P. Ashwell

EVANSTON, ILLINOIS

September 2017

© Copyright by Adam P. Ashwell 2017

All Rights Reserved

ABSTRACT

Computational Investigations into Plasmonic Excitations, Catalytic Reactions and Surface Doping

Adam P. Ashwell

The tools of computational chemistry allow researchers to gain insight into chemical systems that would be difficult or impossible to gain experimentally. This dissertation discusses the application of several of these computational tools to chemical systems of interest. First, we present several studies of plasmon resonance in Ag nanoclusters using time-dependent density functional theory. We demonstrate the effect of ligand-protection on plasmonic behavior, and then introduce a new method for identifying and analyzing plasmons in computational results and apply that method to a series of nanorod-like ligand-protected Ag clusters to study size-dependence of ligand effects. These studies afford us insight into optical properties for systems that would be nearly impossible to synthesize and measure experimentally. Second, we present a study of the possible reaction pathways for hydrogenation of CO on a Ni(110) surface, with and without the presence of subsurface hydrogen. This reaction pathway study allows us to look in detail at individual chemical processes that would be difficult or impossible to study experimentally. And finally, we present a study of surface doping of black phosphorus with Lewis acids, in which we predict the doping effects of a number of Lewis acid adsorbates and identify several promising candidates for further experimental study.

Acknowledgments

I would first like to thank my two research advisors, George Schatz and Mark Ratner, for their tremendous support, guidance, and patience. I was slow to adapt to life and work as a graduate student, but Mark and George stuck with me. These two men are giants in their fields, and after five years working with them at Northwestern I fully understand why. I would also like to thank my committee members Igal Szleifer and Tamar Seideman, whose time, effort, and insight have been very valuable to me during my career at Northwestern.

The Northwestern Chemistry community is a friendly, supportive, and collaborative one, and I have been very fortunate to be a part of it. My many colleagues in theoretical chemistry have been extremely helpful to me. I owe a particular debt of gratitude to Drs. Sharani Roy, Lindsey Madison, and Rebecca Gieseking. Without the enormous help and support each of them gave me, and their incredible patience as I pestered them with questions day in and day out, I would certainly never have gotten this far as a graduate student. I would also very much like to thank Dr. Wei Lin, who has taught and helped me a great deal.

I am very grateful to my parents for their support and guidance, both in the context of graduate school and simply life as an adult. My brother Benjamin has also been a great help to me, encouraging me, advising me, and teaching me. For the three years we overlapped at Northwestern it was a great pleasure working on the same floor and living in the same building as him. But don't tell him I said that.

And finally, I would like to thank most of all my lovely wife Megan, without whom I would not have had the strength, resolve, or support to come this far.

Table of Contents

List of Tables

List of Figures

CHAPTER 1

Introduction

Computational chemistry has become a vital and indispensable tool in modern chemistry. This has been propelled by recent rapid advances in computational power as well as the development of numerous computational methods and software packages that have greatly increased the accuracy of results as well as lowered the barrier to entry into the field. Computational chemistry can both complement and supplement experimental work. Armed with various computational models and techniques, researchers can lay the groundwork for experimentalists, modeling the properties of various systems and determining which particular systems, under which particular conditions, are worthy of experimental study. Researchers can also model systems that have already been studied experimentally, exploring the underlying causes of various system properties and helping to characterize the system further. And furthermore, computational chemists can explore systems that would be difficult or impossible to realistically synthesize or measure, gaining insight into phenomena that could not be otherwise studied.

In this work, we apply several variants of the density functional theory (DFT) computational model to important problems, each with a different motivation and relationship to experiment. We first address the nature of localized surface plasmon resonances (LSPRs) in small Ag nanoparticles called nanoclusters, or simply clusters. In noble metal nanoparticles, the conduction electron “cloud” can be made to oscillate collectively relative to the particle bulk at some characteristic frequency. The resonant frequency at which this oscillation occurs depends on

various properties of the particle in question, including size, shape, composition, and environment.[1] The sensitivity of plasmon resonance frequencies in nanoparticles to changes in the aforementioned properties gives rise to numerous applications in index-of-refraction and biological sensing, photocatalysis, and optical devices.[2–9] The plasmon resonances of noble metal nanoparticles are relatively well-understood phenomena at most particle sizes, and they can be successfully modeled using a host of classical electrodynamics methods. At small particle sizes, however, classical models break down as ligand and surface effects become increasingly significant, and ab initio quantum mechanical models become necessary. In chapter 2, we present a detailed study of the effects of ligands on the plasmonic excited states of several Ag clusters using DFT and the extension of DFT for studying excited state properties, time-dependent density functional theory (TDDFT). We also present a simple method for identifying and analyzing plasmonic excited states called the plasmonic criteria method (PCM). In chapter 3, we extend and revise PCM into the plasmonic indicator method (PIM), introducing three calculable quantities that together serve as indicators of an excited state's plasmonic character. We then apply PIM to several systems and demonstrate its effectiveness in identifying both dipolar and quadrupolar plasmons, and then we extend these concepts into a simple model for grouping plasmonic excited states together. Finally, in chapter 4, we apply TDDFT and PIM to a series of nanorod-like ligand-protected Ag clusters of varying lengths, exploring the evolution of the plasmonic excited states of these systems with increasing length. These three studies represent the application of computational chemistry to systems and phenomena that are not easily synthesized or measured by experiment, and they serve to give insight into the plasmonic behavior of Ag clusters and particles that could not easily be gained otherwise.

We next address the reaction pathways for hydrogenation of CO on a Ni(110) surface, specifically in the presence of subsurface hydrogen. The hydrogenation of CO is an important reaction process in industrial synthesis, where it plays a role in the Fischer-Tropsch process, the reaction of CO and H_2 to yield various hydrocarbons.[10] It is also an important step in CO_2 capture processes.[11] CO hydrogenation is often Ni-catalyzed, and under different conditions it can yield methane, methanol, or some mixture of the two. One important possible condition is the presence of subsurface hydrogen inside the Ni surface, which may act as a spectator, a reactant, or both. Control of the ratio of methane to methanol produced in this reaction is highly desirable. Thus, in chapter 5 we present a computational study using plane-wave DFT to determine the relative energetics of the various possible reaction pathways for CO hydrogenation on a Ni(110) surface, both with and without subsurface hydrogen. This study serves both as a follow-up on previous work in our research group on CO_2 hydrogenation on Ni(110)[12] as well as a means to better understand experimental results and better predict future experimental results.

Finally, we address surface doping and passivation of black phosphorus-based 2D semiconductors. Black phosphorus has recently become the subject of intense study as a promising 2D semiconductor material. However, black phosphorus surfaces have been found to degrade significantly during continued ambient exposure, greatly lowering the performance of black phosphorus-based devices. Recent work has shown that black phosphorus surfaces can be passivated through aryl diazonium chemistry, both protecting the surface from degradation and improving device performance through doping of the black phosphorus semiconductor.[13] In chapter 6 we present a computational study of passivation and doping of a black phosphorus surface through binding with Lewis acids using plane-wave DFT. The goal of this study is to determine if there are Lewis acids that may perform similarly to or better than the previously-

studied aryl compounds as passivators, dopants, or both, with the results of the study serving as guidelines for experimentalists as to which Lewis acids, if any, are worth studying.

In our pursuit of these goals, we have applied several computational methods, each a form of or outgrowth of DFT. The remainder of this chapter is devoted to a general overview of DFT and TDDFT as they are used throughout this work. Notation and terminology below are primarily adapted from textbooks and review articles from McQuarrie,[14] Burke and Wagner,[15] Marques and Gross,[16] and Payne et al.[17]

1.1 Schrödinger to Hartree-Fock

Like all ab initio electronic structure methods, DFT is, at its core, built upon the Schrödinger equation

$$\mathbf{H}\Psi = E\Psi \tag{1.1}$$

where Ψ is the wave function of a system consisting of nuclei and electrons, E is the energy of the system, and $\mathbf{H}$ is the Hamiltonian operator of the system. In the Born-Oppenheimer approximation, in which the motions of nuclei and electrons are treated separately, the Hamiltonian can be defined as

$$\mathbf{H} = \mathbf{T} + \mathbf{V} + \mathbf{V_{ee}} \tag{1.2}$$

where $\mathbf{T}$ is the kinetic energy, $\mathbf{V}$ is the electron-nuclear potential energy, and $\mathbf{V_{ee}}$ is the electron-electron repulsion energy.

The variational principle dictates that the expectation value of the Hamiltonian satisfies

$$\langle \mathbf{H} \rangle = \frac{\langle \Psi | \mathbf{H} | \Psi \rangle}{\langle \Psi | \Psi \rangle} \geq E_0 \tag{1.3}$$

where the condition $\langle \mathbf{H} \rangle = E_0$ is met only when Ψ is an eigenfunction of $\mathbf{H}$ with eigenvalue E_0. Thus, Ψ need not be known exactly to obtain relatively accurate energies – rather, Ψ can be chosen so as to minimize $\langle \mathbf{H} \rangle$, which should ultimately give a reasonable approximation of the ground state energy of the system. However, for systems of chemical interest this procedure is incredibly costly and impractical.

The Hartree-Fock method allows the above method to be simplified through approximating the form of the electronic wave function as a Slater determinant of spin-orbitals ψ_i:

$$\Psi_{HF} = \frac{1}{\sqrt{N!}} \begin{bmatrix} \psi_1(\mathbf{x}_1) & \psi_2(\mathbf{x}_1) & \dots & \psi_N(\mathbf{x}_1) \\ \psi_1(\mathbf{x}_2) & \psi_2(\mathbf{x}_2) & \dots & \psi_N(\mathbf{x}_2) \\ \vdots & \vdots & & \vdots \\ \psi_1(\mathbf{x}_N) & \psi_2(\mathbf{x}_N) & \dots & \psi_N(\mathbf{x}_N) \end{bmatrix} \tag{1.4}$$

where $\mathbf{x}_i$ contains the spatial and spin coordinates of electron i and N is the number of electrons in the system. This form of the wavefunction ultimately yields the expression

$$E_{HF} = \sum_{i=1}^{N} + \frac{1}{2} \sum_{i,j=1}^{N} (J_{ij} - K_{ij}) \tag{1.5}$$

where H_i treats electron-nuclei Coulombic attraction and kinetic energy for electron i and J_{ij} and K_{ij} are terms that treat the electron-electron Coulombic repulsion and exchange, respectively. The Hartree-Fock orbitals, which are described as a linear combination of orbitals from an orthogonal basis set, are optimized iteratively in a self-consistent approach to yield the lowest possible energy. The energy of the system as a whole can then be calculated by adding E_{HF} to the total potential energy of all nucleus-nucleus interactions, which in the Born-Oppenheimer approximation are constant. Notably, the Hartree-Fock method does not account for electron correlation, which has necessitated the development and usage of various post Hartree-Fock methods to correct this.

1.2 Density functional theory

The bases of DFT are the Hohenberg-Kohn theorems. The first of these proves that the Hamiltonian of an atomic or molecular system, and therefore all other atomic or molecular properties, are unique functionals of the electron density $\rho(r)$:

$$\langle A \rangle = A[\rho(r)] \tag{1.6}$$

The second Hohenberg-Kohn theorem then demonstrates that the energy of the system as determined by the electron density satisfies the variational principle such that

$$E_0 \leq E[\rho(r)] \tag{1.7}$$

As in the Hartree-Fock method, this relationship allows for self-consistent calculation of both ground state energy and electron density starting from some trial density. However, this calculation is greatly simplified relative to the Hartree-Fock case, as instead of a wave function with $3N$ spatial variables an electron density with only three spatial variables is used.

To improve the accuracy and applicability of DFT for chemical systems, Kohn and Sham introduced orbitals into DFT. This is achieved by mapping the true problem, that of a system of interacting electrons in some external potential, onto a system of non-interacting electrons in an effective potential that has the same density as the interacting system. The energy of such a system can be written as

$$E = T_s[\rho] + E_{eN}[\rho] + J[\rho] + E_{xc}[\rho] \tag{1.8}$$

where T_s, E_{eN}, and J can all be solved exactly for this non-interacting system, but E_{xc} can only be solved exactly using some unknown functional. Thus, v_{xc}, the exchange-correlation potential, is typically approximated using any one of a large number of available exchange-correlation functionals. The accuracy of a DFT calculation thus often depends on choice of functional as well

as choice of basis set. This form of DFT is sometimes called Kohn-Sham DFT, or KS-DFT. We employ KS-DFT to study the ground-state electronic structure of Ag clusters because KS-DFT provides an excellent combination of efficiency and accuracy for molecular systems.

1.3 Plane-wave density functional theory

To study systems of realistic size with DFT, or to study solid-state systems, one must employ periodic boundary conditions. With a periodic potential, the one-electron solutions to the Schrödinger equation that previously took the form of spin-orbitals now take the form of Bloch states,

$$\varphi_{j\mathbf{k}}(r) = e^{i\mathbf{k}\cdot r}\phi_{j\mathbf{k}}(r) \tag{1.9}$$

where $e^{i\mathbf{k}\cdot r}$ is a plane-wave multiplied by a function $\phi_{j\mathbf{k}}(r)$ with the same periodicity as the potential of the system, **k** is a wave vector, and the energy eigenstates associated with the one-electron Bloch states $\varphi_{j\mathbf{k}}(r)$ are referred to as bands. As the energy of each band is discrete at each of the **k** vectors in the first Brillouin zone, the energies and other properties of the bands, and therefore of the system as a whole, are obtained by integrating over **k** values that correspond to occupied states. This is done by sampling a finite number of **k** vectors in the Brillouin zone. Plane-waves of varying energy (below some defined cutoff energy) are used as a basis set, rather than the localized basis sets used in KS-DFT for discrete molecules as described in 1.2.

Pseudopotentials are used in plane-wave DFT to describe core electrons, which are those electrons in lower-energy orbitals that are localized around atomic nuclei and are relatively insensitive to changes in the atom's environment. A pseudopotential is a parameterized potential applied to the outer electrons that approximates that which would result from interactions with core electrons. The use of pseudopotentials greatly reduces computational cost for plane-wave

DFT and in most systems is necessary to make the problem tractable. This is also true for large systems in discrete KS-DFT. We employ plane-wave DFT, supported by pseudopotentials, in chapters 5 and 6 in our studies of the energetics of molecules bound to solid surfaces, as such systems require periodic boundary conditions.

1.4 Time-dependent density functional theory

DFT can be extended into TDDFT, which can model the response of a molecular system to some time-dependent perturbation, such as an incident laser beam, and can thus be used to model phenomena such as optical absorption. Here we concern ourselves specifically with linear-response TDDFT, or LR-TDDFT, although in this work, as in many others, the terms TDDFT and LR-TDDFT are used largely interchangeably.

TDDFT is built upon the work of Runge and Gross,[18] who derived a Hohenberg-Kohn-like theorem for the time-dependent Schrödinger equation in a many-body system. Runge and Gross demonstrated that, as in the time-independent case, the energy and various properties of a system under the effect of a time-dependent external potential can be determined uniquely by the time-dependent electron density of the system evolving from some initial fixed state. In effect, if the external potential and the initial electron density of the system are known then all other properties can be calculated.

Building from this base, the excitation energies and excited states of the system can be calculated using the approach of Casida.[19] Using the Kohn-Sham orbitals calculated using ground-state KS-DFT, the excited states of the system can be constructed as linear combinations of single particle transitions between those Kohn-Sham orbitals. This requires solving the eigenvalue problem

$$\sum_{jb} \Omega_{ia,jb} F_{jb,I} = \Delta_I^2 F_{ia,I} \tag{1.10}$$

where Δ_I is the excitation energy of the *I*th excited state, *a* and *b* indicate virtual Kohn-Sham orbitals, *i* and *j* indicate occupied Kohn-Sham orbitals, the elements $F_{ia,I}$ correspond to the contribution to the excited state of the transition from the occupied orbital ϕ_i to the virtual orbital ϕ_a, and the elements $\Omega_{ia,jb}$ are given by the expression

$$\Omega_{ia,jb} = \delta_{ij}\delta ab + 4\sqrt{\Delta_{ia}\Delta_{jb}} K_{ia,jb} \tag{1.11}$$

where **K** is the so-called "coupling matrix", the terms of which give the relative degree of coupling between pairs of single particle transitions.

To determine oscillator strengths for excited states, the transition dipole moments d_{ia} must first be calculated for individual single particle transitions. Then the transition dipole moment of the *I*th excited state, d_I, from which oscillator strength can be derived, can be calculated as

$$d_I = \sum_{ia} \sqrt{\frac{2\Delta_{ia}}{\Delta_I}} F_{ia,I} d_{ia} \tag{1.12}$$

We employ TDDFT in chapters 2, 3, and 4 in our studies of the optical response properties of Ag clusters.

CHAPTER 2

A Time-Dependent Density Functional Theory Study of the Impact of Ligand-Protection on the Plasmonic Behavior of Ag Nanoclusters

2.1 Introduction

Noble metal nanoparticles with plasmonic properties have been the focus of extensive study in recent years.[1,20] The localized surface plasmon resonances (LSPRs) of noble metal nanoparticles appear in optical spectra as strong absorption peaks that change in energy in response to changes in properties such as size, shape, composition, and environment,[1,21] giving rise to numerous applications in index-of-refraction and biological sensing, photocatalysis, and optical devices.[2–9] Plasmon resonance also results in the enhancement of the nanoparticle's local electric field, and as such noble metal nanoparticles are used as substrates for surface-enhanced Raman spectroscopy (SERS).[22–26] Other materials such as alkali metals, Group 13 metals, and intermetallic alloys have been shown to exhibit plasmonic performance similar to or even superior to that of noble metals.[27–29] However, gold and silver remain the most commonly used plasmonic materials due to their low reactivity, making them easier to work with as well as particularly well-suited to biomedical applications.[30–33]

Classically, an LSPR in a metal nanoparticle involves excitation of collective oscillations of the conduction electrons with respect to the positively-charged background of the nuclei.[1] The plasmonic behavior of a variety of nanoparticles of different shapes, sizes, and compositions can

be described accurately using classical electrodynamics methods.[1,34–37] The oldest of these methods is Mie theory, based on a solution to Maxwell's equations for a sphere, as presented by Gustav Mie in 1908.[38,39] Solutions to Maxwell's equations have since been extended to accurately describe optical behavior in non-spherical and heterogeneous particles[40–42] using such methods as the discrete dipole approximation (DDA)[43] and the finite-difference time-domain (FDTD) method.[44] While classical electrodynamics can accurately predict LSPRs in a range of nanoparticles, they have been shown to fail in the small particle limit,[45] where quantum effects and the influence of protecting ligands become significant.

These limitations can be overcome, however, using quantum mechanical methods. Plasmonic excited states found using time-dependent density functional theory (TDDFT) have been shown to be correlated with those found by well-established classical methods. Few-atom, bare Ag nanoclusters embedded in solid Ar have been shown experimentally to produce molecule-like absorption spectra (with multiple absorption bands), but these evolve into plasmon-like behavior for 20 atom clusters and larger.[46] The absorption spectra of small tetrahedral Ag clusters calculated by TDDFT show similar molecule-like discrete features for small clusters, but these become more plasmon-like as cluster size increases, with many closely-spaced excited states underlying the plasmon band. Extrapolation of the size-dependent energy of the primary peak in the spectra of tetrahedral nanoclusters to the large particle limit leads to excellent agreement with the LSPRs of tetrahedral nanoparticles calculated by the classical DDA method with empirical dielectric functions.[47] A detailed analysis of the TD-DFT excited states for tetrahedral Ag clusters has shown that even at sizes as small as Ag_{20}, the primary excited state in the calculated absorption

spectrum is a collective excited state of several particle-hole states associated with the conduction electrons, which is a characteristic signature of plasmon excitation.[48]

Guidez and Aikens presented in 2014 a quantum mechanical analysis of plasmonic resonances using configuration interaction (CI) in which they defined a plasmon as a coherent superposition of single particle transitions in which the transition dipole moments of the transitions interfere constructively.[49,50] They describe the wave function of a given excited state in an ideal plasmonic system with *N* single particle states in which all single particle transitions have the same energies and transition dipoles as

$$\Psi^{ex} = A_1\Phi_1 + A_2\Phi_2 + \cdots + A_N\Phi_N \qquad (2.1)$$

where Φ_i are the singly-excited determinants of each interacting state and A_i are weighting coefficients. After calculating the energies and oscillator strengths of the *N* excited states using the CI matrix, they find a single plasmonic state resulting from constructive addition of the contributing single particle transitions and $N - 1$ degenerate zero-intensity non-plasmonic states. The authors have also used a variation of this method to describe the plasmon resonances found in acenes.[51]

Quantum mechanically, an LSPR can be defined in terms of a collective excitation of conduction electrons into the unoccupied portion of the conduction band. In practical terms, a collective excited state is one that is a linear combination of several single particle transitions whose dipole moments interfere constructively.[49,50] Due to the computational expense of *ab initio* methods such as TDDFT, quantum mechanical studies of plasmonic nanoparticles are typically limited to small nanoclusters, usually below 2 nm in diameter. It is possible to treat larger nanoclusters with TDDFT by applying the time-dependent local density approximation (TDLDA) with a jellium model, in which the positively-charged nuclei of the cluster are treated as a positive

charge spread out uniformly over the volume of the cluster.[52–54] However, as this method does not treat molecular structure explicitly, it cannot properly describe or account for the effects of ligands.

Nanoclusters are interesting both as a means to better understand larger, computationally intractable systems and as intriguing systems in their own right. In the nanocluster size regime, the continuous density of states of larger nanoparticles is broken into discrete energy levels, giving rise to new chemical, optical, and electrical properties and therefore new applications.[55–59] While both Au and Ag are plasmonic materials, at small sizes only Ag clusters consistently display plasmonic behavior. The plasmons observed in larger Au structures disappear in the small size limit, as the intraband transitions of Au clusters and nanowires are mixed with interband transitions, resulting in localized excited states that do not show the dependence on cluster size and shape that is characteristic of plasmons.[60–64] In contrast, plasmons have been observed in Ag clusters as small as Ag_{10}.[47,48,65] Given the computational expense of *ab initio* methods like TD-DFT, it is far more practical to study plasmons in small Ag clusters than in Au clusters large enough for plasmons to emerge.

Ligand-protection is an important factor to take into account in characterizing plasmon behavior. Experimentally, ligand-protected clusters are far more easily synthesized and measured than bare clusters, and at small sizes the impact of ligands on the electronic structure and optical properties of clusters is significant. In a 2010 study, Peng et al.[45] synthesized and measured the absorption spectra of a number of ligand-protected Ag nanoparticles ranging in diameter from roughly 2 to 20 nm. They found that, while classical electrodynamics predicted a blue-shift in the LSPR with decreasing size, the experimental spectra showed a reversal in size-dependence of the LSPR at a turnover point of roughly 12 nm, below which the spectra are strongly red-shifted with decreasing size. Both the location of the turnover point and the degree to which the LSPR of the

Ag nanoparticles redshifts below the turnover point were found to change significantly when the amine ligands were replaced with thiolate ligands. Because ligand effects become stronger with decreasing particle size, we would expect to see very substantial ligand effects in few atom Ag clusters.

Plasmons have been observed in sufficiently-large thiolated Au and intermetallic Au-Ag clusters (that is, clusters with thiol-based ligands),[64,66–73] with plasmons being found to emerge in Au clusters as size increases from smaller clusters up to $Au_{144}(SH)_{60}$ and $Au_{314}(SH)_{96}$.[74] In contrast, most studies of plasmonic behavior in Ag clusters have been focused on bare clusters, rather than the more experimentally-relevant thiolated clusters.[47,48,75–78] One reason for this is that crystallographically-determined structures of thiolated Ag clusters have only recently become available.

In this chapter, we study the electronic structures and optical properties of two bare Ag nanoclusters and their ligand-protected variants using TDDFT. In particular, we examine the impact of ligand-protection on the plasmonic excited states observed in bare clusters. To do this, we employ what we refer to as the plasmonic criteria method (PCM), an analytical method in which we examine intraband, interband, and ligand-to-metal character of excited states, as well as whether or not an excited state qualifies as collective, to identify and analyze plasmonic excited states. We show that the addition of ligands, particularly thiolate ligands, to Ag clusters results in the presence of numerous ligand-to-metal charge transfer excited states in the absorption spectrum, and that these ligand-to-metal excited states are dominant at higher energies. We also show that dielectric screening and ligand field effects associated with ligand-protection can shift and split the Kohn-Sham orbitals of the bare Ag clusters, resulting in large red-shifts in the energies of plasmonic excited states and the splitting plasmons into multiple excited states that are not as

coherently coupled. Lastly, we demonstrate that ligand-protection results in core-localization of the plasmon in small Ag clusters.

2.2 Computational Methods

Ground state electronic structure and geometry optimization were carried out using density functional theory (DFT). The X_α exchange-correlation functional[79] and a double-ζ (DZ) Slater type basis set with frozen cores were used for geometry optimization. TDDFT was used for excited state calculations with the statistical average of (model) orbital potentials (SAOP)[80, 81] functional and an all-electron triple-ζ (TZP) Slater type basis set,[82,83] a level of theory that has been used in several earlier studies of noble metal nanoclusters and nanowires.[66,67,78] Only excited states that were optically allowed by symmetry were calculated. To account for relativistic effects, the zeroth order regular approximation (ZORA) was used.[84–86] Charges were assigned using a grid-based Bader analysis.[87,88] All calculated spectra are shown convoluted with a Lorentzian with a full width at half-maximum (fwhm) of 0.1 eV. Calculations were carried out using the Amsterdam Density Functional (ADF) 2013.01 and 2014.01 programs.[89–92]

2.3 Results and Discussion

2.3.1 Ag_{13}^{5+}

We first consider the electronic structure and absorption spectrum of Ag_{13}^{5+}, which comprises the bare core (with 8 valence electrons) of the $Ag_{25}(SH)_{18}^-$ and $Ag_{25}(NH_2)_{18}^-$ clusters which will be discussed in detail later. The structure of Ag_{13}^{5+} consists of a single central Ag atom surrounded by an icosahedral cage of twelve Ag atoms, as shown in Figure 2.1a. Calculations on the Ag_{13}^{5+} cluster were performed using the D_{5d} symmetry point group, as the I_h point group is not

supported in ADF. The 5+ charge state of Ag_{13} is studied because the resulting Ag_{13} electronic structure has the same number of conduction electrons as the ligand-protected variants (8 conduction electrons), as is described below.

2.3.1.1 Electronic Structure

In Ag clusters, KS orbitals composed primarily of orbitals up to and including 4d are fully occupied, while the set of KS orbitals made up of 5s and 5p orbitals is partially occupied. The calculated electronic structure for the Ag_{13}^{5+} conduction band (Figure 2.2a) corresponds well

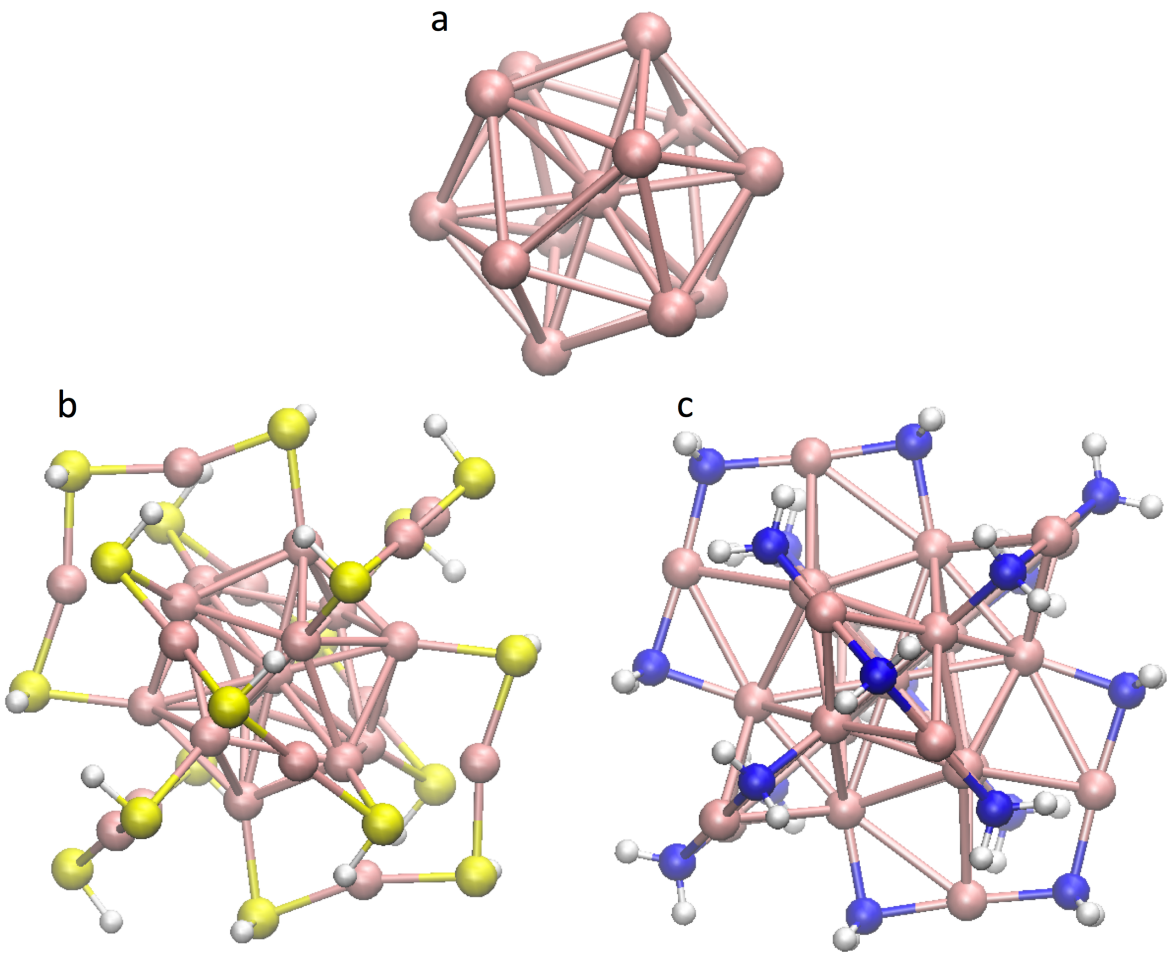

Figure 2.1. Optimized structures of (a) Ag_{13}^{5+}, (b) $Ag_{25}(SH)_{18}^{-}$, (c) $Ag_{25}(NH_2)_{18}^{-}$.

with the superatom model proposed by Walter et al.[93] wherein the valence electrons of metal clusters are found in delocalized superatomic orbitals following the Aufbau rule $1S^2 \mid 1P^6 \mid 1D^{10} \mid 2S^2\ 1F^{14} \mid \ldots$. The 8 valence electrons of Ag_{13}^{5+} fit neatly into this model, resulting in occupied S and P superatomic orbitals and a closed shell. We can identify superatomic KS orbitals as those composed primarily of 5s and 5p atomic orbitals.

Furthermore, we find in Figure 2.2a that the KS orbitals are divided into two regions. All orbitals shown below about -29 eV are dominated by Ag 4d atomic orbital character (with one exception discussed below), while all those above, both occupied and virtual, are dominated by Ag 5s and 5p atomic orbital character. While made up of discrete orbitals, these regions above and below -29 eV correspond to the conduction and valence bands, respectively, found in larger metal particles. Note that the very negative values of the energies of these orbitals arise from the high positive charge of the species being studied.

The occupied 1S superatomic orbital (also a conduction orbital) is found at roughly -31.3 eV in Figure 2.2a, firmly in the middle of the valence band. The next set of superatomic orbitals is found in the triply-degenerate HOMO, corresponding to the 1P orbitals. Beyond this, in the virtual portion of the conduction band, we find the five 1D orbitals at roughly -25.9 eV, the single 2S orbital at -24.8 eV, and the seven 1F orbitals split into groups of three and four orbitals at -23.6 and -22.8 eV, respectively. Due to the Laporte selection rule governing optical transitions for this centrosymmetric system, for optically allowed transitions electrons from the ungerade 1P orbitals can only be excited into the gerade 1D and 2S orbitals.

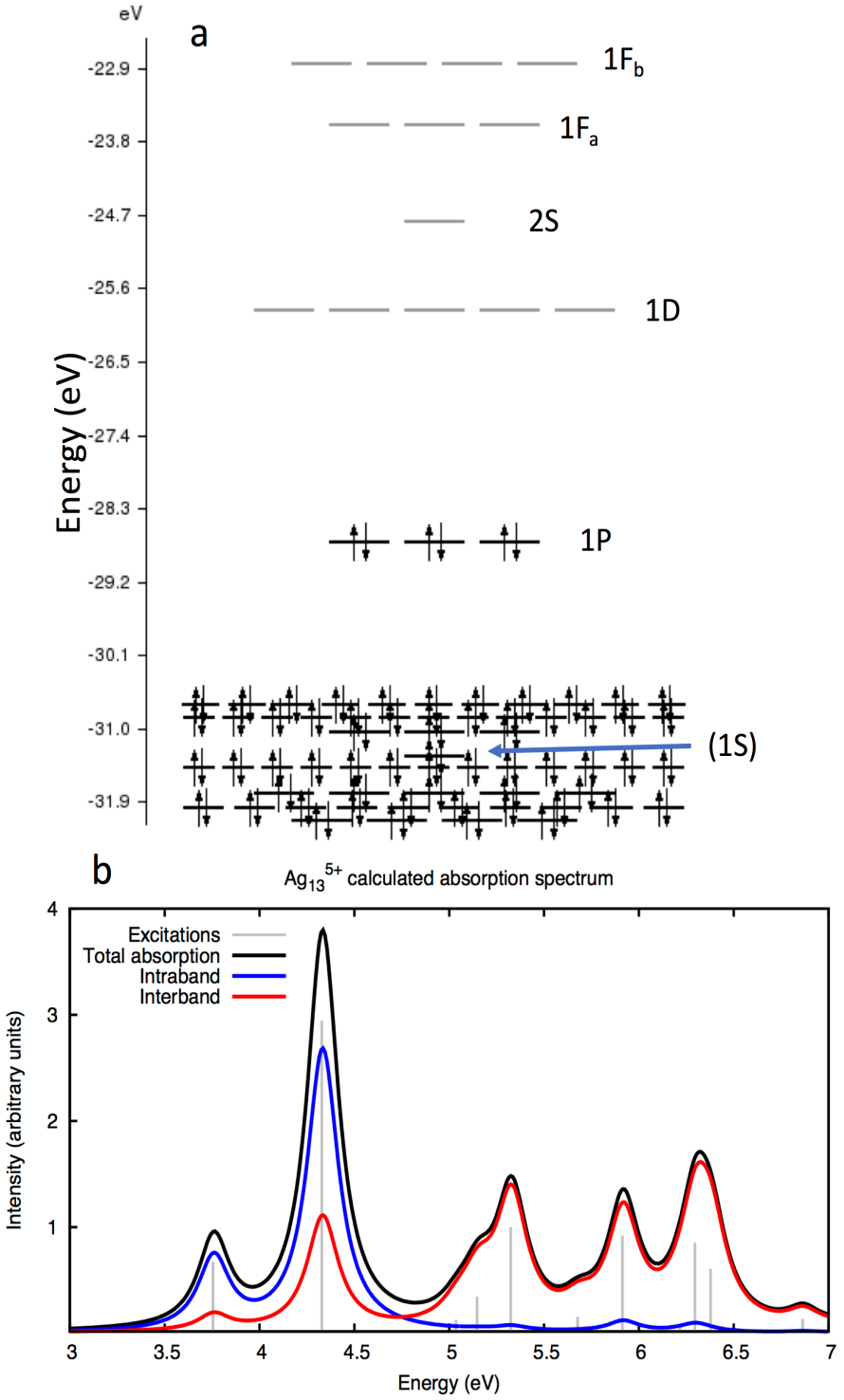

Figure 2.2. (a) The calculated electronic structure of Ag_{13}^{5+}(note that the superatom 1S is embedded in a large number (65) of occupied orbitals associated with the atomic 4d state of Ag), and (b) the calculated absorption spectrum of Ag_{13}^{5+}. The total absorption spectrum is broken down by the characters of the underlying excited states.

2.3.1.2 Optical Properties

We find a number of discrete excited states in the absorption spectrum of Ag_{13}^{5+} (Figure 2.2b). To characterize these excited states as plasmonic or non-plasmonic and make sense of the spectrum, we first analyze the atomic orbital character of the occupied and virtual orbitals involved in each excited state. Excited states in TDDFT are linear combinations of single particle transitions between occupied and virtual KS orbitals. KS orbitals are, in turn, linear combinations of atomic orbitals. Therefore, excited states can be characterized by the atomic orbital characters of the KS orbitals associated with each single particle transition making up the excited state. In Ag_{13}^{5+}, and indeed in all systems studied in this chapter, all virtual orbitals that are accessible at relevant energies are conduction band orbitals of predominantly Ag 5s and 5p character. Because all excited states carry electrons into the conduction band, we need only determine the characters of the occupied orbitals involved to characterize an excited state as either interband ($d \rightarrow sp$) or intraband ($sp \rightarrow sp$), with high intraband character a requirement for a plasmonic excited state.

In addition to the absorption spectrum of Ag_{13}^{5+}, Figure 2.2b shows the spectrum decomposed into interband and intraband contributions. Each peak in the spectrum is actually representative of three nearly-degenerate excited states with mutually orthogonal transition dipole moments, but for simplicity each group of three will be referred to as a single excited state. We see that the first two peaks, at 3.75 and 4.33 eV, are predominantly intraband, while the peaks at higher energies are interband. There are only a few possible single particle transitions low enough in energy and with the correct symmetries to mix around 4 eV – those between the three 1P orbitals and the five 1D orbitals, and between the 1P orbitals and the 2S orbital. Examination of the single particle transition contributions to the two intraband peaks shown in Table 2.1 reveals that the first peak is collective, involving a mixture of 1P to 1D and 1P to 2S single particle transitions. For our

Table 2.1. Transitions contributing to important excited states in Ag_{13}^{5+}. An interband excited state at 6.38 eV is also shown here for the sake of comparison. The five single particle transitions that most contribute to each excited state are given.

Energy (eV)	Transition	Weight
3.75	1P → 2S	0.420
	1P → 1D	0.323
	1P → 1D	0.215
	Valence band → 1D	0.014
	Valence band → 1D	0.002
4.33	1P → 2S	0.542
	1P → 1D	0.180
	1P → 1D	0.119
	Valence band → 1D	0.065
	Valence band → 1D	0.023
6.38	Valence band → 1D	0.735
	Valence band → 1D	0.183
	Valence band → 2S	0.018
	Valence band → 1D	0.014
	Valence band → 1D	0.009

purposes, an excited state is considered collective if no contributing single particle transition has a weight greater than 0.5 and if there are at least three single particle transitions with weights greater than 0.1. Here the highest contribution is from a 1P to 1D transition with a weight of 0.420. The second peak is similar to the first, but with 1P to 2S transitions making up over half of the total contributions to the excited state (with a weight of 0.542). This means that the excited state at 4.33 eV is less collective than that at 3.75 eV. Of course neither of these excited states is

collective in the sense that all possible conduction electrons are involved in the excited state, but if we describe states as collective that satisfy the 0.5 weight rule noted above, then the 4.33 eV state would be somewhere between a plasmon and a non-plasmon. The presence of two peaks rather than one and the differences in contribution from 1P to 2S single particle transitions may be due to the 1.1 eV energy gap between the 1D and 2S orbitals, preventing single particle transitions to each of them from mixing effectively. Another cause may be the differences in angular momentum state, and therefore shape, between the 1D and 2S orbitals.

The analytical method employed above is what we have dubbed the plasmonic criteria method (PCM). The key parts of this analysis are the calculation of intraband character for each excited state, followed by the determination of collectivity of each excited state through the use of criteria regarding the relative weights of the contributing single particle transitions. Using this method, if an excited state has high intraband character and is collective, then we consider that excited state to be plasmonic.

2.3.2 $Ag_{25}(SH)_{18}^-$ and $Ag_{25}(NH_2)_{18}^-$

We next examine the effects of ligand-protection on the electronic structure and optical properties of the Ag_{13}^{5+} cluster. The $Ag_{25}(SPhMe_2)_{18}^-$ cluster has recently been synthesized,[94] but the very-closely related $Ag_{25}(SH)_{18}^-$ structure was first studied as a hypothetical Ag analogue to the $Au_{25}(SH)_{18}^-$ cluster.[67] The structure of $Ag_{25}(SH)_{18}^-$ is based around the icosahedral Ag_{13}^{5+} core, with six $[SH\text{-}Ag\text{-}SH\text{-}Ag\text{-}SH]^-$ oligomeric ligands attached octahedrally as shown in Figure 2.1b. These ligands are so-called "staples"[95], which are seen in many ligand-protected Ag and Au clusters.[72, 96–100] This results in a structure composed of an Ag_{13} core and then twelve additional Ag atoms incorporated in the oligomeric ligands. The other cluster we examine here, $Ag_{25}(NH_2)^-$,

is a purely hypothetical structure in which the thiolate ligands of $Ag_{25}(SH)_{18}^-$ are swapped out for amines, as shown in Figure 2.1c. All calculations on these two clusters were performed using the C_i symmetry point group.

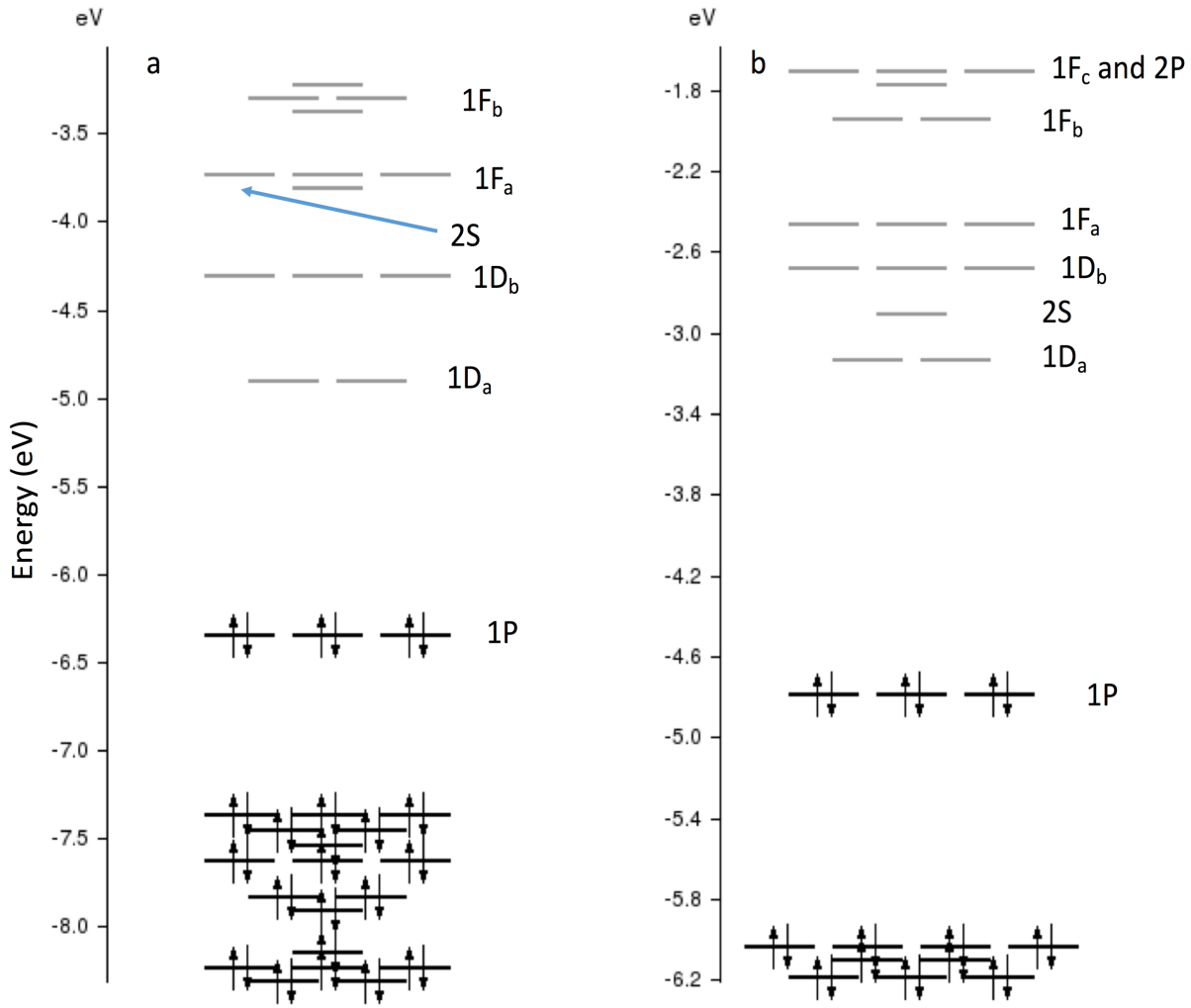

Figure 2.3. Calculated electronic structures of (a) $Ag_{25}(SH)_{18}^-$ and (b) $Ag_{25}(NH_2)_{18}^-$. The orbitals shown here below the 1P orbitals are the upper portion of the ligand band. The valence band is further below in energy.

2.3.2.1 Electronic Structure

The electronic structures of $Ag_{25}(SH)_{18}^-$ and $Ag_{25}(NH_2)_{18}^-$ are shown in Figure 2.3. In both cases, the ligand-protection results in the appearance of a band of ligand orbitals between the

valence band (occupied Ag 4d orbitals) and conduction band 3P HOMO, dominated by either S 3p or N 2p contributions. In Figure 2.3 only the upper portions of these ligand bands are shown. In the thiolated cluster the ligand band spans roughly 2.1 eV, while in the aminated cluster it spans 1.7 eV. The ligand bands of both clusters also have modest contributions from Ag 5s and 5p orbitals.

Table 2.2. Charge analysis and energy-level spacing data for the Ag_{13}^{5+} "family" of clusters. The conduction-valence band gap is the difference in energy between the 3P conduction orbital and the highest-energy valence orbital (orbitals with predominantly Ag 4d atomic orbital character).

	Total Bader charge			
	Ag_{13} (core)	Ag_{12} (ligands)	$(SH)_{18}$ (ligands)	Gap between conduction and valence bands (eV)
Ag_{13}^{5+}	5.00	N/A	N/A	2.01
Ag_{13}	0.00	N/A	N/A	1.53
Ag_{13}^{5-}	-5.00	N/A	N/A	1.37
$Ag_{25}(NH_2)_{18}^{-}$	2.10	4.26	-7.36	2.53
$Ag_{25}(SH)_{18}^{-}$	1.19	2.57	-4.75	3.08

A second effect of ligand-protection in Figure 2.3 is that the HOMO-LUMO gap of the Ag_{13}^{5+} cluster, 2.84 eV, is reduced to 1.65 eV in $Ag_{25}(NH_2)_{18}^{-}$ and 1.45 eV in $Ag_{25}(SH)_{18}^{-}$, and spacings between virtual orbitals are also significantly reduced. These reductions in the conduction band width and spacings can be considered to be a dielectric screening effect of the ligands, where polarization of the ligand electrons by electrons in the conduction and valence orbitals stabilizes those orbitals. Related to this is an increase in the conduction-valence band gap, defined here as the difference in energy between the HOMO and the highest-energy valence orbital (Ag 4d). As shown in Table 2.2, the conduction-valence gap of 2.01 eV in the bare Ag_{13}^{5+} cluster expands to 2.53 eV in the aminated cluster and 3.08 eV in the thiolated cluster. This can be understood in

terms of differential ligand interactions in which the conduction orbitals interact far more with the ligands than do the valence orbitals, as would make sense given that the valence band involves 4d orbitals that are less exposed to the ligands. However, another issue to consider is that the Bader charge analysis shows that ligand-protection also increases the number of electrons in the Ag_{13} core of both $Ag_{25}(SH)_{18}^-$ and $Ag_{25}(NH_2)_{18}^-$, as shown in Table 2.2. To distinguish between the effects of electron addition and those of ligand interactions, we examine the electronic structure of two additional charge states of Ag_{13}, the neutral Ag_{13} cluster and Ag_{13}^{5-}. We see that the simple addition of electrons to the Ag_{13}^{5+} cluster decreases the conduction-valence band gap, so apparently charge addition is less important than ligand interactions. As in the case of the splitting of the 1D superatomic orbitals, the amine and thiolate ligands have similar influence on the electronic structure, though the influence of the amines is smaller.

A third effect of ligand-protection is that the 1D and 2S virtual superatomic orbitals, which are the primary virtual orbitals involved in the plasmonic excited states in Ag_{13}^{5+}, are substantially modified by ligand field effects. In the thiolated cluster the 1D orbitals are split into $1D_a$ and $1D_b$ orbitals that are 0.59 eV apart, and the 2S orbital becomes mixed in with the lower group of 1F orbitals. Note that while the ligands here are arranged octahedrally, the splitting is more akin to that seen in the presence of a tetrahedral ligand field. For the sake of clarity, groups of orbitals that have been split are referred to by their superatomic orbital characters followed by a subscript, as seen in Figure 2.3. In the aminated cluster, the 1D orbitals are split as in the thiolated case, but are separated by only 0.46 eV, and the 2S orbital is shifted down such that it lies between the two sets of 1D orbitals. The splitting observed here is consistent with that seen in previous studies of the $Au_{25}(SH)_{18}^-$ and $Ag_{25}(SH)_{18}^-$ clusters.[66,67,69]

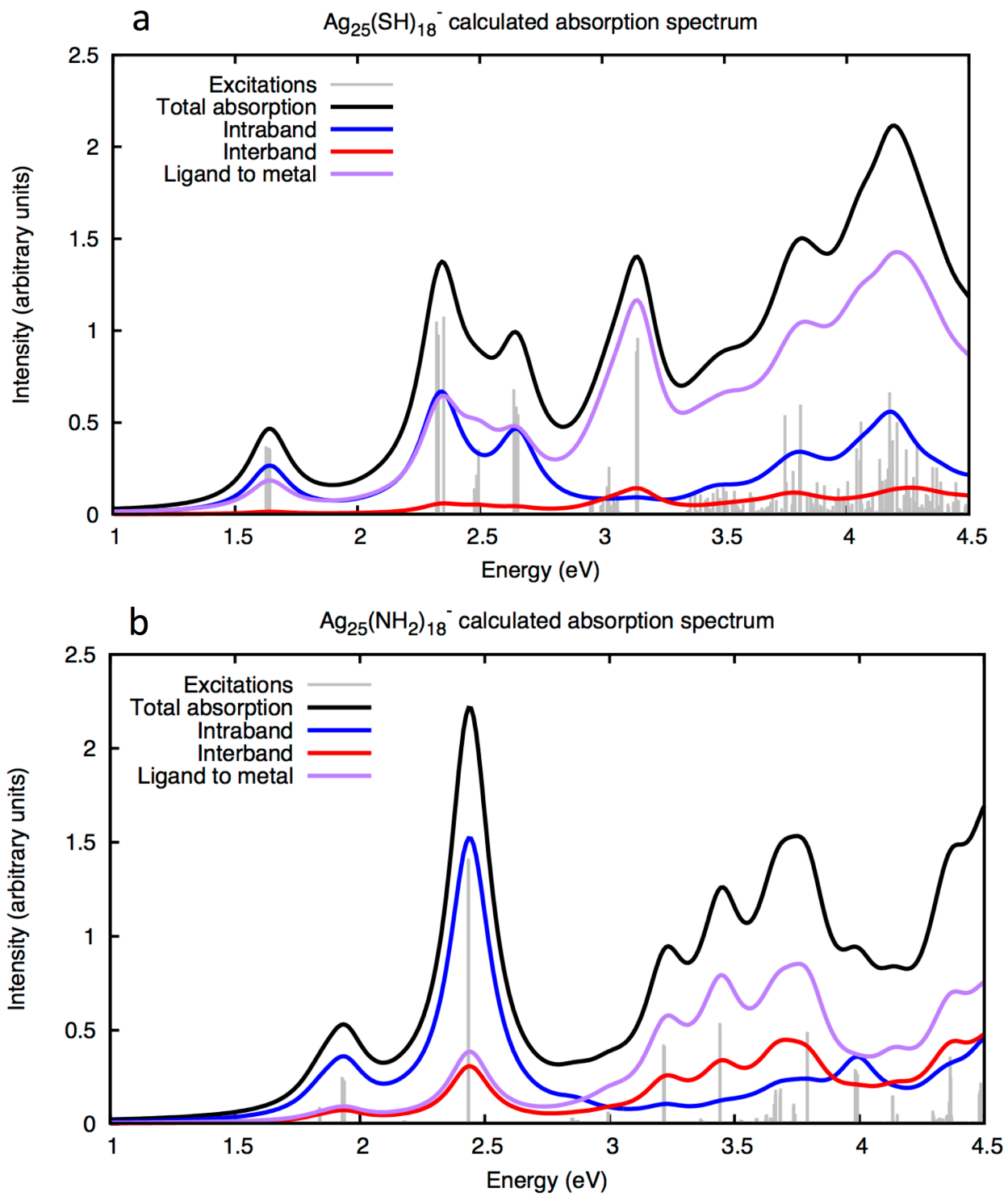

Figure 2.4. Calculated absorption spectra of (a) $Ag_{25}(SH)_{18}^-$ and (b) $Ag_{25}(NH_2)_{18}^-$.

2.3.2.2 Optical Properties

Although superficially similar, the calculated spectra of $Ag_{25}(SH)_{18}^-$ and $Ag_{25}(NH_2)_{18}^-$ (Figure 2.4) are more complicated than that of the bare Ag_{13}^{5+} cluster shown in Figure 2.2. The significant reduction in HOMO-LUMO gap due to ligand-induced dielectric screening pushes the intraband peaks of interest from around 4 eV down to around 2.5 eV, and we also see that a number of peaks arise at higher energies due to ligand-to-metal charge transfer.

Table 2.3. Transitions contributing to important excited states in $Ag_{25}(SH)_{18}^-$.

Energy (eV)	Transition	Weight
1.64	$1P \rightarrow 1D_a$	0.550
	$1P \rightarrow 1D_a$	0.161
	$1P \rightarrow 1D_a$	0.125
	$1P \rightarrow 1D_a$	0.037
	$1P \rightarrow 1D_a$	0.030
2.33	$1P \rightarrow 1D_b$	0.263
	$1P \rightarrow 1D_b$	0.196
	$1P \rightarrow 1D_b$	0.155
	$1P \rightarrow 1D_b$	0.052
	$1P \rightarrow 1D_b$	0.052
2.65	$1P \rightarrow 2S$	0.855
	Ligands $\rightarrow 1D_a$	0.020
	$1P \rightarrow 1D_b$	0.018
	$1P \rightarrow 1D_b$	0.016
	Ligands $\rightarrow 1D_a$	0.010

In the absorption spectrum of $Ag_{25}(SH)_{18}^-$ (Figure 2.4a) we find a large number of sharp peaks. Even at low energies there is a substantial ligand-to-metal contribution in every excited state, which is due to mixing of S 3p orbitals with the Ag 5s and 5p orbitals in the triply-degenerate 1P orbitals as well as some contribution by single particle transitions originating at the top of the ligand band (at -7.3 eV in Figure 2.4a). Regardless of this mixing, we consider peaks that are about evenly intraband and ligand-to-metal to be, for our purposes, intraband.

The intraband excited states of the $Ag_{25}(SH)_{18}^-$ cluster are located at 1.64, 2.33, and 2.65 eV. The component single particle transitions are shown in Table 2.3. The first of these, at 1.64 eV, is a non-collective excited state primarily between the 1P and $1D_a$ orbitals. The second, at 2.33 eV, is a collective excited state primarily between the 1P and $1D_b$ orbitals. These two excited states are equivalent to the plasmonic transition seen at 3.75 eV in the Ag_{13}^{5+} cluster, but lowered in energy by the shrinking of the HOMO-LUMO gap and split in two by the splitting of the 1D orbitals. In contrast to the plasmonic excited state seen in the bare cluster, however, neither of these two excited states in the thiolated cluster have any significant contribution from single particle transitions to the 2S orbital. The third intraband excited state, at 2.65 eV, is almost entirely composed of single particle transitions from the 1P orbitals to the 2S orbital – each of the three excited states making up the peak seen in the spectrum is dominated by a transition from one of the three 1P orbitals to the 2S orbital, and the overall excited state is not collective and, therefore, not plasmonic. This is equivalent to the peak at 4.33 eV in the bare cluster, but with virtually no mixing between transitions to the 2S orbital and transitions to the 1D orbitals. Every excited state higher in energy than those discussed above is predominantly ligand-to-metal, and in fact the spectrum as a whole is dominated by ligand-to-metal excited states. The 1P to 2S single particle transitions in the thiolated cluster do not mix with transitions between the 1P and $1D_a$ or $1D_b$

orbitals, even though the gap between the 2S and $1D_a$ orbitals, 1.1 eV, is unchanged from the corresponding gap in Ag_{13}^{5+}. This may be an effect of dielectric screening. Although the energy gap is the same, the conduction band energies of the thiolated cluster are reduced by the dielectric screening from the ligands, meaning that the 2S may be more weakly coupled to the 1D orbitals than in the bare cluster even though the energy gap is unchanged.

We next look at the absorption spectrum of $Ag_{25}(NH_2)_{18}^-$ (Figure 2.4b), where a number of differences from the $Ag_{25}(SH)_{18}^-$ spectrum are readily apparent, and the spectrum is more similar

Table 2.4. Transitions contributing to important excited states in $Ag_{25}(NH_2)_{18}^-$.

Energy (eV)	Transition	Weight
1.84	$1P \rightarrow 1D_a$	0.212
	$1P \rightarrow 2S$	0.208
	$1P \rightarrow 1D_a$	0.199
	$1P \rightarrow 1D_a$	0.173
	$1P \rightarrow 1D_a$	0.053
1.93	$1P \rightarrow 2S$	0.767
	$1P \rightarrow 1D_a$	0.069
	$1P \rightarrow 1D_b$	0.026
	$1P \rightarrow 1D_a$	0.019
	$1P \rightarrow 1D_a$	0.018
2.43	$1P \rightarrow 1D_b$	0.242
	$1P \rightarrow 1D_b$	0.185
	$1P \rightarrow 1D_b$	0.180
	$1P \rightarrow 1D_b$	0.148
	$1P \rightarrow 1D_a$	0.042

to that of the bare cluster. We see far less ligand-to-metal character spread throughout the spectrum, and even at higher energies the ligand-to-metal character is far less dominant than it is in the thiolated cluster. This difference in the magnitude of the ligand-to-metal contribution to the spectra of $Ag_{25}(SH)_{18}^-$ and $Ag_{25}(NH_2)_{18}^-$ is due to the relative energies of the valence orbitals of the thiolate and amine ligands – the S 3p valence electrons are much closer in energy to the HOMO of the cluster than are the N 2p electrons.

As in the case of $Ag_{25}(SH)_{18}^-$, there are three notable intraband excited states in the $Ag_{25}(NH_2)_{18}^-$ excitation spectrum (the peak just below 2 eV in Figure 2.4b includes two separate excited states). The first intraband excited state, at 1.84 eV, is a plasmonic excited state primarily from the three 1P orbitals to the two $1D_a$ orbitals, but with some contribution from transitions to the 2S orbital, as seen in Table 2.4. The second excited state, at 1.93 eV, is almost entirely made up of transitions from the 1P orbitals into the 2S orbital, and is equivalent to the peaks at 4.33 eV in Ag_{13}^{5+} and 2.65 eV in $Ag_{25}(SH)_{18}^-$. The final intraband excited state is at 2.43 eV, and is mostly from the 1P orbitals to the $1D_b$ orbitals. In this case, the first and third intraband excited states, at 1.84 and 2.43 eV, are equivalent to those at 3.75 eV in Ag_{13}^{5+} and at 1.64 and 3.22 eV in $Ag_{25}(SH)_{18}^-$, which also primarily consists of transitions into the 1D orbitals.

The relationship between the spectra of the aminated and bare clusters is similar to that between the thiolated and bare clusters. In both of the ligand-protected clusters, the first somewhat-plasmonic excited state of the bare cluster, at 3.75 eV, is split into two separate plasmonic excited states due to splitting of the 1D superatomic orbitals. The second somewhat-plasmonic excited state in the bare cluster, at 4.33 eV, ceases to be plasmonic at all upon addition of the ligands. While some of the shifting and splitting of peaks in the spectrum of Ag_{13}^{5+} upon ligand-protection can be explained by splitting and shifting of orbitals, the inability of single particle transitions

close in energy to mix effectively in the spectra of the ligand-protected clusters cannot. In the bare Ag_{13}^{5+} cluster, single particle transitions from the 1P orbitals to the five degenerate 1D orbitals mix to a significant extent with those from the 1P orbitals to the 2S orbital, which is about 1.1 eV higher in energy. However, in the thiolated cluster, the two groups of split 1D orbitals are separated by only about 0.60 eV, and yet there is little mixing between the single particle transitions from the 1P orbitals into each of the two groups. Furthermore, the 2S orbital in the thiolated cluster is about 1.1 eV higher in energy than the $1D_a$ and only about 0.55 eV higher in energy than the $1D_b$ orbitals. And yet, there is essentially no mixing between single particle transitions to the 1D orbitals and those to the 2S orbital. The aminated cluster is a similar case. In $Ag_{25}(NH_2)_{18}^-$, we do see separate peaks for transitions from 1P to $1D_a$, to 2S, and to $1D_b$, but in the transition to the $1D_a$ orbitals there is a non-trivial contribution from single particle transitions into the 2S orbital. This may be due to the relative closeness of these energy levels, as the 2S orbital is only 0.23 eV higher in energy than $1D_a$, and the three $1D_b$ orbitals are only 0.44 eV higher in energy than $1D_a$. In contrast, in the thiolated cluster, where the 2S and $1D_a$ orbitals are separated by 1.1 eV, there is no significant mixing between 1P to 1D and 1P to 2S single particle transitions. As discussed above, this may be due to dielectric screening effects of the ligands on the relevant superatomic orbitals. Also, importantly, nearly all the conduction electrons involved in the plasmonic peaks in the thiolated and aminated clusters come from the icosahedral Ag_{13} core, rather than from the twelve Ag atoms in the six $[SH\text{-}Ag\text{-}SH\text{-}Ag\text{-}SH]^-$ ligands.

2.3.3 Ag_{32}^{14+} and $Ag_{44}(SH)_{30}^{4-}$

2.3.3.1 Electronic Structure

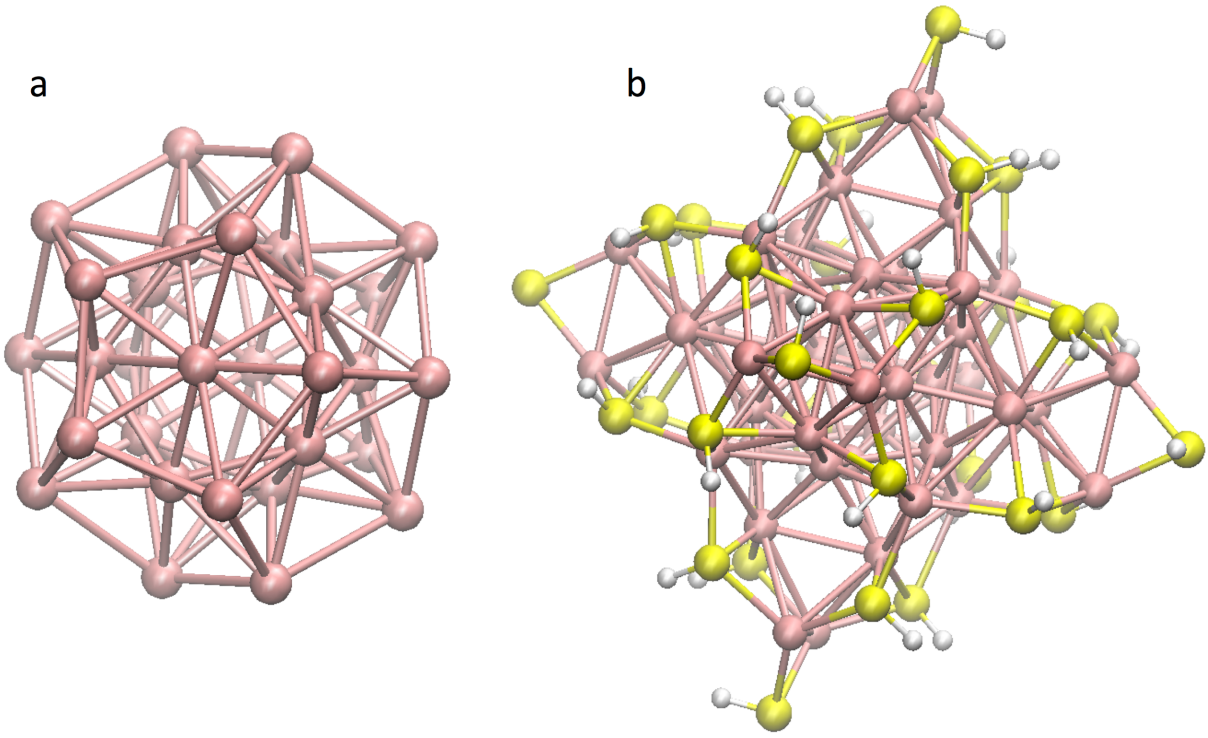

Figure 2.5. Structures of (a) Ag_{32}^{14+} and (b) $Ag_{44}(SH)_{30}^{4-}$.

The last two clusters we examine are Ag_{32}^{14+} and its thiolated form, $Ag_{44}(SH)_{30}^{4-}$. $Ag_{44}(SH)_{30}^{4-}$ was the first all-thiol-protected Ag cluster to be synthesized and have its structure fully crystallographically determined.[101,102] Its structure as well as that of Ag_{32}^{14+} are shown in Figure 2.5. The structure of Ag_{32}^{14+} consists of an icosahedral Ag_{12} core (unlike Ag_{13}^{5+}, there is no central Ag atom) surrounded by an Ag_{20} dodecahedral shell. It has 18 valence electrons, which gives it a closed shell in the superatom model. The thiolated structure, $Ag_{44}(SH)_{30}^{-}$, has six $Ag_2S_5^{3-}$ staple ligands attached octahedrally. The two distinct regions in the structure of Ag_{32}^{14+} allow us to study how ligand-protection affects surface and core Ag conduction electrons differently. All calculations for both clusters were performed using the C_i symmetry point group. As in the case

of the Ag_{13}^{5+} cluster, the highly nonphysical 14+ charge state of Ag_{32} is chosen so as to maintain a consistent number of conduction electrons between the bare and ligand-protected clusters.

As with the Ag_{13}^{5+} cluster, the superatomic orbitals of Ag_{32}^{14+} can be found in its electronic structure (Figure 2.6a). The 1S orbital is found in the middle of the valence band at -53.23 eV, and is not shown. The three 1P orbitals are located on the upper edge of the valence band at -50.63 eV, and have a mixture of conduction and valence band character. The HOMO is comprised of the five nearly degenerate 1D orbitals. The LUMO, at -47.54 eV, is the 2S superatomic orbital, and the seven 1F orbitals are split into a group of four at -47.34 eV ($1F_a$) and a group of three at -45.94 eV ($1F_b$). Lastly, the three 2P orbitals are found at -45.60 eV. It is important to note that both the five occupied 1D orbitals and the virtual 2S orbital are of gerade symmetry, meaning that transitions

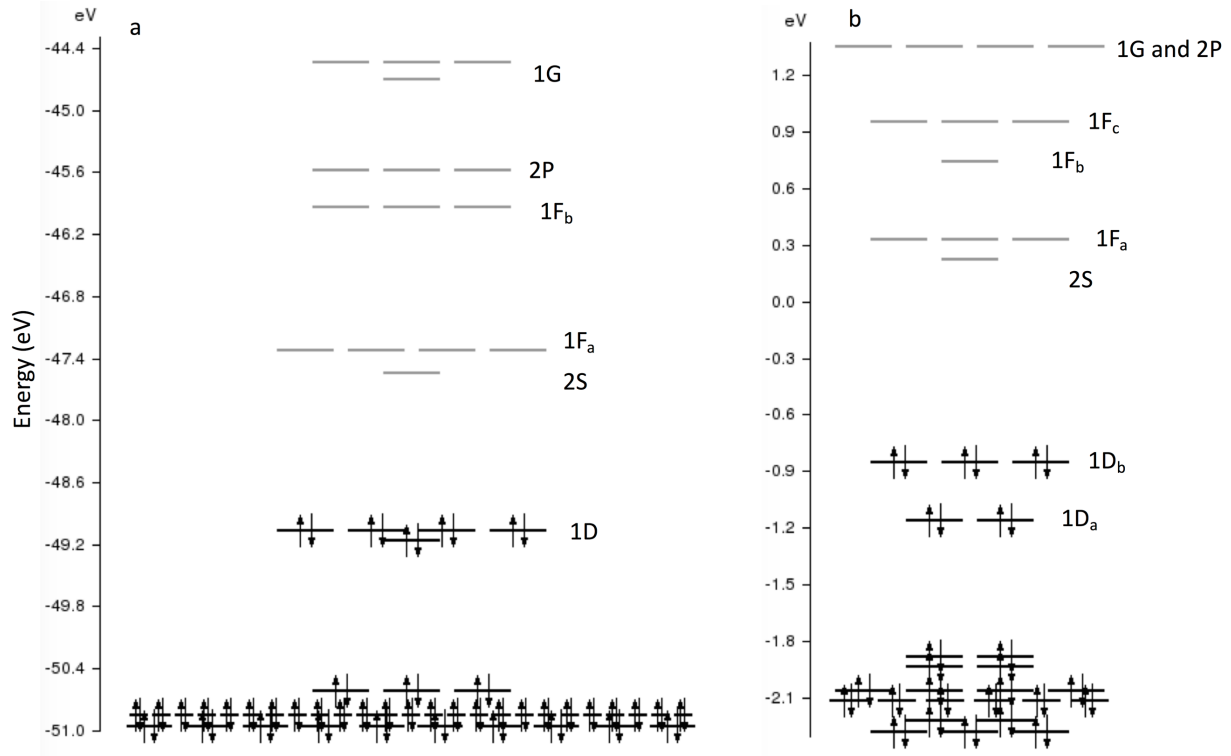

Figure 2.6. Calculated electronic structures of (a) Ag_{32}^{14+} and (b) $Ag_{44}(SH)_{30}^{4-}$.

between them are forbidden. The first virtual orbitals that are accessible to excitation from the 1D orbitals are the ungerade 1F orbitals, followed by the ungerade 2P orbitals.

In the electronic structure of $Ag_{44}(SH)_{30}^{4+}$ (Figure 2.6b) we see that, as was the case for $Ag_{25}(SH)_{18}^{-}$ and $Ag_{25}(NH_2)_{18}^{-}$, the addition of ligands results in the addition of a ligand band between the conduction and valence bands as well as orbital splitting. The five occupied 1D orbitals, which in the bare cluster were just barely split by 0.08 eV, are now split by 0.31 eV. The seven virtual 1F orbitals are now split into three separate groups rather than the two in the bare cluster. And one of the nine virtual 1G orbitals is now relatively low enough in energy that it is below the three virtual 2P orbitals. As before, the addition of ligands increases the gap between the valence and conduction bands (here taken to be between the gap between $1D_a$ HOMO-1 and the 4d valence band), this time from 1.6 eV to 3.0 eV, and lowers the spacings between virtual orbitals.

2.3.3.2 Optical Properties

The calculated absorption spectra of Ag_{32}^{14+} and $Ag_{44}(SH)_{30}^{4-}$ are shown in Figure 2.7. In the bare Ag_{32}^{14+} cluster, there is a single plasmonic excited state at 2.45 eV, composed primarily of single particle transitions from the five 1D orbitals to the four $1F_a$ orbitals, the lowest-energy set of virtual orbitals with the appropriate symmetry to allow a transition from 1D. The single particle transitions that make up this plasmonic excited state (all 1D to $1F_a$) are shown in Table 2.5. In this spectrum intraband excited states are further broken down by region of origin within

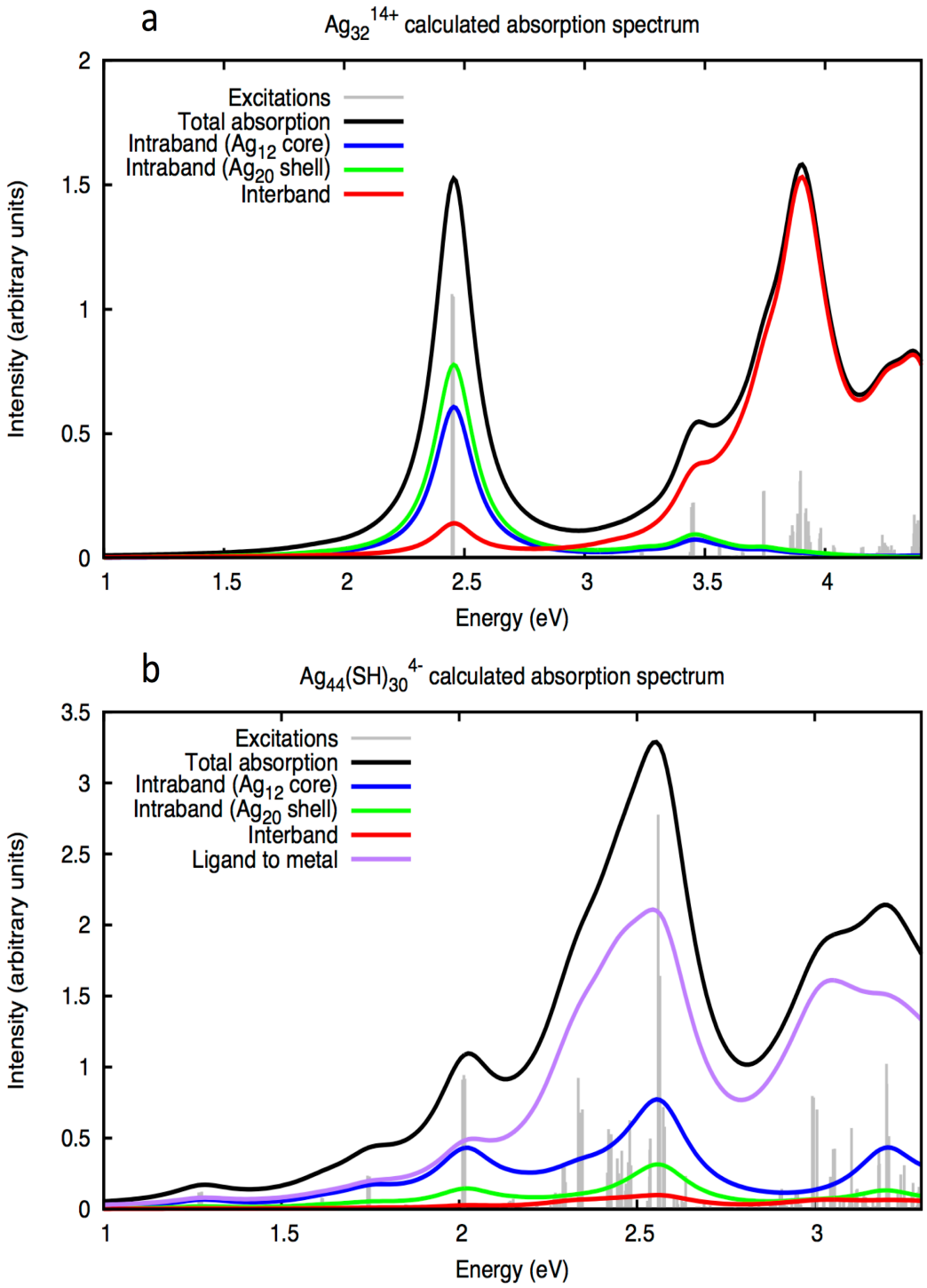

Figure 2.7. Calculated absorption spectra of (a) Ag_{32}^{14+} and (b) $Ag_{44}(SH)_{30}^{4-}$.

Table 2.5. Transitions contributing to important excited states in Ag_{32}^{14+}.

Energy (eV)	Transition	Weight
2.45	$1D \rightarrow 1F_a$	0.128
	$1D \rightarrow 1F_a$	0.119
	$1D \rightarrow 1F_a$	0.102
	$1D \rightarrow 1F_a$	0.074
	$1D \rightarrow 1F_a$	0.056

the cluster – an intraband transition can come from the Ag_{12} core, the Ag_{20} shell, or some mixture of the two. The plasmonic excited state in Ag_{32}^{14+} comes from a nearly even mixture of core and shell, as seen in Figure 2.7a. One reason we see a single plasmonic peak in this spectrum, as opposed to the two seen in that of Ag_{13}^{5+}, may be because of the larger spacing between accessible groups of virtual orbitals. The two groups of 1F orbitals are separated by 1.4 eV, compared to the 1.1 separating the 1D and 2S orbitals in Ag_{13}^{5+}, and we see (Table 2.5) that the $1F_b$ orbitals are not involved in the plasmonic excited state. At energies high enough for electrons from the 1D orbitals to be excited into $1F_b$ orbitals, electrons from the valence band can also be excited into the 2S and $1F_a$, suppressing any potential plasmonic excited state.

Ligand-protection of Ag_{32}^{14+} results in a more complex absorption spectrum for $Ag_{44}(SH)_{30}^{4-}$ (Figure 2.7b). As in the case of the $Ag_{25}(SH)_{18}^{-}$ cluster, we find that ligand-to-metal character dominates the absorption spectrum of $Ag_{44}(SH)_{30}^{4-}$. While Ag_{32}^{14+} has a single plasmonic excited state, $Ag_{44}(SH)_{30}^{-}$ features four of them. The first is at 1.62 eV, and is a mixture of transitions from $1D_b$ to $1F_b$ and from $1D_a$ to $1F_a$, as shown in Table 2.6. The second, at 1.75 eV, is a mixture of $1D_b$ to $1F_b$ and $1D_b$ to $1F_c$. The third plasmonic excited state is at 2.01 eV, made up

Table 2.6. Transitions contributing to important excited states in $Ag_{44}(SH)_{30}^{4-}$.

Energy (eV)	Transition	Weight
1.62	$1D_b \rightarrow 1F_b$	0.225
	$1D_a \rightarrow 1F_a$	0.212
	$1D_a \rightarrow 1F_a$	0.193
	$1D_a \rightarrow 1F_a$	0.109
	$1D_b \rightarrow 1F_b$	0.101
1.75	$1D_b \rightarrow 1F_b$	0.276
	$1D_b \rightarrow 1F_b$	0.109
	$1D_b \rightarrow 1F_c$	0.104
	$1D_b \rightarrow 1F_b$	0.090
	$1D_b \rightarrow 1F_c$	0.086
2.01	$1D_b \rightarrow 1F_c$	0.135
	$1D_b \rightarrow 1F_c$	0.134
	$1D_a \rightarrow 1F_c$	0.133
	$1D_a \rightarrow 1F_c$	0.070
	$1D_a \rightarrow 1F_a$	0.065
2.56	Ligands $\rightarrow$ 2S	0.235
	$1D_a \rightarrow 2P$	0.175
	$1D_a \rightarrow 2P$	0.155
	Ligands $\rightarrow$ 2S	0.068
	$1D_a \rightarrow 2P$	0.035

mostly of single particle transitions from $1D_a$ and $1D_b$ to $1F_c$. And finally, the fourth and most intense plasmonic excited state is at 2.56 eV, a mixture of single particle transitions between the upper part of the ligand band and the 2S LUMO orbital and between $1D_a$ and 2P.

Importantly, we see that the core Ag atoms contribute substantially more than the shell Ag atoms to the plasmonic excited states. In contrast, the two layers contribute about equally to the plasmonic excited state in the bare Ag_{32}^{14+} cluster. This suggests that the presence of ligands localizes some portion of the conduction electrons in the Ag shell, perhaps because of dielectric screening, resulting in a core-localized plasmon not seen in the bare cluster. As with the Ag_{13}^{5+} cluster and its ligand-protected variants, the twelve Ag atoms in the six $Ag_2S_5^{3-}$ ligands do not participate in any plasmonic excited states.

The presence of four plasmonic excited states in $Ag_{44}(SH)_{30}^{4-}$, compared with just one in Ag_{32}^{14+}, appears to have several causes. The first is simply orbital splitting due to ligand field effects. Because the thiolate ligands split the 1D into two groups and splits the 1F orbitals into three groups, a number of single particle transitions that were degenerate in Ag_{32}^{14+} now have different energies. As a result, there are a number of new combinations of occupied and virtual energy levels available. The second is that the presence of thiolate ligands shifts the relative energies of orbitals, lowering energies. For example, the plasmonic peak in the thiolated cluster at 2.56 eV involves intraband transitions into the virtual 2P orbitals. The single particle transitions have energies of about 2.2 eV, whereas in the bare cluster, the same single particle transitions have energies of 3.6 eV. And finally, the increase in the gap between the conduction and valence bands upon ligand-protection, from 1.6 to 3.0 eV due to differential ligand interactions for valence and conduction orbitals, pushes the onset of interband excited states to higher energies, allowing

intraband excited states to higher-energy virtual orbitals to occur without convoluting with interband excited states.

2.4 Conclusions

We have performed DFT and TDDFT calculations on two sets of Ag nanoclusters, both with and without ligand-protection, and we developed and applied PCM to identify and analyze plasmonic excited states in the results of these calculations. The calculated electronic structures of these clusters show that ligand-protection of both the Ag_{13}^{5+} and Ag_{32}^{14+} clusters results in three distinct effects. (1) The highest occupied ligand orbitals show up at energies above the valence band, leading to substantial contribution from ligand-to-metal charge transfer excited states to the spectra, particularly at higher energies. (2) Dielectric screening reduces the splitting of the conduction band orbitals and differential ligand interactions increase the gap between the valence and conduction bands and in most cases reduces the spacings between virtual orbitals. (3) Ligand field effects lead to splitting of superatomic orbitals in the conduction band, in particular the sets of 1D and 1F superatomic orbitals, and this reduces plasmonic character of the lower energy excited states. These factors combine to create multiple plasmonic peaks in the calculated absorption spectra of the ligand-protected clusters, rather than the single plasmonic peaks seen in the bare clusters. The extent to which the ligands split the superatomic orbitals and shift virtual orbital energies was found in the case of Ag_{13}^{5+} to depend on the identity of the ligand. Amine ligands were found to have a smaller impact on the electronic structure of Ag_{13}^{5+} than thiolate ligands due to the lower energy of nitrogen's valence orbitals relative to those of sulfur. This is consistent with the findings of Peng et al.,[45] whose experiments demonstrated a larger red-shift for thiolated Ag nanoparticles than for aminated nanoparticles as diameter was reduced.

The Ag atoms in the oligomeric ligands in each ligand-protected cluster studied were found not to contribute significantly to any plasmonic excited states, nor did the addition of these Ag atoms to the Ag cores result in any increase in the occupancy of the superatomic orbitals. While the plasmonic excited state in Ag_{32}^{14+} is composed roughly evenly of single particle transitions from the Ag_{12} core and Ag_{20} shell, contributions from the Ag_{12} core become dominant in the spectrum of the thiolated cluster. In the case of Ag_{32}^{14+} cluster and its thiolated counterpart, $Ag_{44}(SH)_{30}^{4-}$, ligand-protection was found to localize as well as split the plasmonic excited state seen in the bare cluster.

CHAPTER 3

Developing Analytical Approaches to Identify Plasmonic Excited States

3.1 Introduction

A key yet often overlooked component of the study of plasmons is the ability to identify them in optical spectra. The identification of localized surface plasmon resonances is usually trivial for larger nanoparticle systems, where the dipolar plasmon absorption is typically the most intense peak in the spectrum (although the quadrupolar plasmon can become quite strong as well in some systems).[1] In cases where this is not true, classical electrodynamics methods such as Mie theory and the discrete dipole approximation (DDA) can be used to accurately model the optical behavior of the particle, allowing researchers to compare experimental and calculated spectra to clearly identify experimental plasmonic peaks.

However, in the small-particle or -cluster limit, plasmon identification becomes challenging. At these small sizes, where spectra often have molecule-like features, there may be a number of excited states with significant oscillator strength, all, some, or none of which may be plasmons. Furthermore, as was observed in chapter 2, there may be exited states that are only somewhat plasmonic. Classical electrodynamics methods fail in this size range, as surface and ligand effects have a large impact. These systems can only be properly modeled using quantum mechanical methods, but identification of plasmons in optical spectra calculated quantum-mechanically is decidedly non-trivial.

In the previous chapter, we developed and applied the plasmonic criteria method (PCM) to ligand-protected Ag nanoclusters to study the effects of ligands on plasmonic excited states. In addition to PCM, a number of other plasmon identification methods have been developed for use with quantum mechanical models. One such method, proposed in 2013 by Bernadotte et al.,[103] is based upon the idea that the energies of plasmonic excited states are far more dependent on coupling between single particle transitions than are the energies of non-plasmonic excited states. This dependence on coupling in plasmonic excited states reflects at least in part their high collectivities – that is, the energies of excited states that are made up from substantial contributions from multiple single particle transitions at different energies should be highly dependent on the ability of those single particle transitions to couple to one another. In this method, the authors define electronic excited states as the poles of the external response function

$$\chi_{ext}(r, r', \omega) = \int \varepsilon^{-1}(r, r'', \omega)\chi_{irr}(r'', r', \omega)d^3r'' \tag{3.1}$$

where χ_{irr} is the irreducible response function (i.e. the response to changes in the total potential, rather than just the external perturbation), ω is the angular frequency of the external perturbation, and the dielectric function ε is defined as

$$\varepsilon(r, r'', \omega) = \delta(r - r'') - \int \chi_{irr}(r, r''', \omega)f_{Coul}(r''' - r'')d^3r''' \tag{3.2}$$

where f_{Coul} is the Coulomb kernel. Poles of χ_{ext} can appear either at frequencies corresponding to poles of χ_{irr} or at frequencies where the dielectric function ε has a zero mode. The former are classified as single particle transitions and the latter as plasmons. A primary difference between these two classes of excited states is that the frequencies of plasmons depend on f_{Coul}, while those of single particle transitions do not. The authors performed TDDFT calculations on small

plasmonic systems with a modified definition of ε in which they multiply f_{Coul} by a scaling factor λ. As they scanned λ from 0 to 1, they found that the energies of single particle transitions were largely unchanged, while those of plasmons changed substantially. This approach has been used in a number of studies to investigate plasmonic excited states in metal clusters and nanowires.[60,104,105] However, this method is computationally expensive, as it often requires dozens of TDDFT calculations to be performed on a single system of interest to get useful information. Furthermore, it has not yet been applied to ligand-protected clusters.

Another interesting analytical method for plasmon identification comes from Gieseking et al.[106] In this work, the semiempirical INDO method is used to calculate orbital energies rather than DFT, and then excited state energies and properties are calculated using configuration interaction (CI). While the use of INDO results in lower quantitative accuracy than DFT, it is far cheaper computationally and is shown to give qualitatively accurate results. The authors demonstrate for a number of bare Ag clusters that the plasmonic excited states can be identified by their dipole additivity. Dipole additivity is a metric of the degree to which the transition dipole moments of the configurations contributing to an excited state interact additively, and can be defined as

$$\gamma = \frac{\sum_i \mu_i}{\sum_i |\mu_i|} \tag{3.3}$$

where γ is dipole additivity and μ_i is the transition dipole moment of the *i*th single particle transition. One obvious limitation of dipole additivity as a metric for plasmonic character is that dipole additivity will always be high for an excited state that is dominated by one single particle transition. INDO/CI itself is a promising computational method for generating qualitatively significant optical spectra of metal clusters at a fraction of the cost of TDDFT, and has been used recently to study solvatochromic shifts, electrochemical charge transfer, and the chemical

mechanism in surface-enhanced Raman spectroscopy.[107–109] However, in spite of its high computational cost, TDDFT remains a far more quantitatively accurate model.

While most studies of plasmons concern only dipolar plasmons, in which the entire "cloud" of conduction electrons oscillates along some axis, quadrupolar plasmon resonances are also of interest. While for small nanostructures they are optically dark, they can still be excited by near-field radiation.[110] Quadrupolar plasmons have been found to give stronger enhancement for surface-enhanced Raman spectroscopy[111] as well as greater sensitivity for index-of-refraction based sensing.[112,113] Quadrupolar excited states can be identified by calculating and examining transition quadrupole moments in addition to transition dipole moments. Notably, quadrupolar plasmons have been identified in Ag nanorods using the CI method detailed in the previous paragraph.[106]

In chapter 2, we presented a study of ligand effects on plasmons in Ag clusters using a method we had developed to analyze spectra calculated with TDDFT that we dubbed PCM. We identified plasmons using two criteria: (1) a plasmonic excited state involves primarily conduction electrons, and must therefore be primarily an intraband excited state, and (2) a plasmonic excited state must be collective. Intraband character for excited states was calculated by determining the atomic orbital characters of individual KS orbitals, and then using those to determine the atomic orbital characters of excited states that consisted of linear combinations of single particle transitions between those KS orbitals. The collectivity of an excited state was determined by holding the percentage contributions of single particle transitions to the excited state against a set of somewhat arbitrary criteria: no single particle transition should contribute more than 50% to the excited state, and at least three single particle transitions should contribute 10% or more to the

excited state. Using this methodology, we were able to identify and analyze plasmons in systems both with and without ligands.

However, PCM, which we used previously, has several significant shortcomings which severely limit its utility in the analysis of spectra of larger and more complex structures than those studied in chapter 2. Indeed, when we began our study of plasmons in so-called "box clusters", which is presented in chapter 4, we found that our method did not scale well to these systems. Our analytical method was thus heavily revised to address the shortcomings we found.

In this chapter, we present our improved analytical method for plasmon identification, in which we use several quantifiable indicators of plasmonic character together to identify plasmonic excited states in calculated optical spectra. This is referred to as the plasmonic indicator method (PIM), in contrast with the plasmonic criteria method (PCM) introduced in chapter 2. We discuss how we replaced the concept of intraband character with that of superatomic character, how we introduced a quantification for collectivity, and how we developed a new metric that appears to be strongly related to plasmonic character called "coupling range". We then revisit the calculated absorption spectra of Ag_{13}^{5+}, $Ag_{25}(SH)_{18}^{-}$, $Ag_{25}(NH_2)_{18}^{-}$, Ag_{32}^{14+}, and $Ag_{44}(SH)_{30}^{4-}$. We then show that this method can also be used to identify quadrupolar plasmons in Ag nanorods in addition to the dipolar plasmons previously discussed. Finally, we present a simple analytical model for grouping plasmonic excited states together to measure the transition of plasmonic peaks from molecular to classical with increasing cluster size.

3.2 Methods

All DFT and TDDFT calculations in this chapter were performed using the ADF software package, with versions 2013.01 and 2014.01[89–92] used for the bare and ligand-protected clusters

presented in 3.3.1 and version 2016.103[114] used for the nanorod and tetrahedral clusters presented in 3.3.2 and 3.3.3. For all systems the X_α exchange-correlation functional[79] and a double-ζ (DZ) Slater type basis set with large frozen cores were used for geometry optimization.[82,83] As the results presented in sections 3.3.1, 3.3.2, and 3.3.3 were all obtained as parts of separate studies, each set of results was calculated using a different level of theory. For 3.3.1 the SAOP model potential[80,81] was used with a TZP basis set. For 3.3.2 the LB94 model potential[115] was used with a DZ basis set with a [$1s^2$-$3d^{10}$] frozen core for Ag. And for 3.3.3 the PBE exchange-correlation functional[116] was used with a DZ basis set with a [$1s^2$-$4p^6$] frozen core for Ag. For all cluster calculations we accounted for relativistic effects using ZORA.[84–86]

3.2.2 Intraband and superatomic character

One of the key distinguishing features of a plasmonic excited state is that it is an excitation of the delocalized conduction electrons, and thus it is important to characterize the electrons involved in a given excited state. As discussed above, our previous method, PCM, involved the calculation of a quantity called "intraband character" for each excited state. In that implementation, each KS orbital's atomic character was calculated. An orbital's "conduction character" was equal to the sum of the percentage contribution for all contributing Ag 5s and Ag 5p orbitals, "valence character" was the same but for Ag 4d character, and "ligand character" was again the same but for ligand valence orbitals (for thiolate ligands S 3p, and for amine ligands N 2p). In practice, few or no orbitals have 100% conduction, valence, or ligand character, but instead have some mixture of characters.

While intraband character is useful, it is simply a roundabout way to get at what is truly significant, which is the "superatomic character" of an excited state. As described in the previous chapter, superatomic orbitals are conduction orbitals in metal clusters that are delocalized over the entire cluster. In near-spherical clusters, like those studied in the previous chapter, superatomic orbitals look very similar in shape to atomic orbitals. In practice, every orbital in the conduction band is also superatomic. However, in some cases it can be difficult to judge where the conduction band begins.

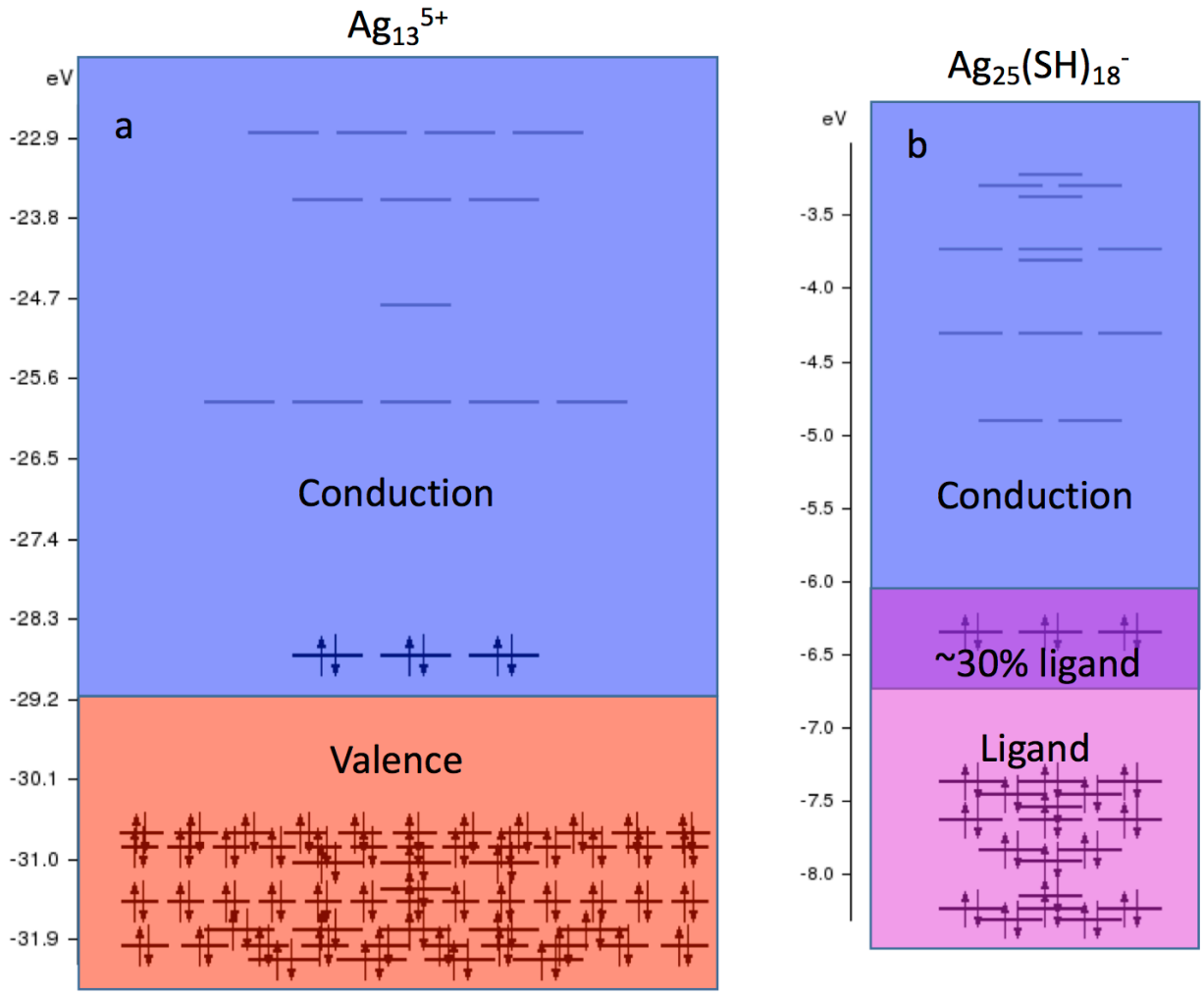

Figure 3.1. Portions of the orbital energy diagrams of (a) Ag_{13}^{5+} and (b) $Ag_{25}(SH)_{18}^{-}$ with regions dominated by one type of atomic character marked with colored rectangles.

Mixing of atomic orbital characters in KS orbitals does not pose a significant problem when studying bare clusters, such as Ag_{13}^{5+} and Ag_{32}^{14+}, as the conduction and valence bands are typically quite distinct, and thus the superatomic orbitals also have very high conduction characters. However, when ligands are present, there is significant mixing between the ligand and conduction bands, as well as the ligand and valence bands, as illustrated schematically in Figure 3.1, where we compare the separations between the conduction band and the valence or ligand band in Ag_{13}^{5+} and $Ag_{25}(SH)_{18}^{-}$. This presents a challenge, as it means that the superatomic orbitals, which lie in the conduction band, have some significant amount of ligand character. This in turn means that excited states originating from superatomic orbitals are not considered wholly intraband. As such, it can be difficult to distinguish between excited states from superatomic orbitals and excited states from the ligand band using PCM. While this method was successful in our analyses of the $Ag_{25}(SH)_{18}^{-}$, $Ag_{25}(NH_2)_{18}^{-}$, and $Ag_{44}(SH)_{30}^{4-}$ clusters, each excited state of interest in the calculated spectra of these clusters was checked by hand to determine which orbitals its electrons came from. This can become impractical with more complex spectra and electronic structures, as will be seen in chapter 4. Thus, it is necessary to replace intraband character with a more generally useful metric that can clearly distinguish between superatomic and non-superatomic excited states.

Our solution to this problem is to introduce the concept of "superatomic character." Rather than calculate conduction, ligand, and valence characters for each KS orbital, we instead simply classify each KS orbital as either superatomic or not superatomic. Then the superatomic character

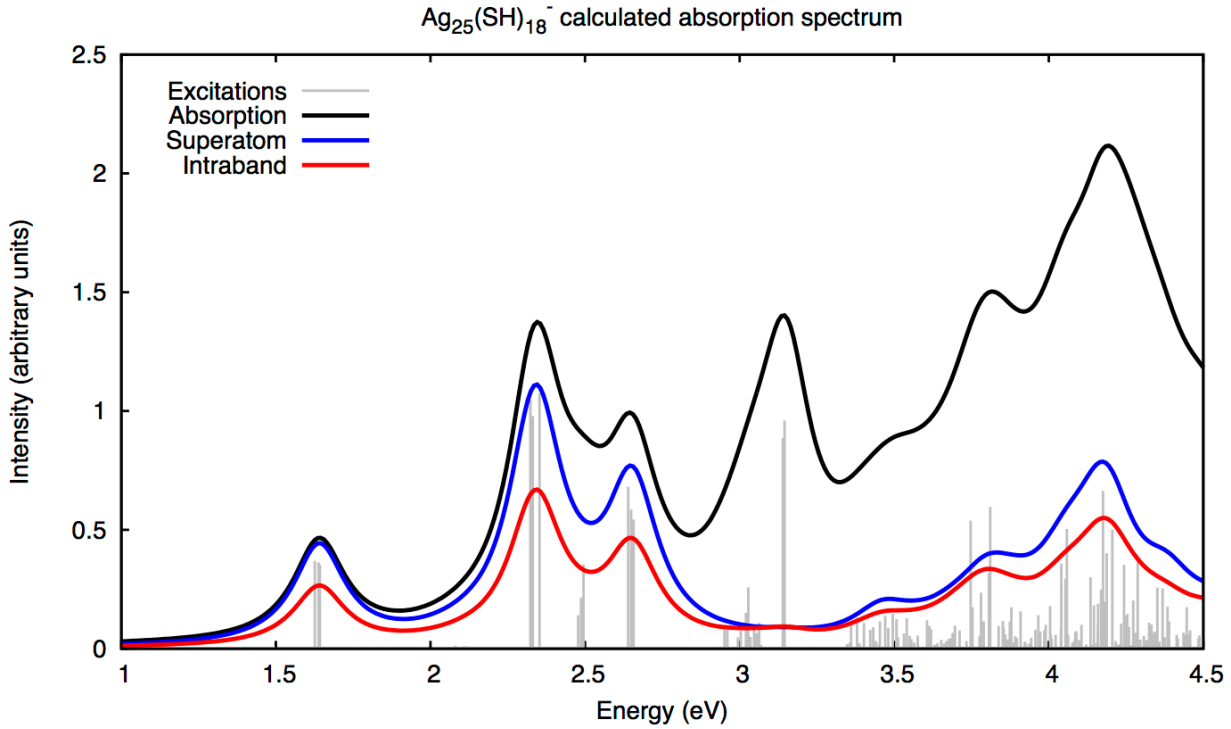

Figure 3.2. Calculated absorption spectrum of $Ag_{25}(SH)_{18}^-$ with both superatomic character and intraband character plotted.

of each excited state is calculated by adding together the percentage contributions of its single particle transitions that originate in superatomic orbitals.

However, identifying superatomic orbitals can present a challenge. For large clusters, this can mean visual analysis of many dozens of orbitals. For the near-spherical clusters previously studied, superatomic orbitals look very similar in shape to atomic orbitals, and are thus easily identifiable. But for clusters that are not near-spherical, superatomic orbitals can be more difficult to identify, as their shapes are particular to the shape of the cluster. In practice, though, we have discovered that superatomic orbitals can in fact be identified via their conduction character, which we have defined as equal to the sum of the percentage contributions of all Ag 5s and 5p atomic orbitals to the orbital in question. For every cluster we have studied, we have found that every visually-identified superatomic orbital also had a conduction character of at least 40%, and that no

non-superatomic orbitals in relevant energy ranges had a conduction character greater than 40%. Thus, visual orbital analysis may only be necessary when working with cluster shapes not previously studied.

To illustrate the difference between intraband and superatomic character, we present in Figure 3.2 the calculated absorption spectrum of the $Ag_{25}(SH)_{18}^-$ cluster with both intraband and superatomic character plotted. We see in this case that superatomic character is almost uniformly higher than intraband character, but most importantly we see that the peaks at 1.64 and 2.33 eV are both clearly excited states from superatomic orbitals (and therefore the conduction band). When using intraband character, it is difficult to quickly determine that these excited states are primarily from the conduction band, and one must investigate the individual single particle transitions involved.

3.2.3 Collectivity

The next indicator in PIM, collectivity, addresses the requirement that a plasmon be a collective excited state. Previously, the determination of an excited state's collectivity was made using a series of criteria which served as cutoffs: (1) no single particle transition dominates the excited state, meaning no transition contributes more than 50%, and (2) multiple single particle transitions contribute significantly to the excited state, meaning at least three transitions contribute 10% or more. The numbers involved were arbitrary, but the criteria were helpful in defining collective excited states.

However, many excited states are either just barely collective or just barely not collective, but are considered either fully collective or fully not collective by this method. In practice, individual excited states of interest were analyzed by hand, and those near the collectivity cutoff

criteria were noted as such. With larger and more complex clusters, though, there may be too many significant excited states to reasonably do this sort of specific analysis. Furthermore, it is difficult to directly compare the collectivities of excited states when collectivity depends on both of the criteria described above. To solve these problems, we adopted the transition inverse participation ratio (TIPR) proposed and used by Casanova et al.[104] The TIPR, referred to hereafter simply as the collectivity, is defined as:

$$\tau = [\sum_{i=1}^{n_{occ}} \lambda_i^4]^{-1} \tag{3.4}$$

where τ is collectivity and λ_i is the coefficient of the *i*th single particle transition in the linear combination that makes up the excited state. The minimum possible value for collectivity of an excited state is 1.0, when there is only one single particle transition contributing to the excited state, and the maximum value is *n* when there are *n* single particle transitions all contributing equally. As this is a relatively new metric there are no established guidelines for its interpretation. However, based on our experience, we typically consider a collectivity between 1.0 and 2.0 to be extremely low, from 2.0 to 3.0 to be somewhat low, from 3.0 to 5.0 to be somewhat collective, from 5.0 to 8.0 to be collective, and greater than 8.0 to be extremely collective. These numbers are arbitrary, but they give a sense of the relative meanings of different collectivity values.

3.2.4 Coupling range

We also add one new component to PIM, which is the calculation of a quantity we have termed "coupling range" for an excited state. One of the primary challenges in applying our analytical method to complex spectra is the sheer number of excited states that must be considered. When working through these excited states, neither superatomic character nor collectivity alone

serve as good indicators of plasmonic character, as there are many excited states with high superatomic character but low collectivity and many with high collectivity but low superatomic character. Furthermore, some excited states that have high superatomic characters and collectivities have very low oscillator strength, and are therefore of little interest. We endeavored to find another indicator of plasmonic character that would help us to sort through the hundreds of excited states in each spectrum, and we thus developed the new concept of coupling range.

In the Casida formalism of TDDFT,[19] the energies of excited states are not equal to KS orbital energy differences, but are instead calculated by combining single particle transitions using coupling matrix elements, which depend on the various orbitals involved in a given pair of single particle transitions as well as the Coulomb and exchange-correlation kernels. This dependence on the Coulomb kernel is the basis of the scaling method introduced by Bernadotte et al.[103] and described in 3.1. Bernadotte et al. demonstrated that the energies of plasmonic excited states are highly dependent on the Coulomb kernel, as they involve significantly more coupling than non-plasmonic excited states. The energy of an excited state made up from single particle transitions that are relatively far apart in energy should depend on the ability of those single particle transitions to couple with one another. Thus, how strongly an excited state's energy depends on the coupling between its constituent single particle transitions can be roughly measured by looking at how far apart in energy those single particle transitions are. To this end, we calculate the standard deviation of single particle transition energies for each excited state, weighted by the contribution each transition makes to the excited state, to give the coupling range,

$$\sigma = \sqrt{\sum_{i=1}^{N} w_i (E_i - \bar{E_w})^2} \tag{3.5}$$

where σ is the coupling range, N is the number of single particle transitions contributing to the excited state, w_i is the contribution percentage of the ith single particle transition, E_i is the energy of the ith single particle transition, and E_w is the weighted average of single particle transition energies. In our experience, coupling range seems to depend on a combination of superatomic character and collectivity to varying degrees, and we also find a correlation between coupling range and oscillator strength. As we show in the next section, we have found coupling range to be a very good indicator of plasmonic character, although the use of superatomic character and collectivity as further plasmonic indicators remains necessary.

3.3 Results and Discussions

3.3.1. Applying PIM to cluster spectra

We first consider the bare Ag_{13}^{5+} cluster, which was discussed in chapter 2. We analyze data from the same TDDFT calculation as in chapter 2. The calculated absorption spectrum of Ag_{13}^{5+} is shown in Figure 3.3. In addition, Table 3.1 gives the calculated energy, intensity, superatomic character, collectivity, and coupling range values for the six transitions in this spectrum with the highest coupling ranges. As before, each excited state in this spectrum is in fact a set of triply-degenerate excited states, each with a different symmetry. The excited states presented in Table 3.1 are in fact averages of these triply-degenerate excited states.

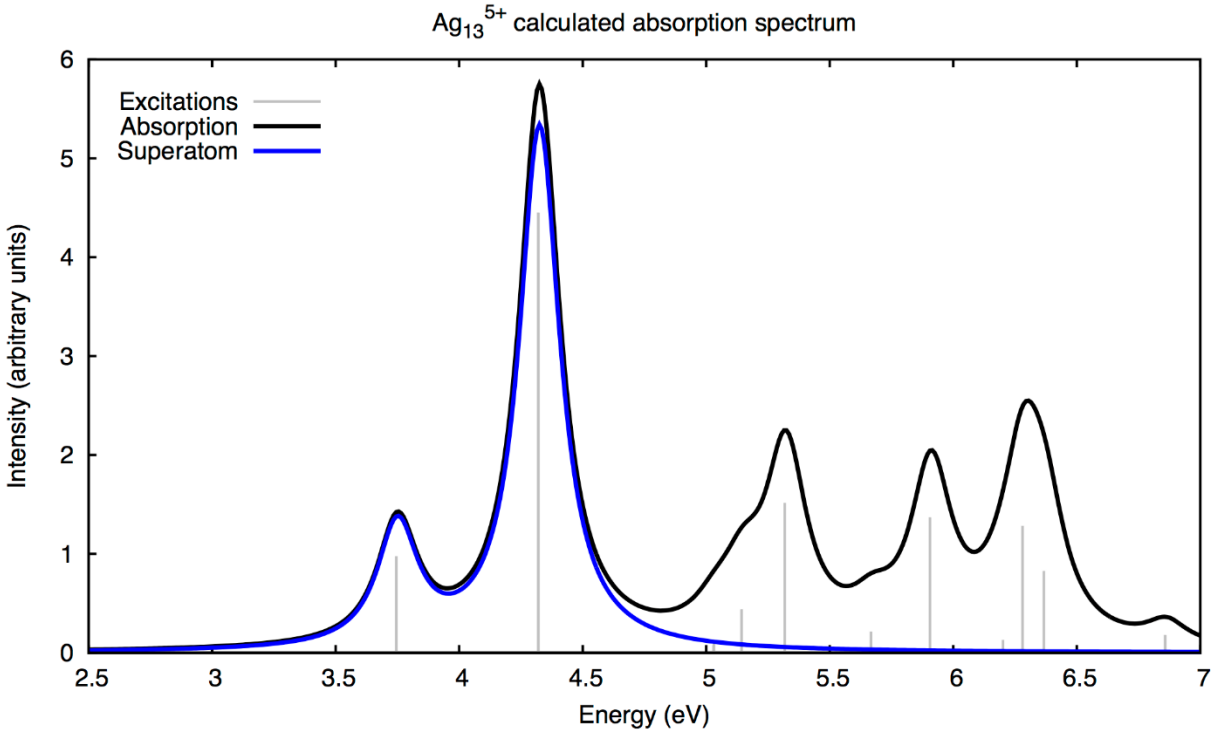

Figure 3.3. Calculated absorption spectrum of Ag_{13}^{5+} with superatomic character plotted in blue.

Table 3.1. Properties of the six excited states in the Ag_{13}^{5+} absorption spectrum with the highest coupling range values.

Energy (eV)	Oscillator strength	Superatomic character (%)	Collectivity	Coupling range (eV)
4.32	0.59	93.64	4.62	0.62
3.75	0.13	99.00	6.43	0.57
5.91	0.18	0.00	12.39	0.10
6.86	0.02	0.00	1.09	0.09
6.37	0.11	0.00	9.60	0.09
5.14	0.06	0.00	22.89	0.09

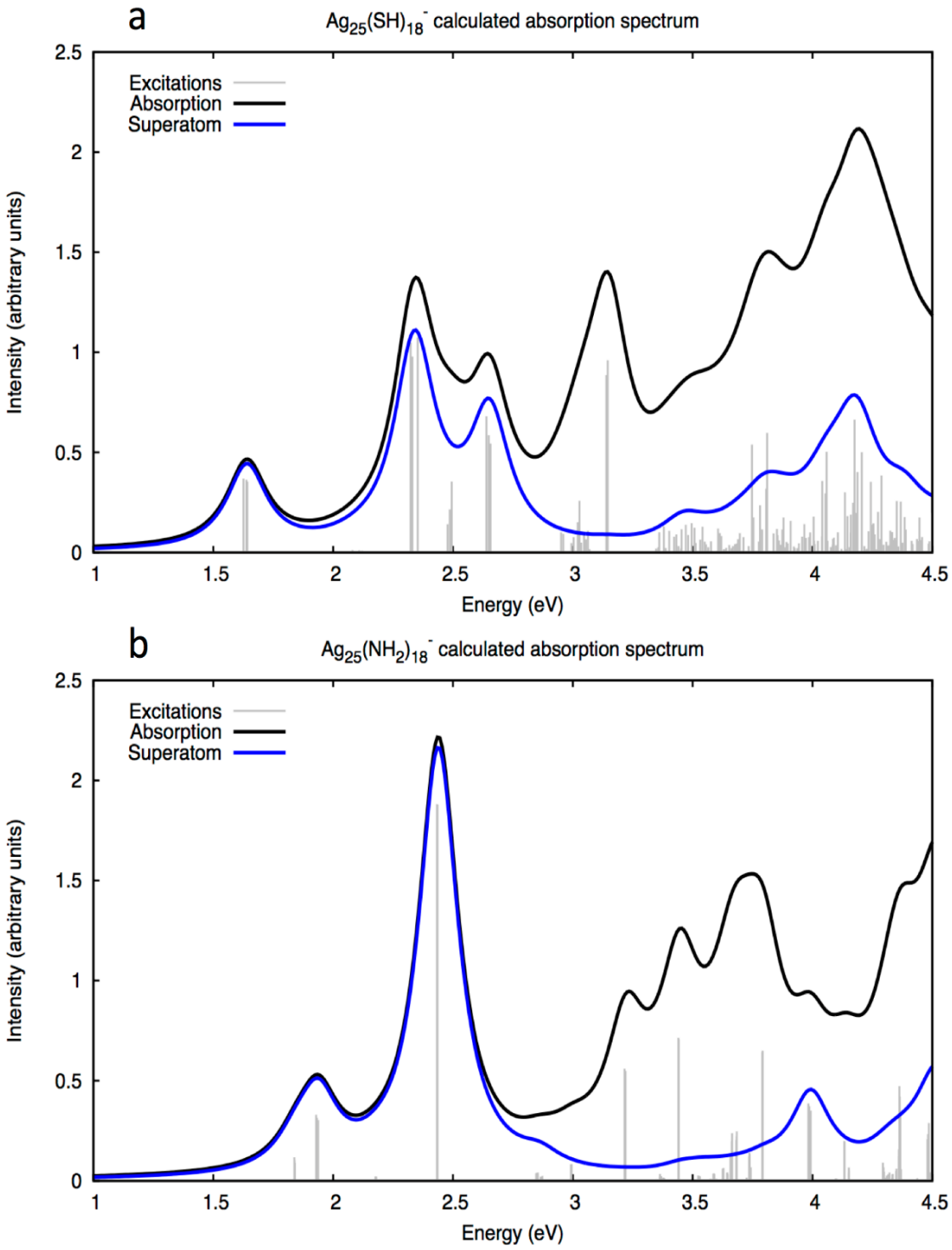

Figure 3.4. Calculated absorption spectra of (a) $Ag_{25}(SH)_{18}^-$ and (b) $Ag_{25}(NH_2)_{18}^-$.

We see in Table 3.1 that the two excited states with the highest coupling range values are both almost entirely superatomic in character and have decent collectivity values. These two peaks, at 4.32 eV and 3.75 eV, were also identified as being at least marginally plasmonic using the method described in chapter 2. The four other peaks shown here have no superatomic character, and are therefore not at all plasmonic. Here we find that the two plasmonic excited states in this spectrum also have by far the highest coupling ranges.

Next we consider the ligand-protected variants of the Ag_{13}^{5+} cluster, $Ag_{25}(SH)_{18}^{-}$ and $Ag_{25}(NH_2)_{18}^{-}$. The calculated spectrum of $Ag_{25}(SH)_{18}^{-}$ is shown in Figure 3.4a, and the six excited states with the highest coupling range values are detailed in Table 3.2. In chapter 2, we identified the excited states at 2.34 eV and 1.64 eV as being plasmonic, while that at 2.65 eV was identified as being a strong intraband transition that was not at all collective and therefore not plasmonic. Using our new analytical method, we find that the excited states at 2.34 and 1.64 eV have the highest coupling range values, followed by that at 2.65 eV.

Looking at the data in Table 3.2, it is clear that the excited state at 2.34 eV is plasmonic, as it has a very high superatomic character and a relatively high collectivity. While the peaks at 1.64 and 2.65 eV have nearly identical coupling ranges, it is easy to determine from the data in Table 3.2 that the former is at least somewhat plasmonic while the latter is not, as the peak at 1.64 eV has a collectivity of 3.00 while that at 2.65 eV only has a collectivity of 1.30. In the case of the excited state at 2.65 eV, the moderately-sized coupling range seems to come from very small contributions from a number of single particle transitions that are relatively far away in energy from one dominant single particle transition. The next three excited states in Table 3.2 all also have similar coupling range values, but they can be quickly determined not to be plasmonic by

their very low superatomic characters.

Table 3.2. Properties of the six excited states in the $Ag_{25}(SH)_{18}^-$ absorption spectrum with the highest coupling range values.

Energy (eV)	Oscillator strength	Superatomic character (%)	Collectivity	Coupling range (eV)
2.34	0.12	87.90	5.58	0.22
1.64	0.04	99.66	3.00	0.17
2.65	0.07	94.21	1.30	0.14
2.49	0.03	10.75	4.20	0.13
3.14	0.11	1.30	5.15	0.11
2.54	0.00037	3.82	2.63	0.10

The calculated absorption spectrum of the $Ag_{25}(NH_2)_{18}^-$ cluster is shown in Figure 3.4b, while the six excited states with the highest coupling ranges are shown in Table 3.3. Again, we find that the peaks identified as plasmonic in chapter 2 have the highest coupling ranges. The excited states at 2.43 eV and 1.84 eV, previously identified as plasmonic, again appear to be plasmonic. As with the thiolated cluster, there is a peak in the $Ag_{25}(NH_2)_{18}^-$ spectrum at 1.93 eV that was identified in chapter 2 as being strongly intraband but not collective. We are able to determine that this peak is not plasmonic despite its coupling range value by looking at its low collectivity. In Table 3.3 we also find another excited state that displays some slight plasmonic character, that at 2.18 eV.

Table 3.3. Properties of the six excited states in the $Ag_{25}(NH_2)_{18}^-$ absorption spectrum with the highest coupling range values.

Energy (eV)	Oscillator strength	Superatomic character (%)	Collectivity	Coupling range (eV)
2.43	0.23	99.26	5.85	0.23
1.84	0.01	99.95	5.37	0.14
1.93	0.04	99.83	1.78	0.12
2.99	0.01	0.28	3.27	0.09
3.22	0.07	0.64	5.04	0.09
2.18	0.0025	99.45	2.69	0.09

Finally, we use our new analytical method to analyze the calculated spectra of the Ag_{32}^{14+} (Figure 3.5a and Table 3.4) and $Ag_{44}(SH)_{30}^{4-}$ (Figure 3.5b and Table 3.5) clusters. In chapter 2 only one peak in the Ag_{32}^{14+} spectrum, that at 2.35 eV, was found to be plasmonic. With our new analytical method, the only peak that stands out as clearly plasmonic is that same peak at 2.35 eV, which has by far the highest coupling range value, a 100% superatomic character, and a very high

Table 3.4. Properties of the six excited states in the Ag_{32}^{14+} absorption spectrum with the highest coupling range values.

Energy (eV)	Oscillator strength	Superatomic character (%)	Collectivity	Coupling range (eV)
2.45	0.16	100.00	13.99	0.52
3.45	0.03	40.04	16.76	0.16
3.74	0.04	14.35	4.02	0.10
3.86	0.02	0.84	7.76	0.07
3.92	0.03	0.66	2.95	0.07
3.24	0.003	99.78	5.56	0.07

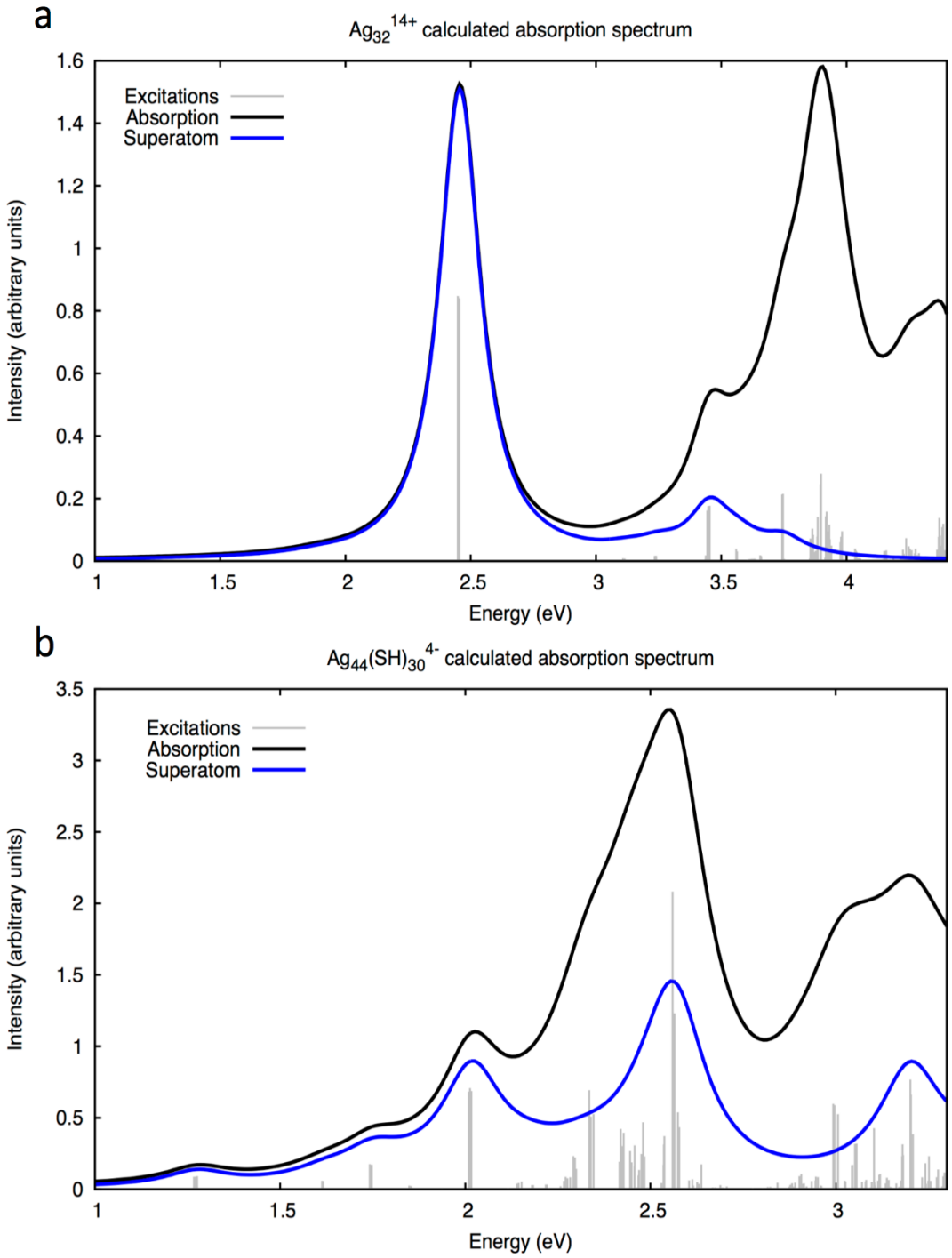

Figure 3.5. Calculated absorption spectra of (a) Ag_{32}^{14+} and (b) $Ag_{44}(SH)_{30}^{4-}$.

collectivity. The next excited state in Table 3.4, that at 3.45 eV, has a very high collectivity, but its superatomic character is only about 40%. The only other excited state in Table 3.4 that looks plasmonic at all is that at 3.24 eV, which has a near-100% superatomic character and a somewhat high collectivity. This peak may be mildly plasmonic, but it does have a very low oscillator strength of 0.003.

Table 3.5. Properties of the six excited states in the $Ag_{44}(SH)_{30}^{4-}$ absorption spectrum with the highest coupling range values, followed by an excited state that was identified as plasmonic in chapter 2 (that at 1.62 eV).

Energy (eV)	Oscillator strength	Superatomic character (%)	Collectivity	Coupling range (eV)
2.01	0.08	100.00	14.46	0.23
2.56	0.17	61.90	6.95	0.14
1.75	0.02	100.00	6.51	0.14
2.30	0.02	21.40	5.65	0.12
2.34	0.07	12.86	4.45	0.11
1.27	0.01	100.00	3.72	0.11
1.62	0.0067	100.00	5.33	0.08

When applied to the $Ag_{44}(SH)_{30}^{4-}$ cluster, our new analytical method again gives reasonable results. In chapter 2, four plasmonic excited states were identified for this cluster at 1.62, 1.75, 2.01 eV, and 2.56 eV. Three of those four are present in Table 3.5 and have the three highest coupling range values. The excited states at 2.01 and 1.75 eV clearly read as plasmonic, as they have high collectivities and 100% superatomic characters. The excited state at 2.56 eV seems to be somewhat less plasmonic, as its superatomic character is only 61.90%. The excited state at 1.62 eV also appears plasmonic, although its oscillator strength is very low.

For each cluster studied here, performing analysis of calculated spectra using superatomic

character, collectivity, and coupling range as plasmonic indicators successfully identifies as plasmonic those excited states that were so identified in chapter 2. This is done with a far less labor-intensive method that can be easily automated. Furthermore, additional, quantified insight is gained into the characters of the excited states of interest, where we now have metrics for superatomic character, collectivity, and the extent to which an excited state depends upon coupling.

3.3.2 Quadrupolar plasmons in Ag nanorods

Next, we present a brief demonstration of the identification of quadrupolar plasmons in cluster-sized Ag nanorods. Up to this point in the current chapter, only dipole-allowed excited

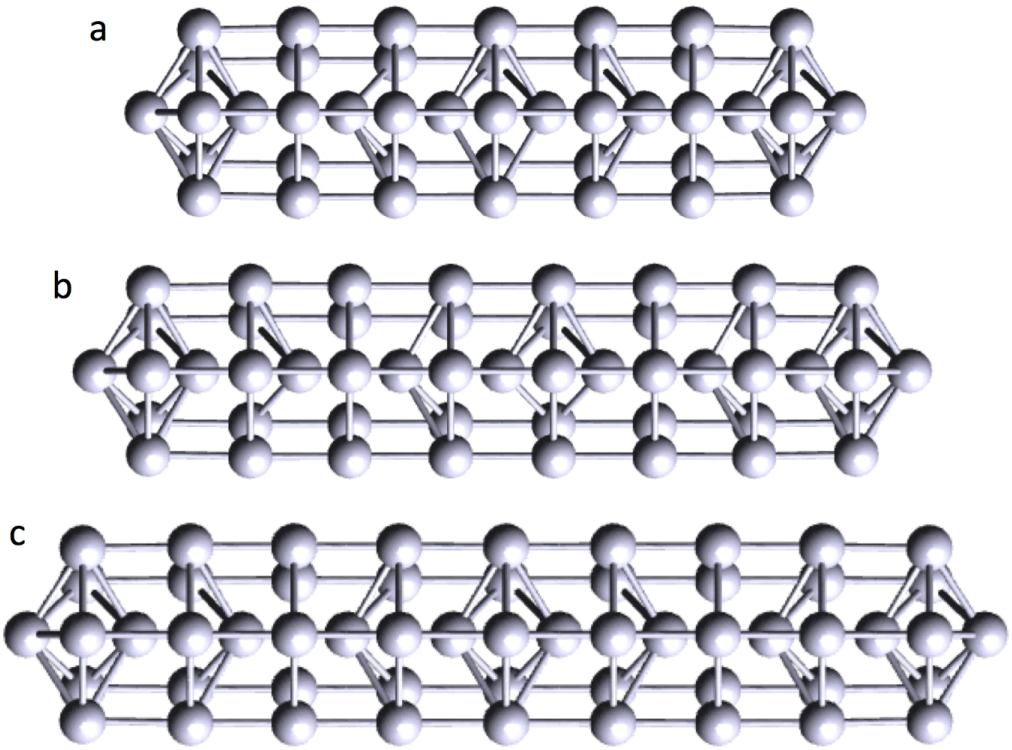

Figure 3.6. Geometry-optimized structures of (a) Ag_{43}^{+}, (b) Ag_{49}^{+}, and (c) Ag_{55}^{+}.

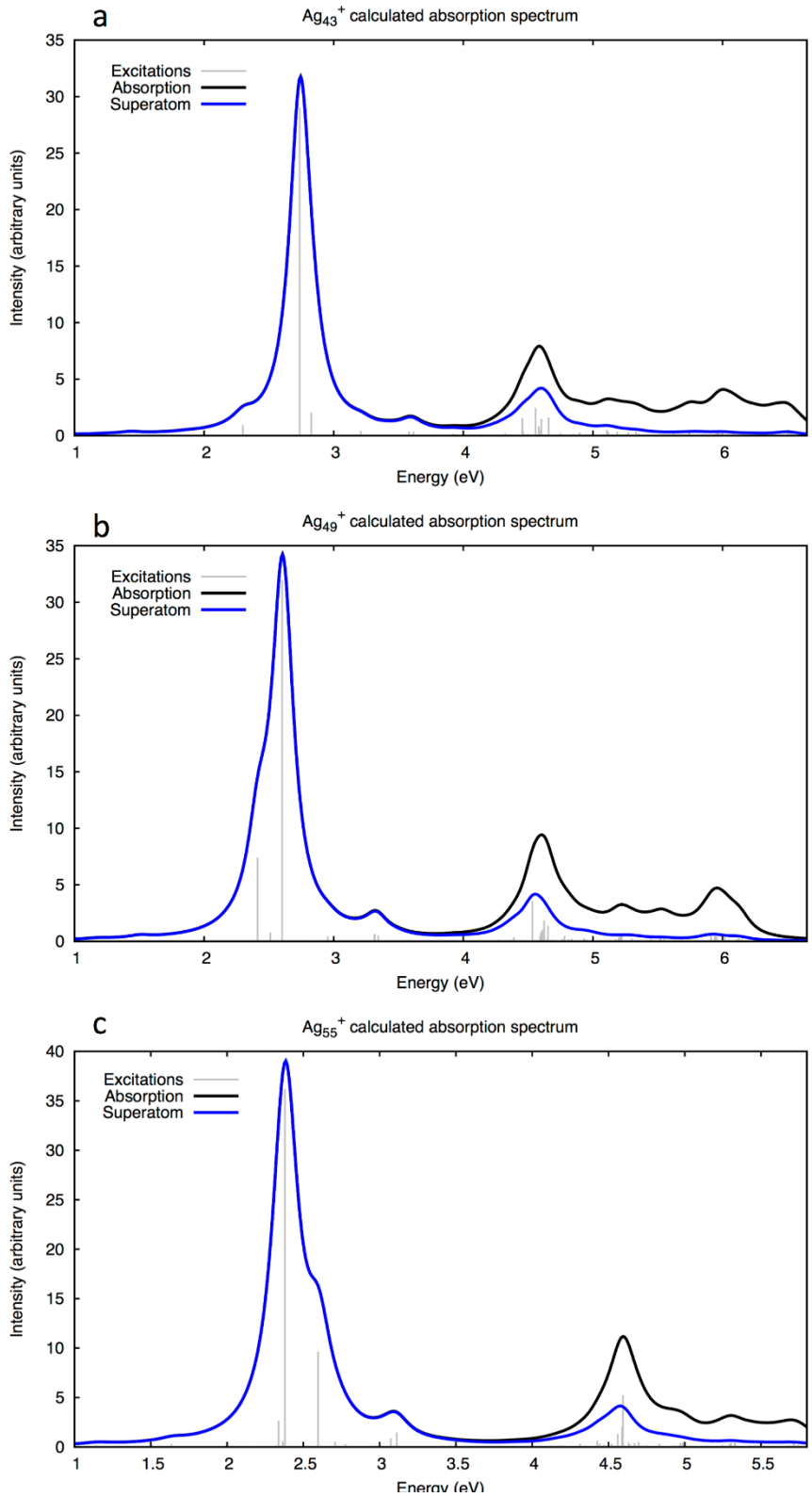

Figure 3.7. Calculated absorption spectra of the Ag nanorod clusters (a) Ag_{43}^{+}, (b) Ag_{49}^{+}, and (c) Ag_{55}^{+}.

states have been considered. To study quadrupolar plasmons, however, we calculated transition quadrupole moments in addition to transition dipole moments. This adds considerably to the expense of the TDDFT calculation, but it is necessary to gauge the ability of PIM to identify quadrupolar plasmons. Oscillator strengths presented below are calculated using only transition dipole moments. However, we have observed that even if oscillator strength includes contributions from transition quadrupole moments, in every case the quadrupole contribution is negligible. It should also be noted that for all excited states with a non-zero oscillator strength (that is, a non-zero transition dipole moment), the calculated longitudinal transition quadrupole moment (Q_{zz}) will depend heavily on the choice of origin in the system, and will therefore be meaningless. Thus, we do not give Q_{zz} values for dipole-allowed transitions.

The structures of the three Ag nanorods we studied, Ag_{43}^{+}, Ag_{49}^{+}, and Ag_{55}^{+}, are shown in Figure 3.6. Each of these structures consists of a series of Ag layers alternating between individual Ag atoms and five Ag atoms arranged pentagonally. These three clusters were previously studied by Gieseking et al.[106] and were found using an INDO/CI approach to have quadrupolar plasmons. The calculated absorption spectra of the three clusters are shown in Figure 3.7. No quadrupolar plasmons are visible in these spectra, as the quadrupolar modes are optically dark and thus have negligible oscillator strength. For each of these clusters, the six excited states with the highest coupling ranges are shown in Table 3.6 as in the tables in the previous section, but with their longitudinal transition quadrupole moments shown as well. The oscillator strength values given in Table 3.6 are calculated using only transition dipole moments.

Table 3.6. Properties of the six excited states in each of the three Ag nanorod cluster absorption spectra with the highest coupling range values.

Ag_{43}^{+}					
Energy (eV)	Oscillator strength (arb. units)	Superatomic character (%)	Collectivity	Coupling range (eV)	Q_{zz} (ea_0)
3.99	0.00	100.00	8.88	0.88	121.65
4.01	0.00	100.00	3.40	0.79	90.88
2.74	9.54	99.90	4.48	0.64	0.00
4.56	0.80	45.56	4.60	0.53	0.00
4.66	0.03	33.51	26.74	0.49	0.00
6.61	0.00	69.81	2.44	0.45	0.00
Ag_{49}^{+}					
Energy (eV)	Oscillator strength (arb. units)	Superatomic character (%)	Collectivity	Coupling range (eV)	Q_{zz} (ea_0)
3.81	0.00	100.00	11.40	0.96	188.88
2.60	10.06	99.95	4.36	0.74	0.00
2.41	2.33	99.98	1.85	0.63	0.00
4.39	0.069	96.33	2.36	0.54	0.00
4.53	1.12	65.16	8.58	0.54	0.00
4.10	0.00	100.00	5.30	0.44	62.87
Ag_{55}^{+}					
Energy (eV)	Oscillator strength (arb. units)	Superatomic character (%)	Collectivity	Coupling range (eV)	Q_{zz} (ea_0)
3.64	0.00	100.00	3.85	0.80	144.13
4.44	0.11	83.43	6.65	0.71	0.00
2.38	10.86	100.00	4.59	0.68	0.00
3.88	0.00	100.00	6.65	0.66	126.60

3.61	0.00	100.00	4.34	0.66	121.40
4.60	1.57	36.70	20.33	0.62	0.00

Quadrupolar plasmons are identifiable in all three clusters. In Ag_{43}^{+}, the two excited states with the highest coupling ranges are both dark states at right around 4 eV. Each has 100% superatomic character; one has a very high collectivity, and the other has a decent collectivity. These two excited states also have high Q_{zz} values, indicating that they are quadrupolar. The other excited state with a high coupling range, that at 2.74 eV, has a very high oscillator strength at 9.54, and is thus clearly a dipolar plasmon. In Ag_{49}^{+}, two dark excited states with high Q_{zz} values are also observed, at 3.81 and 4.10 eV. Again, these two excited states have 100% superatomic characters and high collectivities. We also find a clear dipolar plasmon at 2.60 eV and a moderately dipolar plasmonic excited state at 4.53 eV. Finally, in Ag_{55}^{+}, three dark excited states with high Q_{zz} values are observed, each of which has 100% superatomic character and mid-to-high collectivity. These excited states are also near one another in energy, suggesting that they together make up the quadrupolar plasmon of the Ag_{55}^{+} cluster.

3.3.3 Grouping excited states

Another important feature of plasmons in the cluster regime is their size-dependence. The size-dependence of plasmonic excited states in bare Ag nanoclusters was first studied by Aikens et al.[47] in 2008. In this study, the authors calculated the absorption spectra of tetrahedral Ag clusters ranging from Ag_{10} up to Ag_{120} using TDDFT. A dominant plasmonic peak was observed in each of these clusters, red-shifting with increasing size. The plasmonic peaks were also seen to broaden as size increased, with the single plasmonic excited state of Ag_{20} being replaced by a larger and

larger number of such states. These plasmonic peaks were shown to be consistent with those seen in far larger Ag nanoparticles as modeled by classical electrodynamics. This study suggests that the plasmon observed in Ag_{20} as well as those in the other clusters considered in this chapter differ from those in larger clusters in that they consist of only a single plasmonic excited state or a single set of degenerate plasmonic excited states. As cluster size increases, plasmonic peaks become more and more classical in that they consist of a large number of different plasmonic excited states all around the same energy.

To measure the growth of plasmons with increasing cluster size as described in the previous paragraph, we present a simple model for grouping excited states with similar energies together. In this model, we consider not just the superatomic characters, collectivities, and coupling ranges of individual excited states, but also the collectivities and superatomic characters of groups of excited states. The objective of this model is to describe the transition of the plasmonic peaks in the tetrahedral Ag clusters considered by Aikens and coworkers from molecular plasmons to classical plasmons, and to do so by applying the same concepts we use to analyze individual excited states.

We use the coupling ranges of individual excited states to determine how they are grouped together. In our model, two excited states can be grouped together if the distance in energy between them is smaller than the coupling range of each of the excited states. If this is true, then we consider them to be in "mutual range" of one another. We determine every possible set of excited states that are all within mutual range of one another, and then we select the combination with the highest oscillator strength, with oscillator strength of the combination being simply the sum of the oscillator strengths of the constituent excited states. Once this combination is selected, every other combination that contains any of the excited states within this first combination is considered

invalid, and removed from the pool. Then the combination with the next highest oscillator strength is selected, and so on until each excited state belongs to a combination, even if that combination has only one element. We call these selected combinations "groups." We then calculate a "group collectivity" for each group, where we repurpose the transition inverse participation ratio given in equation 3.4, giving

$$\tau_{group} = \left[\sum_{i=1}^{n_{exc}} \frac{f_i}{\sum_{j=1}^{n_{exc}} f_j} \right] \tag{3.6}$$

where τ_{group} is the group collectivity, n_{exc} is the number of excited states in the group, and f_i is the oscillator strength of the ith excited state. We consider group collectivity a loose metric of the classical character of a plasmonic peak.

To ensure that the only large groups we find are plasmonic, or at least are not composed of clearly non-plasmonic excited states, we only allow excited states with greater than 30% superatomic character to join groups. This is necessary due to the presence, in some cases, of non-superatomic excited states near superatomic excited states of interest. This also aids in reducing the computational cost of this model. As with most parameters and cutoffs employed in this model, this value is arbitrary, but it does seem to be effective in dealing with the systems in question. We do not institute a similar cutoff for collectivity of excited states, as we are interested in group rather than excited state collectivity. Furthermore, excited states with low coupling range values should typically be unable to be part of large groups, which helps to keep non-plasmonic excited states from joining otherwise plasmonic groups.

We applied this analytical model to the tetrahedral Ag clusters studied by Aikens et al. We performed TDDFT calculations in the same manner as before, but at the PBE/DZ.4p level of theory. The calculated absorption spectra of these clusters are shown in Figure 3.8, and the results

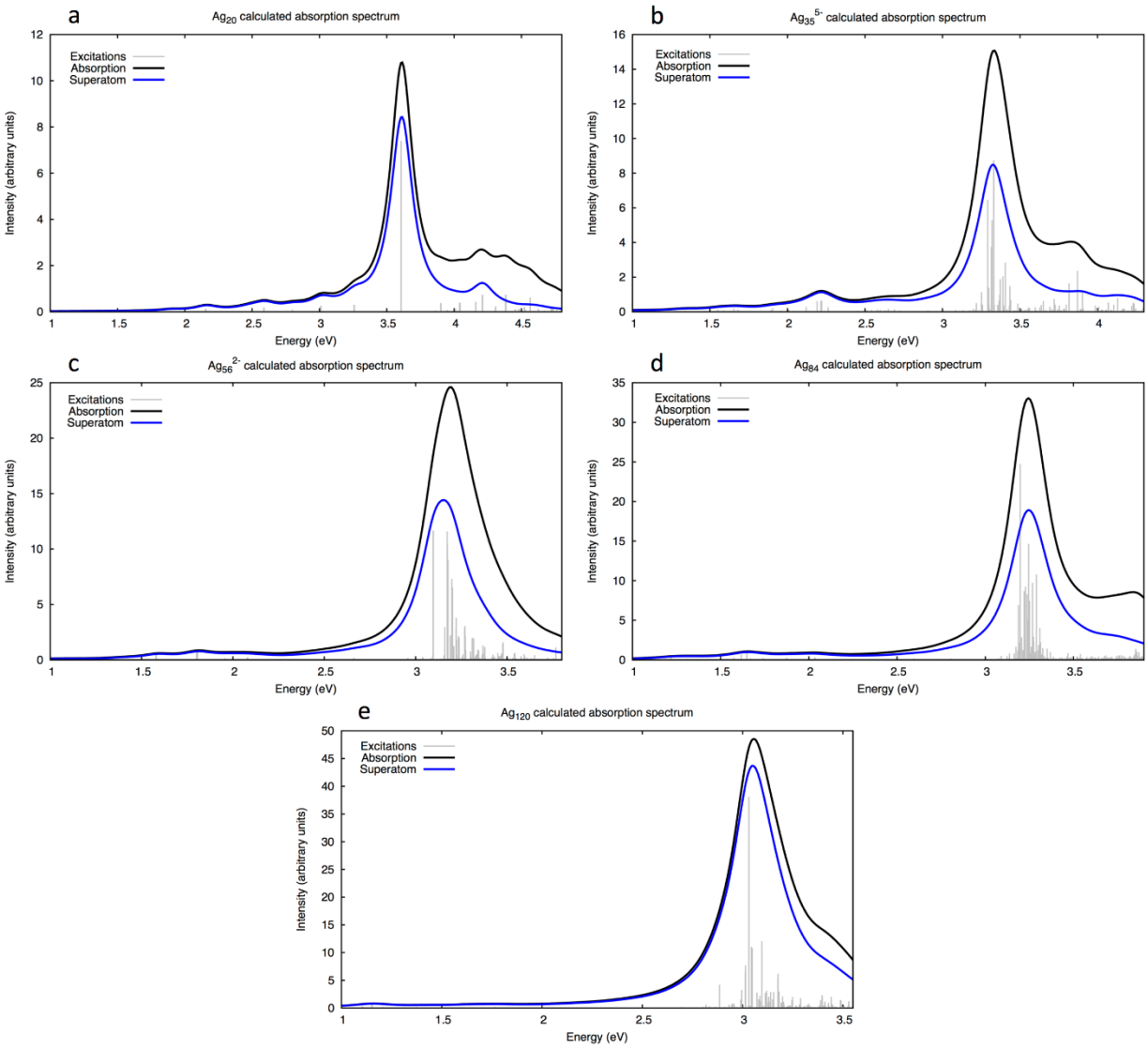

Figure 3.8. Calculated absorption spectra of (a) Ag_{20}, (b) Ag_{35}^{5-}, (c) Ag_{56}^{2-}, (d) Ag_{84}, and (e) Ag_{120}.

of our analysis are given in Table 3.7, in which we present for each tetrahedral cluster the group with the highest oscillator strength. We do not find a monotonic trend of either increasing oscillator strength or increasing group collectivity, but we do note the increase in group collectivity as we go from Ag_{20} to Ag_{35}^{5-} and then to Ag_{56}^{2-}. Group collectivity then decreases slightly from Ag_{56}^{2-} to Ag_{84}, and then decreases again somewhat as size is increased to Ag_{120}. These decreases may simply be anomalous, as even Ag_{120} is still small enough that its electronic structure consists of

discrete orbitals rather than bands. Until a cluster is large enough that its electronic structure becomes truly band-like, the exact energies and compositions of its excited states may depend on quirks of orbital spacing. Unfortunately, as is so often the case when working with a computational method as expensive as TDDFT, it is not a trivial matter to calculate absorption spectra for tetrahedral Ag clusters larger than those we have considered.

Table 3.7. Group properties of the largest groups in each of the five tetrahedral Ag clusters considered in this study.

Cluster	Group oscillator strength	Group collectivity	Group superatomic character (%)
Ag_{20}	3.32	3.00	79.06
Ag_{35}^{2-}	3.60	4.97	66.36
Ag_{56}^{5-}	5.84	8.23	78.92
Ag_{84}	7.27	7.33	60.39
Ag_{120}	8.78	6.87	95.40

Ultimately, the model presented here is a first attempt to consider plasmonic character not only as a feature of individual excited states but also as a feature of peaks in an absorption spectrum, which may be caused by multiple excited states close in energy. We find that we are able to successfully measure the transition of the plasmonic peaks in the Ag tetrahedral clusters from molecular to at least somewhat classical.

3.4 Conclusions

We have developed a new analytical method, the plasmonic indicator method (PIM), for identifying and analyzing plasmonic excited states in the calculated spectra of metal clusters. This method is built on three primary indicators of plasmonic character: superatomic character, collectivity, and coupling range. We demonstrated that, using this method, we can identify the same plasmons we find using the less robust and more labor-intensive PCM, and that we can also

gain additional, quantifiable insight into the nature of the plasmonic excited states in question. We also demonstrated that PIM is capable of successfully identifying quadrupolar plasmons as well as dipolar plasmons. In future studies this capability may aid in the identification and analysis of quadrupolar plasmons in systems large enough that the calculation of large numbers of transition quadrupole moments is impractical. And finally, we demonstrated a new, simple model for measuring the transition of plasmonic peaks from molecular to classical with increasing cluster size. Using this model, we showed that Ag tetrahedral clusters get closer to the classical regime, with a broad plasmon consisting of numerous excited states, as cluster size increases.

CHAPTER 4

Studying the Length-Dependence of Plasmons in Ligand-Protected Box-Like Ag Nanoclusters

4.1 Introduction

The dependence of LSPR energies on nanoparticle size is well-understood for most nanoparticle sizes. As discussed previously, classical electrodynamics methods such as Mie theory,[38] DDA,[43] and FDTD[44] are able to accurately predict plasmon energies as size, shape, composition, and dielectric environment change. However, in the small-particle limit, these methods cease to be accurate. A clear example of this comes from the 2010 study by Peng et al.[45] (as discussed in 2.1), which showed that experimentally-measured LSPRs and classically-calculated LSPRs diverge strongly for Ag nanoparticles below about 20 nm in diameter. This was found to be due to both a failure of classical methods to properly account for the particular dielectric properties of the particle surface as well as a failure to model interactions between ligands and the particles to which they are bound. Surface and ligand effects are both significant only at small sizes due to the increase of surface-to-volume ratio as particle diameter decreases.

As discussed in 3.3.3, Aikens et al.[47] published a study on the size-dependence of plasmons in bare tetrahedral Ag nanoclusters ranging from Ag_{20} to Ag_{120} using TDDFT. From the results of this study, the authors were able to express the energy of the plasmonic peak as a function of the inverse edge length of the cluster. They then used this expression to predict the energy of the

plasmon in a tetrahedral Ag nanoparticle with a 32 nm edge length, and found that the value thus predicted agreed with the plasmon energy predicted for such a particle using the classical DDA method. This 2008 Aikens et al. study remains one of the key links between plasmons found using quantum mechanical methods and those found using classical methods. Similar studies have been performed using TDDFT to study trends in plasmonic excited states of bare Ag and Au nanorod-like clusters, although the typically small widths of these model systems render comparison with classical methods difficult.[117,118] While this has been done using bare clusters, a similar study has never been performed using ligand-protected Ag clusters.

We have studied in detail the effects of ligands on plasmons in Ag nanoclusters.[119] As presented in chapter 2, in this work we showed the mechanisms by which ligands affect plasmons in small Ag clusters: splitting conduction orbitals, altering the spacings between various sets of orbitals, and localizing conduction electrons on the Ag atoms that explicitly bind with the ligands. We expect that with increasing cluster size each of these effects should become less significant, and that in the large-cluster limit the plasmons seen in a ligand-protected cluster should be nearly identical to those seen in a bare cluster, save for a small shift in energy due to the change in the dielectric function of the cluster surface.

However, the study of plasmon size-dependence in ligand-protected clusters presents several major challenges. First, to truly study size-dependence, the shapes of each cluster studied must be identical. However, the number of atoms that must be added to a cluster to increase size in three dimensions while maintaining shape increases with each step. If one were to scale up near-spherical clusters like the ones studied in chapters 2 and 3 in three dimensions in an attempt to observe changes in plasmonic behavior with increasing size, one would very quickly be working with clusters containing so many atoms as to render TDDFT calculations computationally

impractical. This problem has been overcome in studies of bare clusters by working with highly-symmetric cluster shapes to reduce computational cost, but as shown in chapter 2, the ligand-protected near-spherical clusters we have studied have only C_i symmetry, making the possibility of obtaining even three data points for either shape remote. Another major obstacle is that the structures and arrangement of the oligomeric ligands in the Ag_{25} and Ag_{44} ligand-protected clusters are not repeatable at larger sizes, and there are currently no experimentally-determined structures of similarly-shaped but larger Ag clusters. For example, if the icosahedral Ag_{13}^{5+} core of the Ag_{25} clusters were scaled up to the next-largest icosahedral cluster, Ag_{43}^{3+}, the six $Ag_2S_3^-$ oligomeric ligand units arranged octahedrally around the cluster core would need to be increased in size, number, or both. Without taking the structure and arrangement of the ligands from experimental data, one would be left to improvise the structure of the ligand-protected variant of Ag_{43}^{3+}, casting doubt on the meaningfulness of the results of any calculation.

A solution to both of these problems has presented itself in the recent synthesis and characterization of the $[Ag_{67}(SH)_{32}(PH_3)_8]^{3+}$ cluster.[120] This new cluster is shaped like a rectangular prism with ligands coating each side as well as attached to each of its eight corners. The structure of this cluster is modular and can be extended longitudinally by repeating its central building block, which is covered in ligands, as shown in detail below. Thus, we can generate an infinite number of ligand-protected cluster structures of varying lengths. We call this cluster and all clusters built from its components “box clusters”. Because cluster size is only increased in one dimension, the same number of atoms is added to the cluster with each size step, keeping the increase in computational cost relatively low. In addition, the ligand structure of each copy of the central building block is clearly defined, making it fully possible to compare computational results from different clusters following this same pattern. Furthermore, unlike the pentagonal nanorod-

like Ag clusters that are typically studied, the arrangement of the Ag atoms in the $[Ag_{67}(SH)_{32}(PH_3)_8]^{3+}$ cluster is the same as that of bulk Ag, face-centered cubic.

In this chapter, we present a study of the plasmonic behavior of ligand-protected box clusters of varying sizes, from $[Ag_{46}(SH)_{24}(PH_3)_8]^{2+}$ to $Ag_{172}(SH)_{72}(PH_3)_8$, using the PIM analysis presented in chapter 3. We find that increasing box cluster length results in a red-shift of longitudinal plasmon energies, as would be expected in a bare nanorod-like cluster. However, we also find that the splitting of the longitudinal plasmon by the ligands is very persistent with increasing length, only giving a single plasmon at the longest cluster we study, and even then this single plasmon may well be an artifact. The box clusters in this study are thin enough that the effects of ligands wrapped around the sides of the clusters can dramatically affect longitudinal excited states, and due to the slowly-changing surface-to-volume ratio of these clusters, increasing length appears to do little to offset this. Ultimately, we find that increasing box cluster length does not seem likely to result in a significant reduction in ligand effects on plasmon resonance, although we do find clear plasmon resonances in each cluster above the smallest size studied.

4.2 Computational Methods

All calculations in this chapter were performed using the Amsterdam Density Functional 2016.103 software package.[89, 90, 114] The LB94 model potential[115] was used and a double-ζ (DZ) Slater-type basis set with a $[1s^2–3d^{10}]$ frozen core for Ag, a $[1s^2–3p^4]$ frozen core for S, and a $[1s^2–3p^3]$ frozen core for P.[82, 83] For all cluster calculations we accounted for relativistic effects using ZORA.[84–86]

4.3 Results and Discussion

4.3.1 Cluster structures

The structure of the $[Ag_{67}(SH)_{32}(PH_3)_8]^{3+}$ cluster is shown in Figure 4.1, along with the various components into which this structure can be broken down. We first describe the process by which this structure can be expanded in one dimension (or contracted, although this can only be done one time). The $[Ag_{67}(SH)_{32}(PH_3)_8]^{3+}$ cluster has an oblong, rectangular prism-like structure, with thiolate ligands covering each face and phosphine oligomeric ligands (present as $AgPH_3^+$ units) bound to each corner. Without any ligands attached, this cluster would be Ag_{59}.

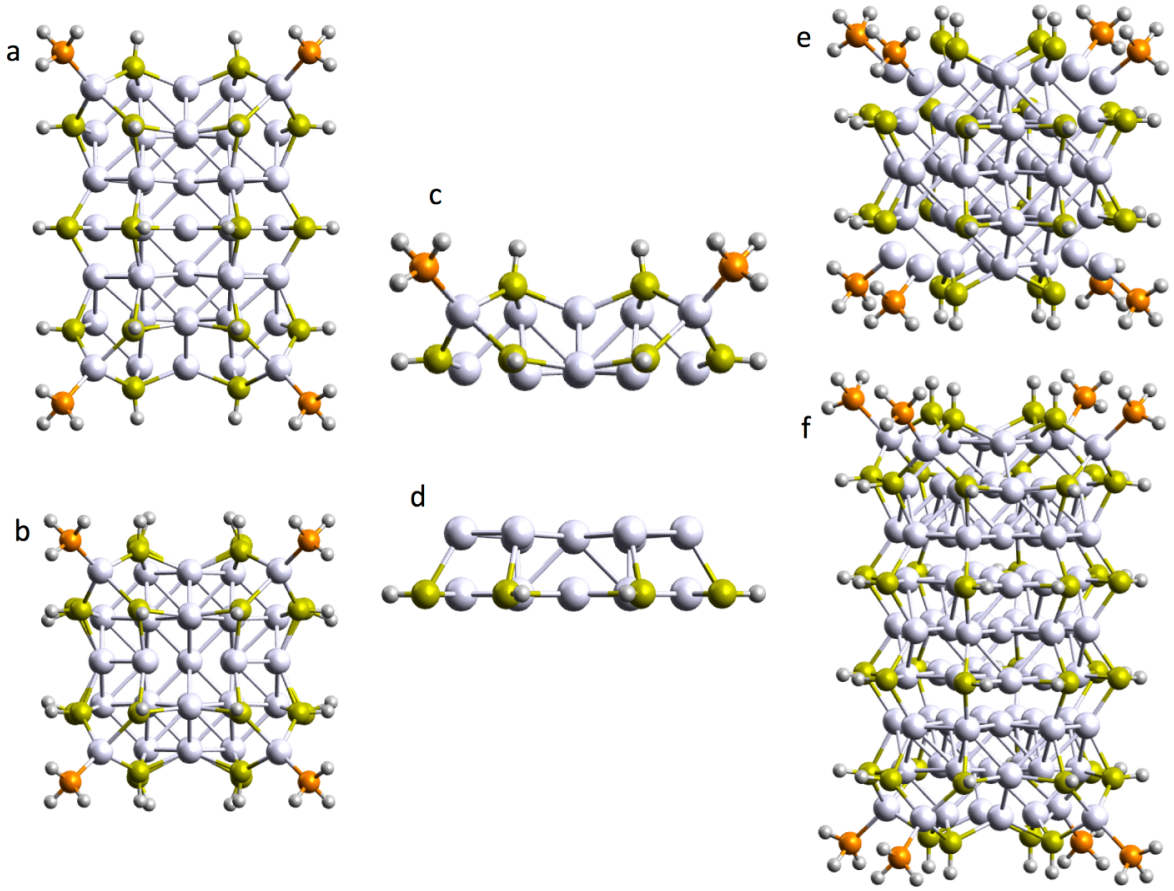

Figure 4.1. (a) A side view of the $[Ag_{67}(SH)_{32}(PH_3)_8]^{3+}$ cluster, (b) a top view of the $[Ag_{67}(SH)_{32}(PH_3)_8]^{3+}$ cluster, (c) a box cluster end piece, (d) a box cluster middle piece, (e) the $[Ag_{46}(SH)_{24}(PH_3)_8]^{2+}$ cluster, and (f) the $[Ag_{88}(SH)_{40}(PH_3)_8]^{2-}$ cluster.

The "ends" of the Ag_{59} core of the cluster can be thought of as separate pieces, each consisting of two layers of Ag atoms: the layer on the very end is 4 Ag atoms, and the other layer is 9 Ag atoms. When ligand-protected, these end pieces bear 12 SH ligands and 4 $AgPH_3^+$ ligands. In the Ag_{59} core there are then three layers remaining. These contain, in order, 12, 9, and 12 Ag atoms, with the 9-atom layer also bearing 8 SH ligands when the structure is ligand-protected. This central portion of the structure can be thought of as alternating between bare 12-atom layers and ligand-bearing 9-atom layers. To extend the structure along the longitudinal dimension, a pair of 9-atom and 12-atom Ag layers can be added to this region. Conversely, to contract the structure, a 9-atom and 12-atom layer can be removed, although this can only be done once to the $[Ag_{67}(SH)_{32}(PH_3)_8]^{3+}$ cluster. The results of both of these processes are shown in Figures 4.1e and 4.1f. In our study, we continually expanded the $[Ag_{67}(SH)_{32}(PH_3)_8]^{3+}$ structure until we reached the limits of computational feasibility. The largest cluster we were able to effectively study was $[Ag_{172}(SH)_{72}(PH_3)_8]$. In total, we studied seven box cluster structures. Of these, the $[Ag_{67}(SH)_{32}(PH_3)_8]^{3+}$ thiolated cluster is the only one that has been experimentally synthesized and characterized thus far.

It is important to note here that a previous study has determined that the $[Ag_{67}(SH)_{32}(PH_3)_8]^{3+}$ thiolated cluster has 32 conduction electrons.[121] In chapters 2 and 3, the bare Ag_{13}^{5+} and Ag_{32}^{14+} clusters we investigated were highly positively-charged so as to have the same number of conduction electrons as their ligand-protected variants. For the bare Ag_{59} cluster, however, a 27+ charge would be necessary to maintain a number of conduction electrons consistent with that of the $[Ag_{67}(SH)_{32}(PH_3)_8]^{3+}$ cluster. While Ag_{13}^{5+} and even Ag_{32}^{14+} were at least somewhat stable structures that could give reasonable results, the Ag_{59}^{27+} cluster unsurprisingly explodes during any geometry optimization, and its calculated absorption spectrum without

optimization is nonsensical. This problem only gets worse with increasing cluster size, and thus it is impossible to meaningfully compare bare and ligand-protected box clusters to determine the extent of ligand effects on plasmonic excited states.

Except for the $[Ag_{67}(SH)_{32}(PH_3)_8]^{3+}$ cluster, which has been synthesized with a 3+ charge, the preferred charge states of the clusters in this study are not known. In general, we choose charge

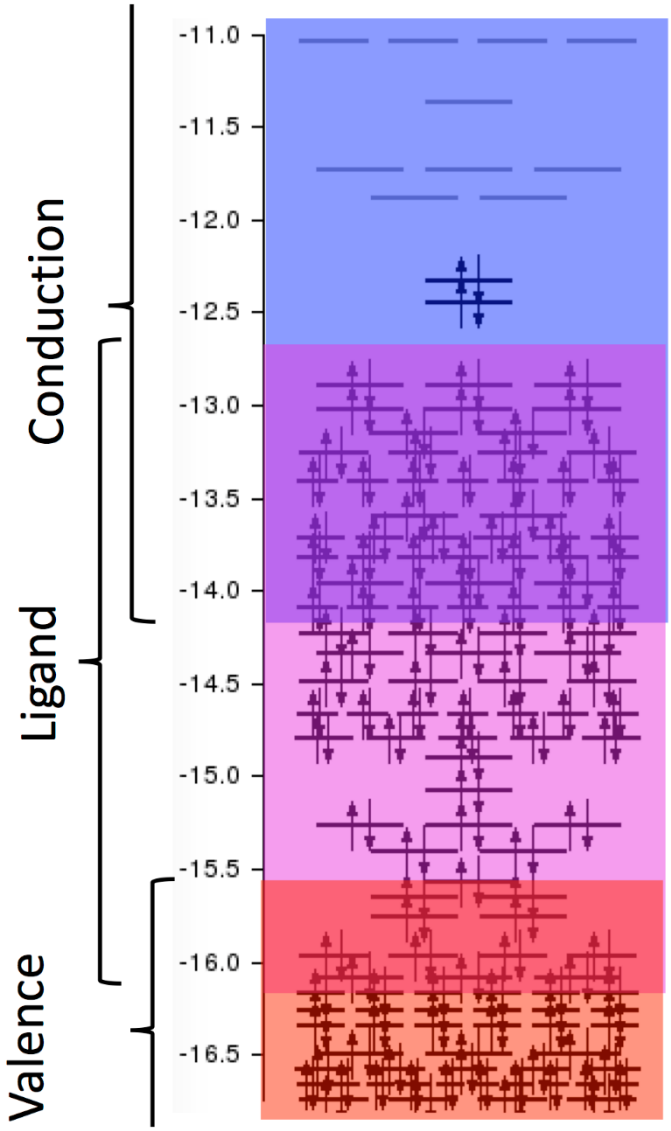

Figure 4.2. A portion of the orbital energy diagram for the ligand-protected $[Ag_{67}(SH)_{32}(PH_3)_8]^{3+}$ cluster.

states that result in a closed-shell electronic structure, and then of those charge states we select the least-charged state. When this process results in a "tie" between a positively- and negatively-charged state, we select the positively-charged state so as to reduce the number of electrons in the calculation.

As apart from the $[Ag_{46}(SH)_{24}(PH_3)_8]^{2+}$ cluster each box cluster in this study is oblong, they can have both transverse and longitudinal plasmons. As we are only altering cluster length and not thickness, we only consider longitudinal plasmons.

4.3.2 Electronic structure

A portion of the electronic structure of the $[Ag_{67}(SH)_{32}(PH_3)_8]^{3+}$ cluster is shown in Figure 4.2. Unlike the electronic structures of the bare Ag_{13} and Ag_{32} clusters and ligand-protected Ag_{25} and Ag_{44} clusters shown in chapter 2, here we do not see clear and distinct sets of degenerate orbitals. Instead, there are a great many orbitals close together just below the HOMO, many of which are in fact superatomic orbitals. As shown by Juarez-Mosqueda et al.[121], the superatomic

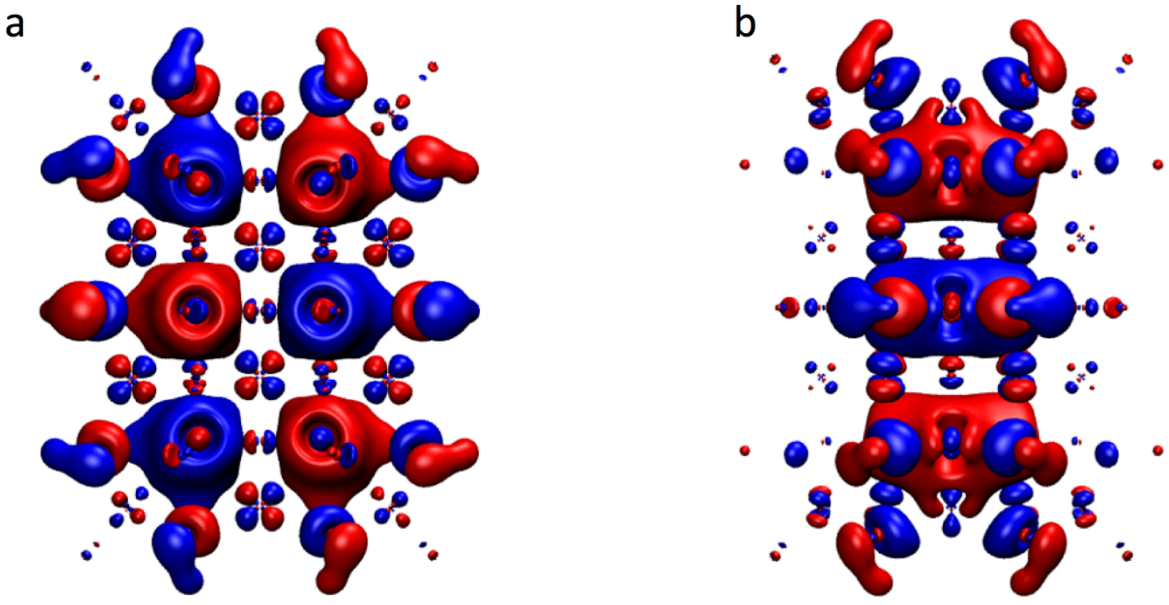

Figure 4.3. (a) View along the x-axis and (b) view along the y-axis of a superatomic orbital of the $[Ag_{67}(SH)_{32}(PH_3)_8]^{3+}$ cluster.

orbitals of $[Ag_{67}(SH)_{32}(PH_3)_8]^{3+}$ and other box clusters do not look like spherical harmonics as they do for the near-spherical clusters considered previously. Rather, they appear to be solutions to the particle in a 3D box problem. An example superatomic orbital of the $[Ag_{67}(SH)_{32}(PH_3)_8]^{3+}$ cluster is shown in Figure 4.3. These superatomic orbitals are only ever doubly-degenerate. Furthermore, as discussed above, there are 32 conduction electrons present in this system, compared with 8 in the Ag_{13}/Ag_{25} clusters and 18 in the Ag_{32}/Ag_{44} clusters. This, along with significant mixing of superatomic and ligand character, leads to a very complex electronic structure that is not easily broken down into distinct sets of orbitals.

4.3.3 Absorption spectra

4.3.3.1 $[Ag_{46}(SH)_{24}(PH_3)_8]^{2+}$

We begin by analyzing the absorption spectrum of the smallest possible box cluster, $[Ag_{46}(SH)_{24}(PH_3)_8]^{2+}$, as well as that of its bare form, Ag_{38}^{2-} The calculated absorption spectrum of the $[Ag_{46}(SH)_{24}(PH_3)_8]^{2+}$ ligand-protected cluster is shown in Figure 4.4a, and the characterizations of the five excited states with the highest coupling range values are given in Table 4.1. The spectrum of $[Ag_{46}(SH)_{24}(PH_3)_8]^{2+}$ does not feature any distinct superatomic peaks that stand out. The closest we get to plasmonic excited states are found at 2.41 and 2.45 eV, but both of these excited states have low superatomic character. The overall low superatomic character present in the absorption spectrum of $[Ag_{46}(SH)_{24}(PH_3)_8]^{2+}$ is likely a result of (1) significant localization of surface conduction electrons by interactions with ligands and (2) the relatively low ratio of occupied superatomic orbitals to ligand orbitals, which here is 0.23. The Ag_{44} thiolated cluster discussed in the previous two chapters has a similar ratio of occupied superatomic to ligand orbitals (0.20), but its spectrum has considerably more superatomic character. This may be due to

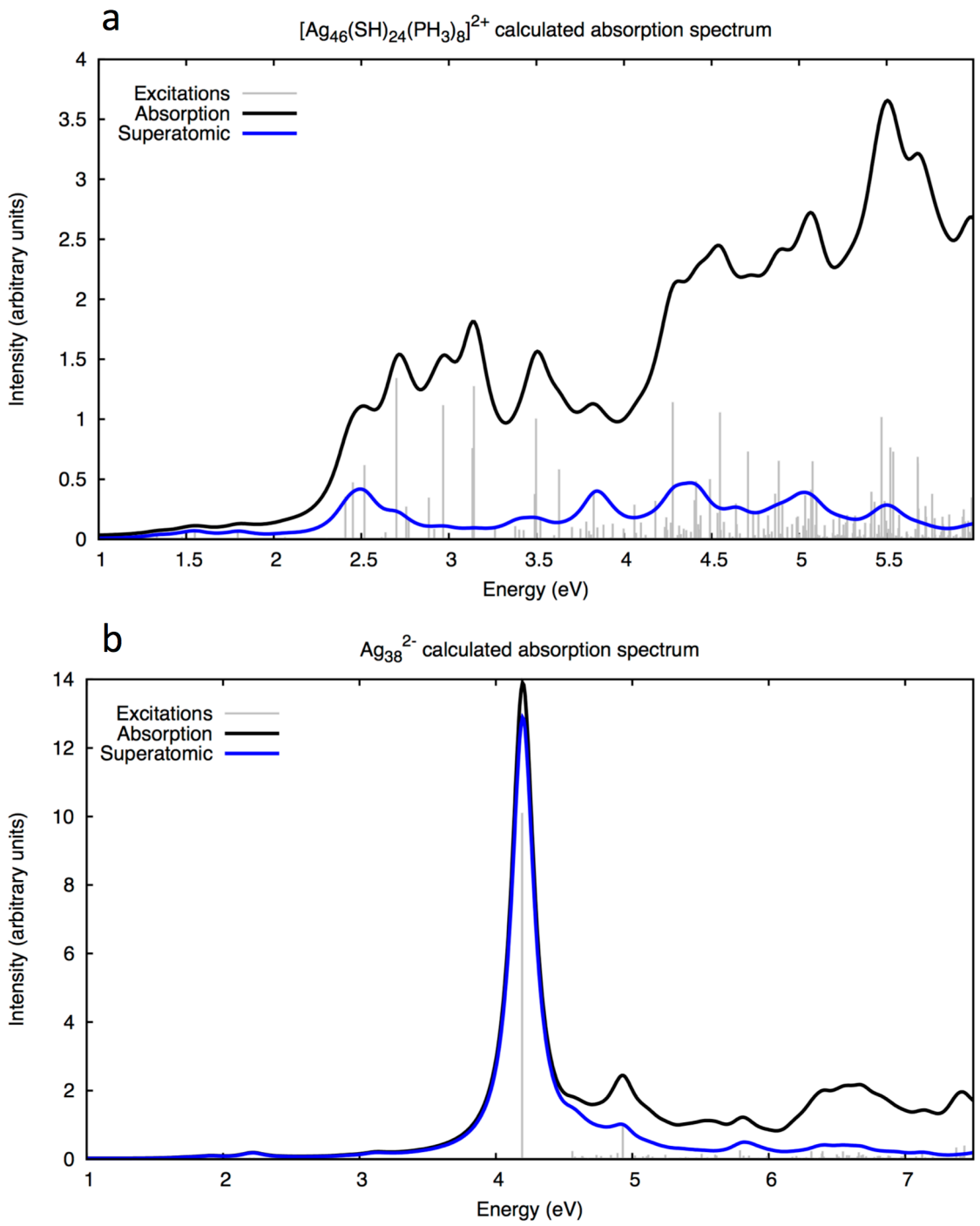

Figure 4.4. Calculated absorption spectra of (a) $[Ag_{46}(SH)_{24}(PH_3)_8]^{2+}$ and (b) Ag_{38}^{2-}.

the ways in which the ligands bind in these two clusters. In Ag_{44}, the SH units are present inside oligomeric $Ag_2S_5^{2-}$ units, where some of the interactions between S and Ag-shell atoms are mediated by the Ag atoms inside the oligomer. In $[Ag_{46}(SH)_{24}(PH_3)_8]^{2+}$, while the 8 PH_3 ligands are bound through oligomeric Ag atoms, the 24 SH units are bound directly to the cluster. This may result in a greater amount of ligand-metal interaction and greater localization of conduction electrons.

Table 4.1. Properties of the 5 excited states in the $[Ag_{46}(SH)_{24}(PH_3)_8]^{2+}$ absorption spectrum with the highest coupling range values.

Energy (eV)	Oscillator strength	Superatom (%)	Collectivity	Coupling range (eV)
2.41	0.07	45.42	3.52	0.214
2.45	0.09	40.80	3.98	0.301
2.70	0.27	14.83	10.11	0.261
2.97	0.22	6.60	5.40	0.271
3.14	0.26	3.07	2.67	0.173

As discussed above, it is not possible to directly compare ligand-protected and bare box clusters, as the only stable structures for bare box clusters have significantly larger numbers of conduction electrons than do the ligand-protected box clusters. However, it is interesting to note that the bare cluster variant of $[Ag_{46}(SH)_{24}(PH_3)_8]^{2+}$, Ag_{38}^{2-}, features a very strong plasmonic excited state, as shown in Figure 4.4b. As there is only one excited state of any interest, we do not provide a table for Ag_{38}^{2-}. The excited state visible here at 4.19 eV is extremely collective at 24.44, has very high superatomic character at 93.11, and a very high coupling range value of 0.812 eV.

That the presence of the ligands would effectively kill a plasmonic excited state is not entirely surprising. As discussed in the previous paragraph, the direct binding of the thiolate ligands to the outermost Ag atoms of the Ag_{38} “core” may result in substantial conduction electron

localization. There is no way to determine whether or not a bare Ag_{38} cluster with the same number of conduction electrons as the ligand-protected $[Ag_{46}(SH)_{24}(PH_3)_8]^{2+}$ cluster would have so strong a plasmonic excited state. However, as we will see, plasmonic excited states are clearly visible in each longer box cluster in this study. The oscillator strength of the strongly plasmonic excited state in the bare Ag_{38}^{2-} cluster is also far higher than anything in the absorption spectrum of the $[Ag_{46}(SH)_{24}(PH_3)_8]^{2+}$ cluster at a massive 4.33, compared with 0.27 for $[Ag_{46}(SH)_{24}(PH_3)_8]^{2+}$. In this case, the effect is likely a combination of localization of conduction electrons by the ligands, the much larger number of conduction electrons present in the Ag_{38}^{2-} cluster (40) than in the $[Ag_{46}(SH)_{24}(PH_3)_8]^{2+}$ cluster (20), and the extremely high collectivity of the plasmonic excited state in Ag_{38}^{2-}.

4.3.3.2 $[Ag_{67}(SH)_{32}(PH_3)_8]^{3+}$

We next consider the $[Ag_{67}(SH)_{32}(PH_3)_8]^{3+}$ cluster, the only box cluster that to our knowledge has been successfully synthesized, as well as the bare Ag_{59}^{-} cluster. The $[Ag_{67}(SH)_{32}(PH_3)_8]^{3+}$ calculated absorption spectrum (Figure 4.5a) shows two clear superatomic peaks at around 1.8 and 2.2 eV (regions A and B), with a somewhat superatomic peak at roughly 2.6 eV (region C). The excited state characterization in Table 4.2 indicates that the peaks around 1.8 and 2.2 eV represent plasmons, while that at 2.6 eV is somewhat plasmonic. It should be noted that for this and all larger box clusters, as we concern ourselves only with longitudinal plasmons, only excited states with A_{2u} symmetry are characterized, as these are longitudinal excited states. The only other dipole-allowed symmetry is E_u, representing transverse excited states.

The first three excited states in Table 4.2 are all at least moderately plasmonic, with collectivities ranging from 3.21 to 4.51 and superatomic characters above 80%. The first of these

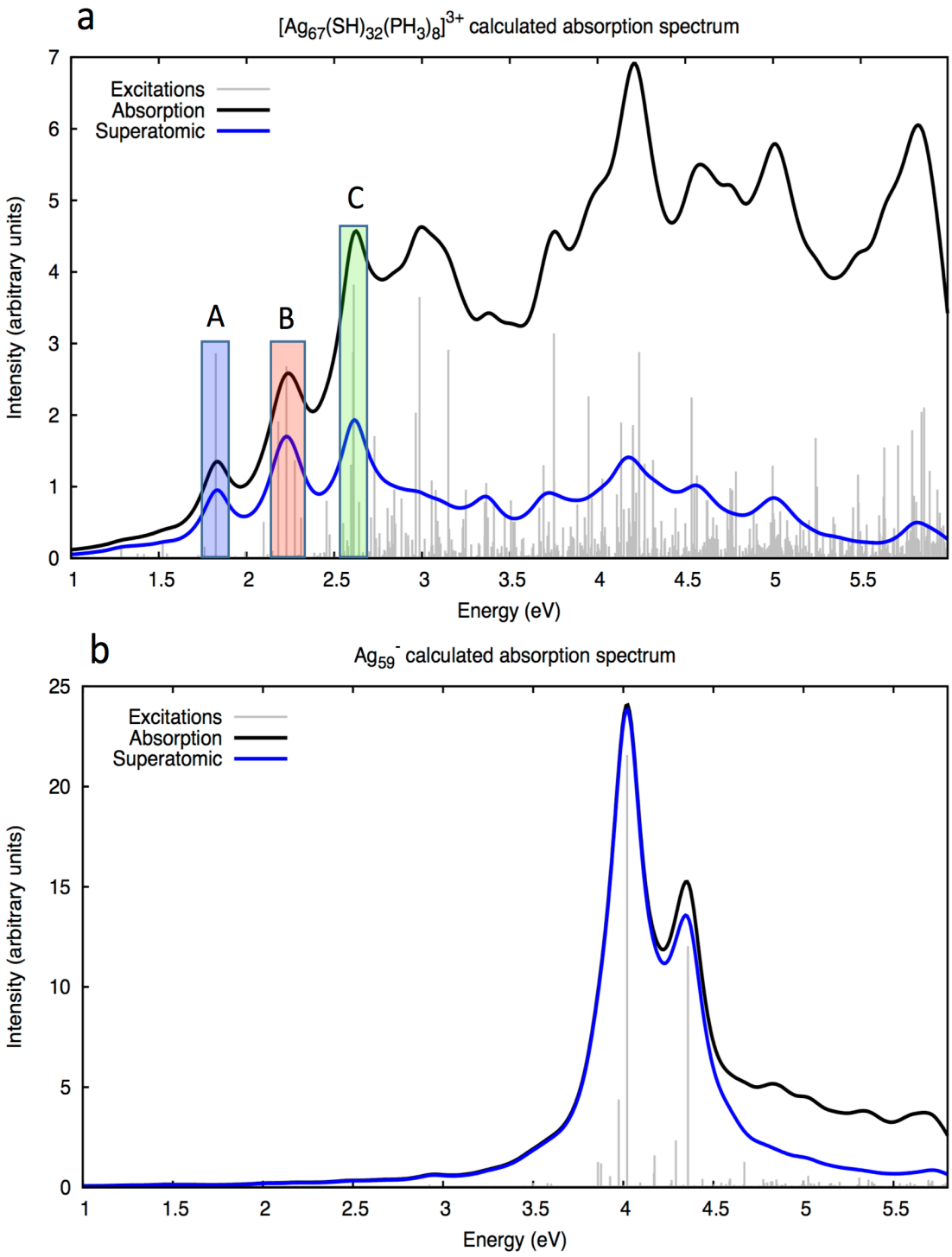

Figure 4.5. Calculated absorption spectra of (a) $[Ag_{67}(SH)_{32}(PH_3)_8]^{3+}$ and (b) Ag_{59}^-. The colored boxes and letter markings in (a) serve to aid the reader in identifying the plasmonic regions specified in the text.

Table 4.2. Properties of the plasmonic excited states of interest in the $[Ag_{67}(SH)_{32}(PH_3)_8]^{3+}$ absorption spectrum. Entries in **bold** are plasmonic or moderately plasmonic, and those in *italics* are borderline plasmonic. Letters in superscript indicate that an excited state is part of a peak labeled with the same letter in Figure 4.5a.

Energy (eV)	Oscillator strength	Superatom (%)	Collectivity	Coupling range (eV)
1.82^{A}	**0.29**	**84.01**	**4.51**	**0.337**
2.18^{B}	**0.19**	**85.96**	**3.21**	**0.277**
2.23^{B}	**0.27**	**87.80**	**4.18**	**0.285**
2.61^{C}	*0.29*	*69.07*	*3.04*	*0.204*
2.61^{C}	*0.38*	*59.44*	*4.16*	*0.179*

Table 4.3. Properties of the plasmonic excited states of interest in the Ag_{59}^- absorption spectrum.

Energy (eV)	Oscillator strength	Superatom (%)	Collectivity	Coupling range (eV)
4.02	**5.61**	**100.00**	**15.28**	**1.157**
3.97	**1.14**	**100.00**	**4.27**	**0.672**
3.88	**0.31**	**100.00**	**3.15**	**0.346**

excited states is responsible for the peak seen at about 1.8 eV in region A, while the second and third are responsible for the peak at about 2.2 eV in region B. In addition, there are two somewhat-less plasmonic excited states at 2.61 eV, making up the peak in region C. Overall, we find two clearly plasmonic peaks and a third, somewhat plasmonic peak.

The calculated absorption spectrum of the bare variant of the $[Ag_{67}(SH)_{32}(PH_3)_8]^{3+}$ cluster, Ag_{59}^-, shows a single clear longitudinal plasmon (Figure 4.5b and Table 4.3). This plasmon is composed of three plasmonic excited states, which are the three entries given in Table 4.3. Again, direct comparison of the $[Ag_{67}(SH)_{32}(PH_3)_8]^{3+}$ cluster with the bare Ag_{59}^- cluster is not possible,

given the greatly differing numbers of conduction electrons in each. Thus, it cannot be definitively shown that without the ligands present in $[Ag_{67}(SH)_{32}(PH_3)_8]^{3+}$ there would be a single clear longitudinal plasmon in the bare cluster spectrum, and that therefore the three longitudinal plasmonic peaks observed in $[Ag_{67}(SH)_{32}(PH_3)_8]^{3+}$ are the result of ligand splitting. However, given the clear plasmonic behavior observed in the non-physical Ag_{13}^{5+} and Ag_{32}^{14+} clusters in chapters 2 and 3, it is not unreasonable to assume that, in the absence of orbital splitting due to the ligands, the $[Ag_{67}(SH)_{32}(PH_3)_8]^{3+}$ absorption spectrum would show a single longitudinal plasmon. In Figure 4.5b there is also a clearly-visible transverse plasmon at 4.36 eV, but as previously stated we do not concern ourselves with transverse excited states in this study.

4.3.3.3 $[Ag_{88}(SH)_{40}(PH_3)_8]^{2-}$ through $Ag_{172}(SH)_{72}(PH_3)_8$

We now present and analyze the absorption spectra of a number of box clusters longer than $[Ag_{67}(SH)_{32}(PH_3)_8]^{3+}$, increasing in size up to $Ag_{172}(SH)_{72}(PH_3)_8$. As shown below, in most such clusters we find the same basic peak structure as we do in $[Ag_{67}(SH)_{32}(PH_3)_8]^{3+}$, in which three plasmonic peaks or regions are observed. However, at longer sizes we begin to observe additional plasmonic peaks. We also find that with increasing length the energies of these peaks or regions decrease. The largest cluster considered here, $Ag_{172}(SH)_{72}(PH_3)_8$, is an important exception to this, as is discussed below.

In the spectrum of $[Ag_{88}(SH)_{40}(PH_3)_8]^{2-}$ (Figure 4.6) we again see two clear plasmonic peaks in regions A and B, but instead of a third moderately plasmonic peak we find a more complicated mixture of excited states in region C (Table 4.4). The peak in region A is composed of a single plasmonic excited state at 1.62 eV. Region B consists of four excited states, only one of which (at 2.06 eV) has a collectivity high enough to truly be considered plasmonic, although

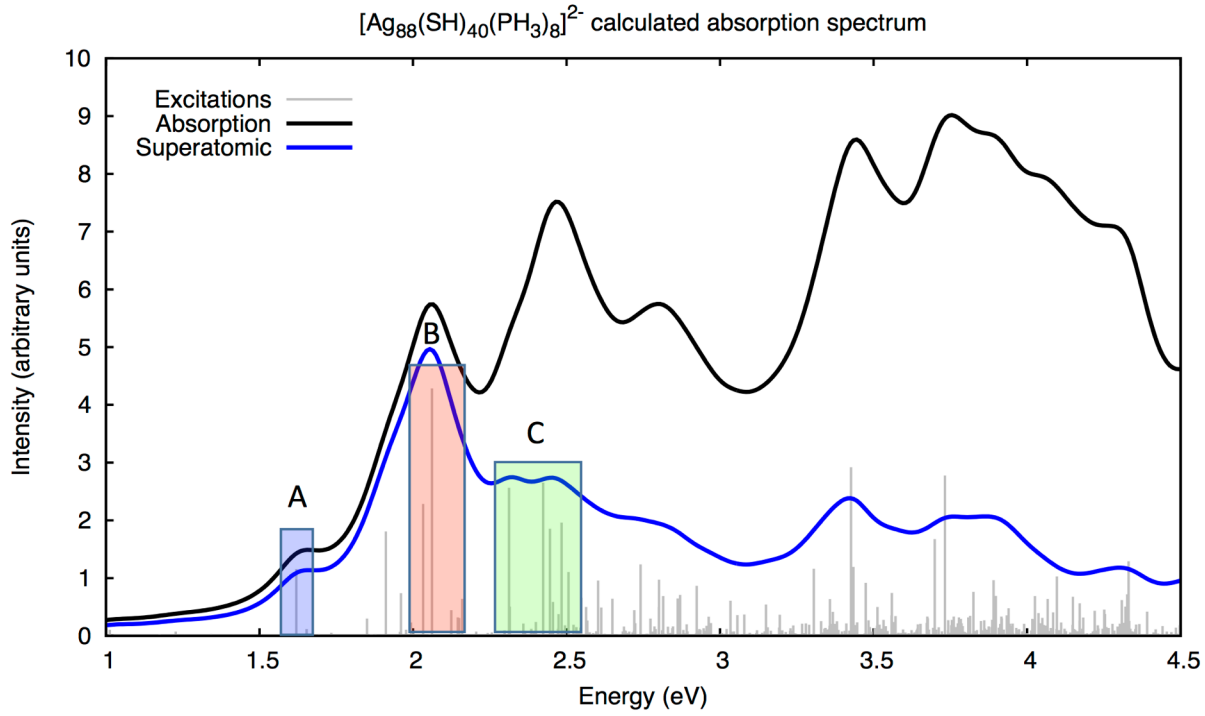

Figure 4.6. Calculated absorption spectrum of $[Ag_{88}(SH)_{40}(PH_3)_8]^{2-}$.

Table 4.4. Properties of the plasmonic excited states of interest in the $[Ag_{88}(SH)_{40}(PH_3)_8]^{2-}$ absorption spectrum.

Energy (eV)	Oscillator strength	Superatom (%)	Collectivity	Coupling range (eV)
1.62^{A}	**0.20**	**85.70**	**4.13**	**0.222**
2.03^{B}	*0.39*	*96.07*	*2.97*	*0.214*
2.06^{B}	**0.73**	**99.02**	**5.88**	**0.271**
2.15^{B}	*0.05*	*94.55*	*2.77*	*0.099*
2.16^{B}	*0.11*	*95.91*	*2.88*	*0.127*
2.31^{C}	*0.44*	*60.15*	*5.40*	*0.251*
2.44^{C}	*0.32*	*42.58*	*4.76*	*0.118*
2.55^{C}	*0.11*	*77.12*	*2.37*	*0.120*

the others are borderline plasmonic. Finally, in region C, we find three borderline plasmonic excited states, which are either lacking in superatomic character (2.31 and 2.44 eV) or lacking in collectivity (2.55 eV). These three regions are shifted down in energy relative to their counterparts

in $[Ag_{67}(SH)_{32}(PH_3)_8]^{3+}$, which is to be expected with increasing length.[117,118] In addition, we see here a significant increase in maximum oscillator strength. In the $[Ag_{46}(SH)_{24}(PH_3)_8]^{2+}$ and $[Ag_{67}(SH)_{32}(PH_3)_8]^{3+}$ clusters the highest oscillator strengths were 0.27 and 0.38 respectively, but in $[Ag_{88}(SH)_{40}(PH_3)_8]^{2-}$ the highest oscillator strength is 0.73, and two other excited states also exceed 0.38 in oscillator strength. This is not surprising, as with increasing length a larger number of conduction electrons are available to take part in plasmonic excited states, as well as a larger distance for the instantaneous dipole to build up across.

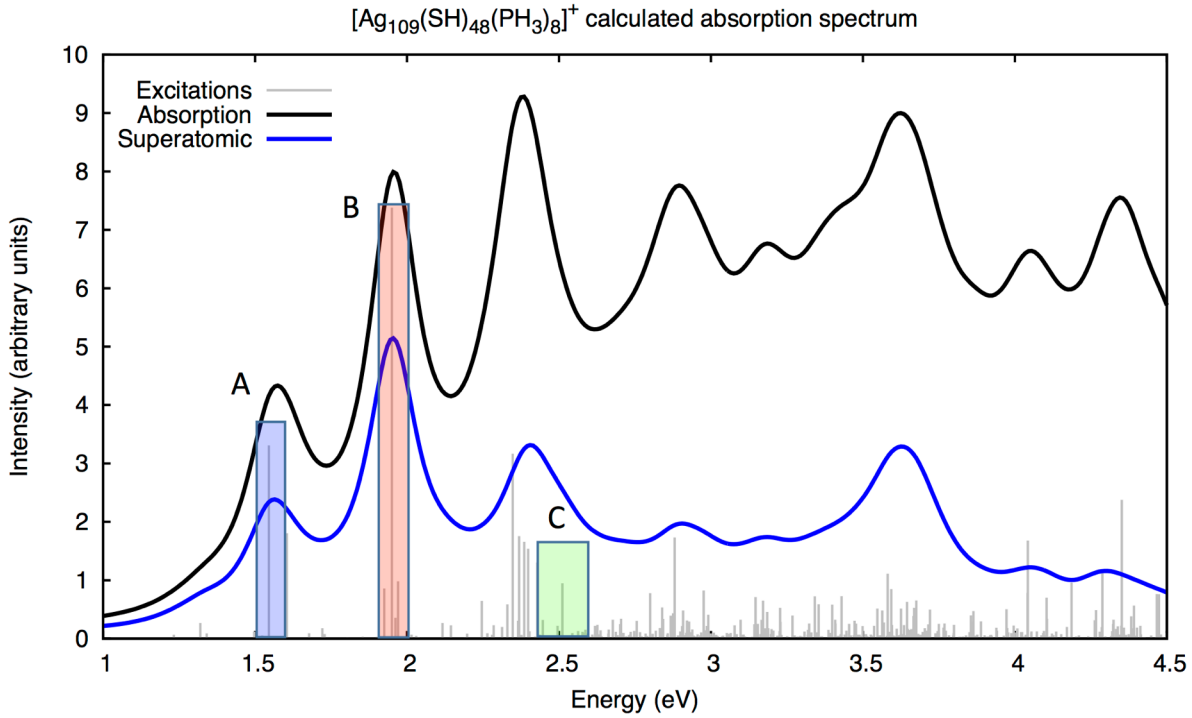

Figure 4.7. Calculated absorption spectrum of $[Ag_{109}(SH)_{48}(PH_3)_8]^+$.

We next consider the $[Ag_{109}(SH)_{48}(PH_3)_8]^+$ cluster. The absorption spectrum of $[Ag_{109}(SH)_{48}(PH_3)_8]^+$ (Figure 4.7 and Table 4.5) again follows the trend seen in $[Ag_{67}(SH)_{32}(PH_3)_8]^{3+}$ and $[Ag_{88}(SH)_{40}(PH_3)_8]^{2-}$, with three plasmonic regions shifted still lower in energy. Here we find a somewhat plasmonic excited state at 1.55 eV that makes up region A,

Table 4.5. Properties of the plasmonic excited states of interest in the $[Ag_{109}(SH)_{48}(PH_3)_8]^+$ absorption spectrum.

Energy (eV)	Oscillator strength	Superatom (%)	Collectivity	Coupling range (eV)
1.55[A]	*0.73*	*62.32*	*5.50*	*0.331*
1.95[B]	**1.62**	**77.93**	**8.33**	**0.376**
2.39[C]	*0.37*	*58.79*	*3.85*	*0.069*
2.51[C]	**0.21**	**82.35**	**3.14**	**0.089**

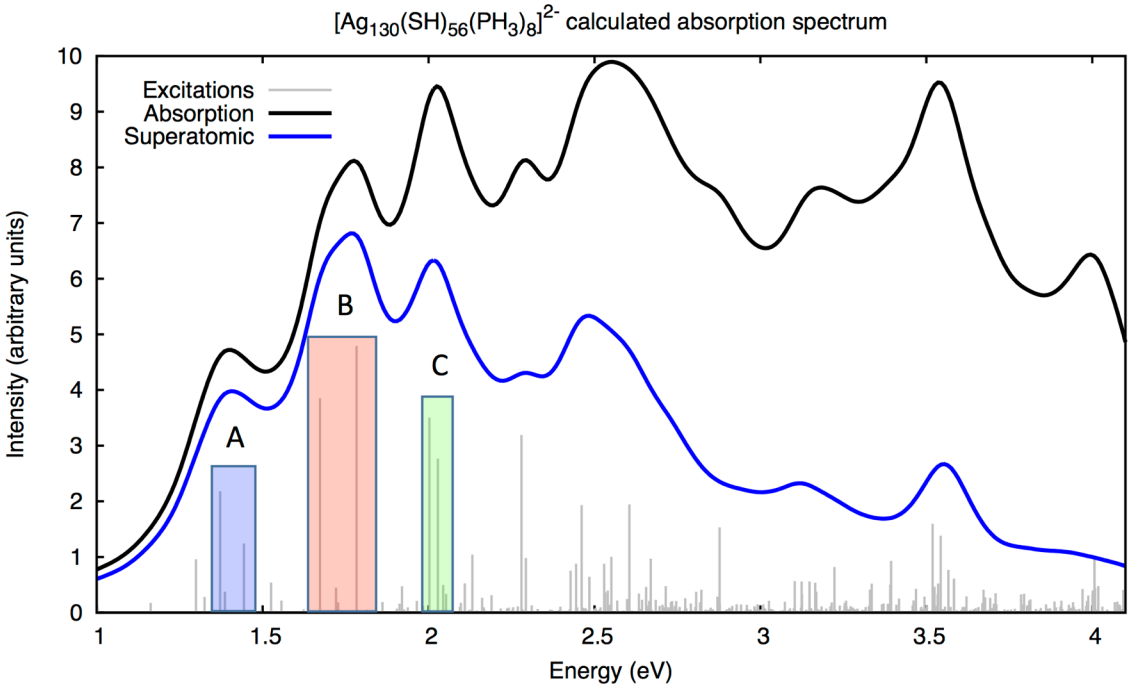

Figure 4.8. Calculated absorption spectrum of $[Ag_{130}(SH)_{56}(PH_3)_8]^{2-}$.

followed by a plasmonic excited state at 1.95 eV (region B). Finally, in region C we find a borderline plasmonic excited state at 2.39 eV and a plasmonic excited state at 2.51 eV. Notably, the coupling range values of the excited states at 1.55 and 1.95 eV are much higher than those of the two excited states in region C. This may be partly due to the higher collectivities of the former

two states, but comparison with results for shorter box clusters suggest that this is not a complete explanation.

Table 4.6. Properties of the plasmonic excited states of interest in the $[Ag_{130}(SH)_{56}(PH_3)_8]^{2-}$ absorption spectrum.

Energy (eV)	Oscillator strength	Superatom (%)	Collectivity	Coupling range (eV)
1.37[A]	**0.55**	**83.86**	**8.22**	**0.240**
1.44[A]	**0.31**	**97.91**	**4.60**	**0.167**
1.67[B]	**0.96**	**95.24**	**6.42**	**0.261**
1.78[B]	**1.20**	**93.57**	**9.29**	**0.283**
2.00[C]	**0.88**	**83.25**	**8.12**	**0.220**
2.03[C]	*0.69*	*68.92*	*5.41*	*0.136*
2.13[C]	*0.26*	*70.98*	*3.46*	*0.069*
2.30	*0.86*	*49.42*	*7.95*	*0.077*
2.59	**0.76**	**79.79**	**6.06**	**0.050**

The spectrum of $[Ag_{130}(SH)_{56}(PH_3)_8]^{2-}$ (Figure 4.8 and Table 4.6) breaks from the observed trend to this point. While we can still identify the three plasmonic regions seen in shorter box clusters, and while those regions are lower in energy than their respective counterparts in the spectra of the shorter box clusters, we also find two plasmonic excited states at energies higher than any of these three regions. Region A consists of two clearly plasmonic excited states at 1.37 and 1.44 eV, and region B consists of two other clearly plasmonic excited states at 1.67 and 1.78 eV. Region C contains one clear plasmonic state at 2.00 eV as well as two somewhat plasmonic states at 2.03 and 2.13 eV. We then find a somewhat plasmonic excited state at 2.30 eV and a plasmonic excited state at 2.59 eV, both of which have low coupling range values compared to most of the other excited states shown in Table 4.6.

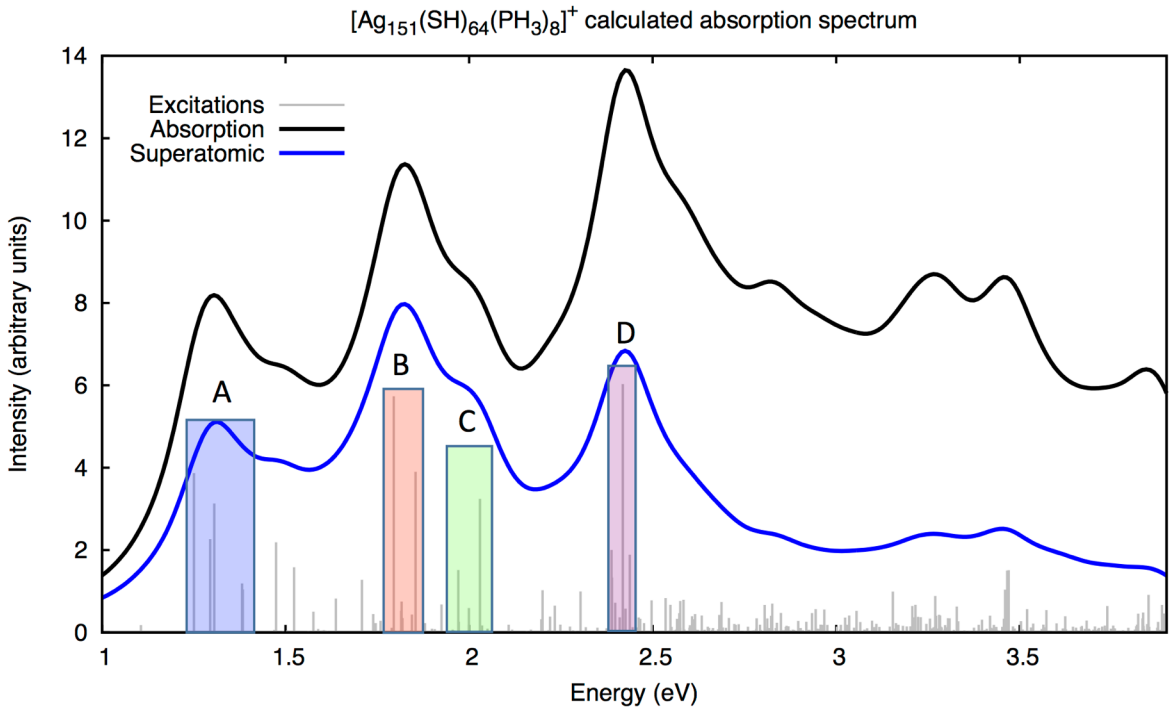

Figure 4.9. Calculated absorption spectrum of $[Ag_{151}(SH)_{64}(PH_3)_8]^+$.

In $[Ag_{151}(SH)_{64}(PH_3)_8]^+$ (Figure 4.9 and Table 4.7), we once more see three plasmonic regions, slightly lower in energy than the respective regions in the spectra of each of the shorter box clusters. However, we also see two additional somewhat plasmonic excited states at higher energies. Unlike the "extra" plasmonic excited states in $[Ag_{130}(SH)_{56}(PH_3)_8]^{2-}$, these two states are very close in energy, and could be considered a fourth plasmonic region, region D. Region A consists of three plasmonic states at 1.29, 1.31, and 1.47 eV, along with a borderline plasmonic state at 1.38 eV. Region B contains plasmonic states at 1.71, 1.79, and 1.85 eV, and region C contains plasmonic states at 1.97 and 2.03 eV. The two somewhat plasmonic states in region D are at 2.42 and 2.44 eV. The presence of four plasmonic regions in the $[Ag_{151}(SH)_{64}(PH_3)_8]^+$ spectrum, as well as that of the two "extra" plasmonic excited states in $[Ag_{130}(SH)_{56}(PH_3)_8]^{2-}$, suggests that as the lengths of the box clusters increase, orbital splitting due to ligand effects does not diminish. Indeed, rather than see three regions become two or one, we have thus far seen three become four.

Table 4.7. Properties of the plasmonic excited states of interest in the $[Ag_{151}(SH)_{64}(PH_3)_8]^+$ absorption spectrum.

Energy (eV)	Oscillator strength	Superatom (%)	Collectivity	Coupling range (eV)
1.29[A]	**0.49**	**79.26**	**4.27**	**0.199**
1.31[A]	**0.67**	**77.20**	**3.39**	**0.246**
1.38[A]	*0.22*	*54.31*	*3.34*	*0.137*
1.47[A]	**0.47**	**86.75**	**3.39**	**0.179**
1.71[B]	**0.27**	**88.39**	**6.87**	**0.093**
1.79[B]	**1.23**	**85.16**	**6.65**	**0.249**
1.85[B]	**0.84**	**83.68**	**2.93**	**0.187**
1.97[C]	**0.32**	**91.47**	**3.62**	**0.070**
2.03[C]	**0.70**	**84.62**	**4.89**	**0.147**
2.42[D]	*1.29*	*58.83*	*10.08*	*0.055*
2.44[D]	*0.41*	*92.62*	*2.90*	*0.056*

We finally see a dramatic change in the absorption spectrum of $Ag_{172}(SH)_{72}(PH_3)_8$ (Figure 4.10 and Table 4.8). Unlike every other box cluster presented thus far, we find only one strongly plasmonic excited state in the $Ag_{172}(SH)_{72}(PH_3)_8$ spectrum, which is at 1.34 eV. The oscillator strength of this excited state is 3.71, three times higher than the highest values found in either $[Ag_{130}(SH)_{56}(PH_3)_8]^{2-}$ or $[Ag_{151}(SH)_{64}(PH_3)_8]^+$. The other excited state with high oscillator strength, which is at 1.66 eV, has a collectivity below 2.00, and is therefore not at all plasmonic. Rather, it is similar to the strong excited state observed at 2.65 eV in the $Ag_{25}(SH)_{18}^-$ cluster (see Figure 3.4a and Table 3.2), which also has high intraband/superatomic character but is not at all collective.

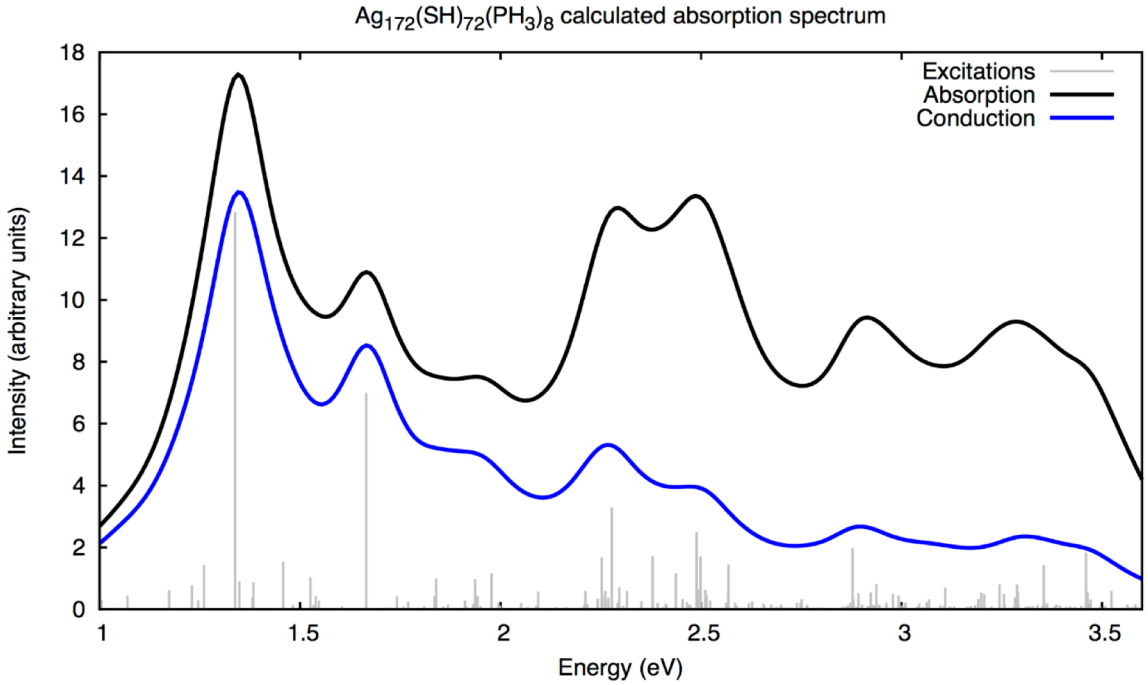

Figure 4.10. Calculated absorption spectrum of $Ag_{172}(SH)_{72}(PH_3)_8$.

Table 4.8. Properties of two excited states of interest in the $Ag_{172}(SH)_{72}(PH_3)_8$ absorption spectrum.

Energy (eV)	Oscillator strength	Superatom (%)	Collectivity	Coupling range (eV)
1.34	**3.71**	**79.09**	**10.00**	**0.399**
1.66	2.02	93.72	1.88	0.275

Interestingly, this single plasmonic excited state observed in $Ag_{172}(SH)_{72}(PH_3)_8$, which has a high superatomic character and a very high collectivity, has a coupling range of 0.40 eV, while the highest coupling range found among the excited states in the $[Ag_{46}(SH)_{24}(PH_3)_8]^{2+}$ absorption spectrum is 0.30 eV, for an excited state with a superatomic character of only 40.80%. In the box clusters between $[Ag_{46}(SH)_{24}(PH_3)_8]^{2+}$ and $Ag_{172}(SH)_{72}(PH_3)_8$ in length we find maximum coupling range values between 0.30 and 0.40 eV, and some below 0.30 eV. While we find that coupling range works well as a comparative metric within a set of excited states of one cluster, it

is not particularly meaningful when used to compare excited states of different clusters. One scenario in which we might actually be able to see increasing coupling range values would be if we were able to expand cluster size in three dimensions, quickly reducing the significance of ligand effects. However, it does not seem that ligand effects are notably reduced in significance as we move from $[Ag_{46}(SH)_{24}(PH_3)_8]^{2+}$ to $Ag_{172}(SH)_{72}(PH_3)_8$.

The sudden convergence of the multiple plasmonic regions shown from $[Ag_{67}(SH)_{32}(PH_3)_8]^{3+}$ through $[Ag_{151}(SH)_{64}(PH_3)_8]^{+}$ to a single plasmon in $Ag_{172}(SH)_{72}(PH_3)_8$ suggests that this single plasmon may be anomalous. It is very possible that, were we able to study the next largest box cluster, $Ag_{193}(SH)_{80}(PH_3)_8$, we would find three or four plasmonic regions once again. Indeed, there is little reason to believe otherwise. While we have continually increased box cluster length, thus reducing the impact of the ligands bound to each "end piece" of the clusters, we have not altered cluster thickness, and thus the splitting effects of the ligands wrapped around the sides of the clusters is not reduced. With enough length, it is possible that there may simply be so many orbitals packed so tightly in energy that the effects of splitting become negligible, but clearly this is not the case in the length scale studied here.

The localization of conduction electrons originating on Ag atoms in the cluster shell also does not reduce significantly with increasing length, for much the same reason as splitting is not significantly reduced. If the box clusters are roughly approximated as cylinders, we can consider the surface area to be equal to $2\pi r^2 + 2\pi rh$, while volume is equal to $\pi r^2 h$. The ratio of the two values does not change quickly with increasing length and constant radius, and thus the surface region, which for each box cluster is completely covered in ligands, does not become particularly less significant.

Furthermore, we observe a general increase in oscillator strength with increasing length in the ligand-protected box clusters. The highest oscillator strength found in the absorption spectrum of $[Ag_{46}(SH)_{24}(PH_3)_8]^{2+}$ is 0.27, while that of $Ag_{172}(SH)_{72}(PH_3)_8$ is 3.71, and the second-highest oscillator strength in the $Ag_{172}(SH)_{72}(PH_3)_8$ spectrum is 2.02. While this trend is not monotonic throughout this study, it does demonstrate that even though at each length studied here the plasmonic excited states are significantly affected by ligands, they do become stronger with increasing length.

4.4 Conclusions

We performed DFT and TDDFT calculations on a number of ligand-protected Ag box clusters of various lengths, from $[Ag_{46}(SH)_{24}(PH_3)_8]^{2+}$ up to $Ag_{172}(SH)_{72}(PH_3)_8$, to study changes in plasmonic behavior with increasing length. We applied the plasmonic indicator method (PIM) to analyze the excited states of the various box clusters and to identify plasmons. We found that, while $[Ag_{46}(SH)_{24}(PH_3)_8]^{2+}$ does not have any plasmonic excited states, every box cluster from $[Ag_{67}(SH)_{32}(PH_3)_8]^{3+}$ through $[Ag_{151}(SH)_{64}(PH_3)_8]^{+}$ has three or four separate plasmonic regions of varying sharpness. We found that the $Ag_{172}(SH)_{72}(PH_3)_8$ cluster has only one strongly plasmonic excited state, but the suddenness of the change from multiple plasmons to one and the barely-changing surface-to-volume ratio of the cluster with increasing length suggest that this may be an anomaly.

This study indicates that while one-dimensional extensions of the experimentally-synthesized $[Ag_{67}(SH)_{32}(PH_3)_8]^{3+}$ clusters do have plasmonic excited states that red-shift with increasing length, simply extending this structure without increasing thickness is unlikely to produce structures that can overcome ligand effects to show a single, strong plasmon that is at all

similar to those observed in many bare clusters. While it would be far more computationally expensive, in the future it would be interesting to extend the box cluster structure in the x and y dimensions as well to more dramatically experiment with changing the magnitude of ligand effects.

CHAPTER 5

Hydrogenation of CO to Methanol on Ni(110) with and without Subsurface Hydrogen

5.1. Introduction

The hydrogenation of CO is an extremely important reaction in many contexts, and it has attracted considerable recent interest. This process can, in various conditions, produce methanol, formaldehyde, and methane, in addition to other hydrocarbons. CO hydrogenation is a vital process in industrial synthesis through the Fischer-Tropsch process[10,122] as well as some CO_2 capture processes,[11] and it can occur in significant amounts in reactions in which CO is a product and a source of H atoms is present.[123,124]

Synthetic hydrocarbons can be obtained via conversion of "synthesis gas" or "syngas", which is composed of CO and H_2, by hydrogenating CO to produce alkanes.[125,126] Syngas itself is often produced via the dry reforming reaction, in which CO_2 and methane (or some other hydrocarbon) are the primary reactants, turning two greenhouse gases into synthetically useful chemicals.[127] In this context, hydrogenation of CO is a subsequent reaction that can occur between the reactant H_2 gas and the product CO gas. Either methane or methanol can be a desirable outcome of CO hydrogenation in this scenario. Thus, the reaction of CO with H_2 is very important, both industrially and environmentally, and control of the ratio between the production of methane, methanol, and formaldehyde is of great interest.

Commonly-used catalyst surfaces for CO hydrogenation include Cu, Co, and Ni. Methanol production is highly favored by Cu catalysts, as the key step in the methanation process, C-O bond breaking, is highly unfavorable. In contrast, Co catalysts strongly favor methane production, as barriers for methanol production are much higher than on Cu surfaces, and C-O dissociation occurs far more readily. Between these two catalysts we find Ni, which occupies a middle ground.[128] Previous experimental studies have shown Ni to be an active catalyst for CO methanation,[129,130] but theoretical studies have suggested that methanol production is a strong possibility on Ni surfaces as well.[131,132] While the Ni(111) surface is the most well-studied, Ni step-edges and other coordination-unsaturated sites are significantly more reactive, and the Ni(110) surface is a fair approximation of these unsaturated sites.[132,133] The most direct experimental study thus far of CO hydrogenation on Ni(110) is a recent study by Roiaz et al.,[134] which demonstrates the presence of two intermediates of the CO methanation process present on the Ni surface.

While the hydrogenation reactions of CO and CO_2 have been studied in great detail, few theoretical studies have explicitly considered the role of subsurface hydrogen. The importance of subsurface hydrogen to the hydrogenation of hydrocarbons adsorbed onto surfaces was initially demonstrated by Johnson et al. in 1992.[135] Subsurface hydrogen, also called bulk hydrogen when it is present more than one layer below the surface, can typically be formed in a material through two mechanisms: (i) impact of individual H atoms on the surface with sufficient energy to overcome a significant barrier (roughly 1 eV on a Ni(111) surface) to entering the subsurface, and (ii) collision of some inert gas atom or molecule with an H atom adsorbed on the surface with sufficient energy to pound it into the subsurface.[136,137] Subsurface hydrogen atoms must overcome an energy barrier to return to the surface and undergo reaction. However, once this barrier is overcome the H atom will have a significant amount of kinetic energy (in our calculations, about

0.5-0.6 eV on a Ni(110) surface), greatly increasing its reactivity and helping the system to overcome further energetic barriers.[138,139]

In addition to this kinetic effect, the presence of subsurface hydrogen as a spectator in a surface reaction rather than a participant can significantly alter the energetics of that reaction. Subsurface hydrogen has been shown in many cases to increase the binding energy of surface adsorbates.[12,140,141] This occurs both through altering the electronic structure of the surface as well as through distortion of the surface structure. As this stabilization effect varies from adsorbate to adsorbate and binding site to binding site, the relative energies of initial states, transition states, and final states in reaction pathways can be altered in ways that are difficult to predict.

The role of subsurface hydrogen in altering the energetics for the hydrogenation of CO_2 on Ni(110) and Ni(111) surfaces was first shown by Peng et al.,[140,141] who calculated reaction barriers for CO_2 hydrogenation to formic acid on these two surfaces both with subsurface hydrogen and without (in which case the reactant was surface hydrogen). These studies found very little impact of subsurface hydrogen on the barriers of the reaction pathway when acting as a spectator. However, when subsurface hydrogen atoms emerged to the surface and became reactants, the authors found that the lower stability of subsurface hydrogen atoms relative to those on the surface greatly changed the overall thermodynamics of the hydrogenation pathway. This effect was significant enough that the authors found that in both cases, while hydrogenation of CO_2 to formic acid was endothermic in the absence of subsurface hydrogen, it became exothermic in the presence of subsurface hydrogen.

This work was expanded upon several years later by Lin et al.[12], who performed similar calculations to study hydrogenation of CO_2 to give CO + H_2O with and without subsurface hydrogen on a Ni(110) surface. In contrast to Peng et al., Lin et al. found that even as a spectator,

subsurface hydrogen altered reaction barriers enough to be considered a significant factor. The authors found that the presence of subsurface hydrogen changed which mechanism was most favorable – the associative mechanism for CO_2 hydrogenation was favored in the absence of subsurface hydrogen, but the presence of subsurface hydrogen favored the redox mechanism.

In the present work, we apply a methodology similar to that of Lin et al., turning our focus now to another important reaction and a likely subsequent reaction of CO_2 hydrogenation, the hydrogenation of CO to give methane, methanol, and/or formaldehyde. We investigate the energetics of the various reaction pathways leading to these products in the presence and absence of subsurface hydrogen. Like Lin et al., we study the effects of subsurface hydrogen both as a participant and as a spectator to the relevant reaction steps. We also build upon the work of Fajín et al.,[131] who studied reactions of CO with surface hydrogen on Ni(110). However, in our study, in addition to considering the effects of subsurface hydrogen, we explore a greater number of potential reaction steps and pathways than previously considered, and we do so using a larger unit cell.

There are four possible pathways involving sequential hydrogenation of CO that each produce methanol. Each intermediate along these four pathways can undergo C-O dissociation, a key and necessary step for methane formation. We compare each of these four pathways against each other, both with and without subsurface hydrogen. We show that based on relative energies of the relevant steady and transition states, what we call Pathway 1, the pathway in which CO is hydrogenated to H_3CO before a final hydrogenation of O to give methanol, is the most favorable pathway, and that in this pathway methanol production is at each step favored over methane production. While subsurface hydrogen is shown to both lower and raise various barriers, we find

that it does so without a simple pattern, and that the effect of subsurface hydrogen on the relative propensities of the various pathways and of methane and methanol is at best small.

5.2. Computational Methods

All calculations in this study were performed with spin-polarized density functional theory (DFT) with periodic boundary conditions as implemented in the Vienna Ab initio Simulation Package (VASP), version 5.3.5.[142,143] The Perdew, Burke, and Ernzerhof (PBE)[144] exchange-correlation functional was used to model exchange and correlation interactions, while electron-ion interactions were modeled using projector-augmented wave (PAW) potentials.[145,146] Structural relaxation calculations were performed using the conjugate gradient method, while transition states and reaction barriers were calculating using the climbing image nudged elastic band (CI-NEB) method.[147,148] The CI-NEB method involves relaxing the structures of a series of images that lie along the reaction coordinate between the initial and final reaction states, which have already been relaxed to energy minima. During this relaxation, a potential is applied along the reaction coordinate, allowing the images to converge to what would normally be non-steady states. Transition states were verified using vibrational frequency calculations.

The Ni(110) surface used in this study is a 2x3 unit cell with 6 Ni atoms per layer and 7 layers. The bottom three layers were constrained to maintain the bulk Ni structure, while the top 4 layers were allowed to relax. The unit cell also contained about 12 Å of vacuum between the uppermost Ni layer and the upper boundary (in the positive z direction) to avoid electronic interactions between vertically-neighboring cells. A 4x3x1 Monkhorst-Pack mesh was used for **k**-sampling of the Brillouin zone.[149]

5.3. Results and Discussion

In this study, the presence of subsurface hydrogen (denoted H_{sub}) in the Ni(110) surface is modeled as a monolayer of H_{sub} in octahedral (O_h) sites just below the surface, as previous work by Lin et al.[12] has shown that H_{sub} is most stable in O_h sites. A full monolayer consists of six H_{sub} atoms, as there are six O_h sites available just below the surface of Ni(110) in the 2x3 unit cell used here. In addition, as a shorthand similar to H_{sub}, we refer to surface hydrogen as H_s.

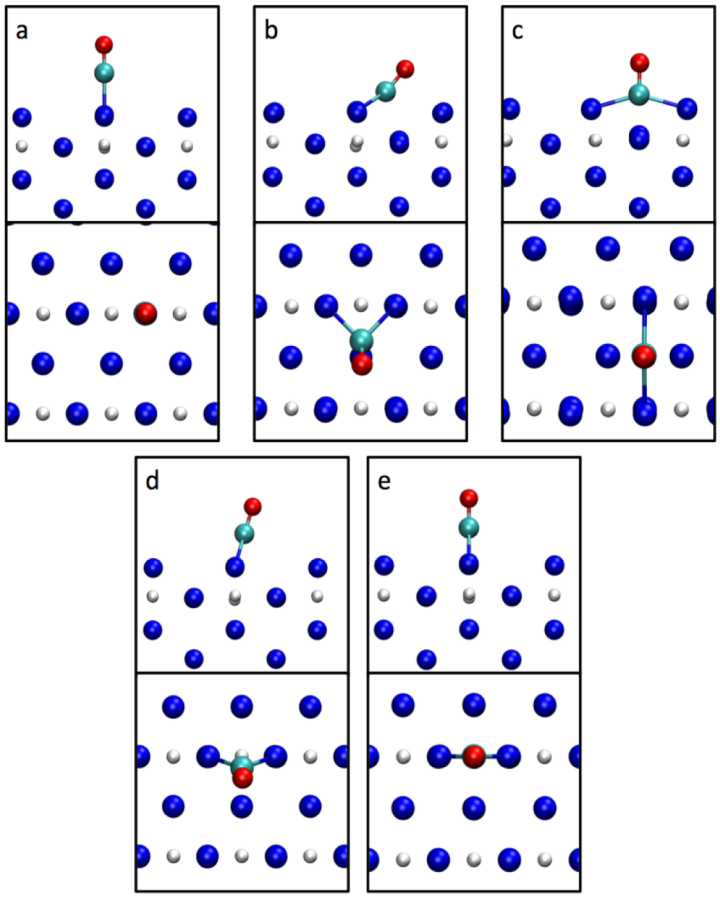

Figure 5.1. Relaxed structures of CO bound to (a) atop, (b) hollow, (c) long-bridge, (d) pseudo-threefold, and (e) short-bridge sites, from (top) a side view and (bottom) a top-down view. Only the H_{sub} case is shown here.

Table 5.1. Binding energies for CO at various binding sites on the Ni(110) surface, both with and without H_{sub}.

Binding site	$E_{binding,\ no\ sub}$ (eV)	$E_{binding,\ sub}$ (eV)
Atop	-1.71	-1.89
Hollow	-1.73	-1.9
Long-bridge	-1.49	-1.75
Pseudo-threefold	-1.41	-2.08
Short-bridge	-1.9	-2.11

5.3.1 Binding energies

We first consider the impact of subsurface hydrogen on the binding energies of CO, H, and the various intermediates along the reaction pathways towards the formation of methanol and methane on the Ni(110) surface.

As discussed above, subsurface hydrogen alters binding energies by 1) altering the electronic structure of the surface and 2) distorting the crystal structure of the surface. We begin by identifying the Ni(110) surface site to which CO binds most strongly, both with and without subsurface hydrogen. Binding energies for CO were calculated at each of the five surface sites present in a (110) surface: Pseudo-threefold, short-bridge, long-bridge, hollow, and atop. CO is displayed in the various binding sites in Figure 5.1 (only shown with subsurface hydrogen present), and the results of the binding energy calculations are presented in Table 5.1. It should be noted that the image of CO bound in a pseudo-threefold site (Figure 5.1d) actually shows a site somewhere between pseudo-threefold and short-bridge, which was the minimum-energy structure found from a structural relaxation calculation beginning with CO in the pseudo-threefold position. When subsurface hydrogen is not present, the calculated minimum-energy structure is more clearly

pseudo-threefold. The preferred binding site is found, in both the subsurface and non-subsurface cases, to be the short-bridge site. In addition, our research group has previously shown that the most stable binding site for a hydrogen atom on a Ni(110) surface, again both with and without subsurface hydrogen, is the pseudo-threefold site.[12]

The binding energies of the various intermediates along the pathways discussed in this study are shown in Table 5.2. It should be noted that, other than CO, none of the reported binding energies with subsurface hydrogen are calculated with a full monolayer of six H_{sub} atoms. Rather, as the reaction pathways proceed, H_{sub} atoms come out of the subsurface monolayer and take part in reactions on the surface. These H_{sub} atoms are not replaced. Therefore, the H_{sub} monolayer becomes depopulated as the reaction progresses. While this does decrease the impact of H_{sub} on the system as a whole, in all cases there remains at least one H_{sub} atom directly below the adsorbate. Previous work has shown the H_{sub} atoms just below an adsorbate to have the largest impact on binding energy.[12]

Table 5.2. Binding energies for the various intermediates along the possible reaction pathways between CO and H_3COH, both with and without H_{sub}.

Adsorbate	$E_{binding,\ no\ sub}$ (eV)	$E_{binding,\ sub}$ (eV)
CO	-1.91	-2.12
HCO	-2.60	-2.91
COH	-4.01	-4.27
HCOH (trans)	-3.25	-3.42
HCOH (cis)	-3.51	-3.69
H_2CO	-1.25	-1.51
H_3CO	-2.56	-2.72
H_2COH	-1.68	-1.83
H_3COH	-0.45	-0.48

Notably, we find that the presence of subsurface hydrogen increases (as in, makes more negative) binding energy in all cases. This is in agreement with our previous work.[12] The presence of H_{sub} alters the electronic structure of the metal surface through shifting of the *d*-band, leading to stabilization of all of the adsorbates considered here. The degree of stabilization is not uniform, ranging from ~6% in the cases of H_3CO and COH to ~21% in the case of H_2CO. One important factor here may be the ways in which H_{sub} atoms distort the Ni(110) surface, which could either increase or decrease binding energy depending on the shape and binding behavior of the adsorbate.

5.3.2 Reaction pathways

The various reaction pathways in play in this study can be thought of as pathways towards the production of methanol via hydrogenation of C and O in which each intermediate can also undergo C-O bond breaking. If the C-O bond is broken, the resulting C- and O-based species can undergo hydrogenation to give methane and water. In accordance with this picture, we consider four main pathways to methanol production:

$CO \rightarrow HCO \rightarrow H_2CO \rightarrow H_3CO \rightarrow H_3COH$ (Pathway 1)

$CO \rightarrow HCO \rightarrow H_2CO \rightarrow H_2COH \rightarrow H_3COH$ (Pathway 2)

$CO \rightarrow HCO \rightarrow HCOH \rightarrow H_2COH \rightarrow H_3COH$ (Pathway 3)

$CO \rightarrow COH \rightarrow HCOH \rightarrow H_2COH \rightarrow H_3COH$ (Pathway 4)

These pathways share some steps with one another, but they differ in the ordering of C- and O-hydrogenation steps. We consider methane production in the context of these four pathways, where each intermediate can either undergo further hydrogenation towards methanol production or C-O dissociation resulting in methane production. It should be noted that the hydrogenation reactions of C and O to CH_4 and H_2O on a Ni(110) surface have been previously studied.[131] As

these reactions themselves are not of particular interest, we do not detail them in this study. In our model we assume that C-O dissociation leads to methane production.

Here we endeavor to compare the energetics of hydrogenation and C-O bond breaking for each intermediate in each pathway, both with and without subsurface hydrogen. However, this comparison between the surface and subsurface pathways presents several significant challenges in presentation, requiring a number of simplifications and adjustments. First, in our scheme for modeling H_{sub} we begin with a full monolayer of six H_{sub} absorbed below the surface. For our calculations involving only H_s rather than H_{sub}, each reactant H_s is adsorbed to the surface just before it reacts. In the formation of H_3COH, this means that in the H_s case the overall energy of the system is lowered by the binding energy of H_s (about -2.6 eV, varying with binding site and the identity of the co-adsorbate) before each step, while in the H_{sub} case each reactant H_{sub} is already bound. To ease comparison between the surface and subsurface cases, in each figure in which we show pathways involving H_s (Figures 5.2, 5.6, 5.8, and 5.10) we consider four reactant H_s atoms to all be bound to the surface from the very first step, even though in our calculations only one H_s is bound at a time. Thus, the energetic interactions associated with co-adsorption of multiple H_s atoms are ignored as if the non-reactant H_s atoms are bound but at some significant distance from the reaction.

Second, many of the key reaction steps we discuss have multiple barriers, usually involving one or both reactants shifting between binding sites to facilitate the reaction, or in the case of HCOH, flipping from the more stable *trans* configuration in which it is formed to the more reactive *cis* configuration. When we present the energetics of the various pathways in this study, we show only the highest barrier for each reaction step, but the ΔE we present is the overall ΔE of the entire reaction step.

Finally, in the H_{sub} pathways, every other reaction step is neither hydrogenation nor C-O bond breaking, but instead is the emergence of one H_{sub} atom onto the surface, where it can then take part in a hydrogenation reaction. As such, each hydrogenation reaction step begins with one H atom on the surface, but as this is not necessary for C-O bond breaking, each C-O bond breaking reaction step begins with no H atoms on the surface. As we are interested in comparing hydrogenation and C-O bond breaking steps directly, in the figures in which we show pathways involving H_{sub} (Figures 5.3, 5.7, 5.9, and 5.11) we consider each C-O bond breaking reaction to occur in the presence of a co-adsorbed surface hydrogen atom (this being a H_{sub} atom that emerged from the subsurface monolayer), even though this is not the case in the relevant calculations themselves. Again, this non-reacting H atom can be considered to be far away from the adsorbate.

The total energy change for the formation of H_3COH from CO and four H atoms is 1.18 eV (Figure 5.2) when those H atoms begin adsorbed to the Ni(110) surface, and -0.54 eV (Figure 5.3) when those H atoms begin as H_{sub} atoms (along with two additional H_{sub} atoms that remain as passive participants). If H_3COH then desorbs from the surface into the gas phase, these energy changes are 1.63 and -0.06 eV, respectively. Comparison of the pathways with and without H_{sub} clearly shows that, regardless of which pathway is followed, the formation of H_3COH is far more thermodynamically favorable when the reactant H atoms are H_{sub}. This is because each time a H_{sub} atom emerges to the surface before reacting, the energy of the system is lowered by roughly 0.5 to 0.6 eV, which has been noted in previous studies.[12,140,141]

We will discuss each of the four pathways presented above and consider the relative energetics for each intermediate of hydrogenation or C-O bond breaking, both with and without subsurface hydrogen, and compare them with one another. As a convenient reference, the reaction barriers and energies of each reaction step discussed below are also shown in Table 5.3.

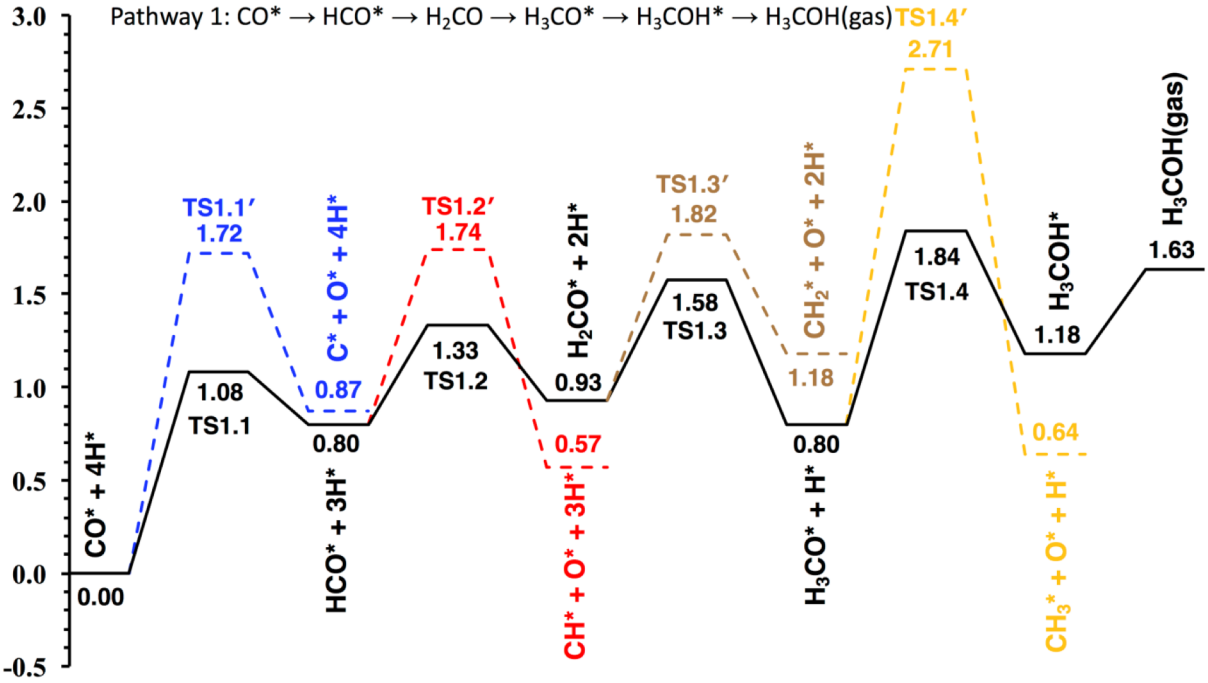

Figure 5.2. Energy diagram for Pathway 1 when subsurface hydrogen is not present. Each dashed line represents an offshoot of Pathway 1 in which the C-O bond breaks, leading, eventually, to the formation of methane and water. The colors are present to make the offshoots more visually distinguishable from one another. An asterisk (*) denotes an adsorbed species.

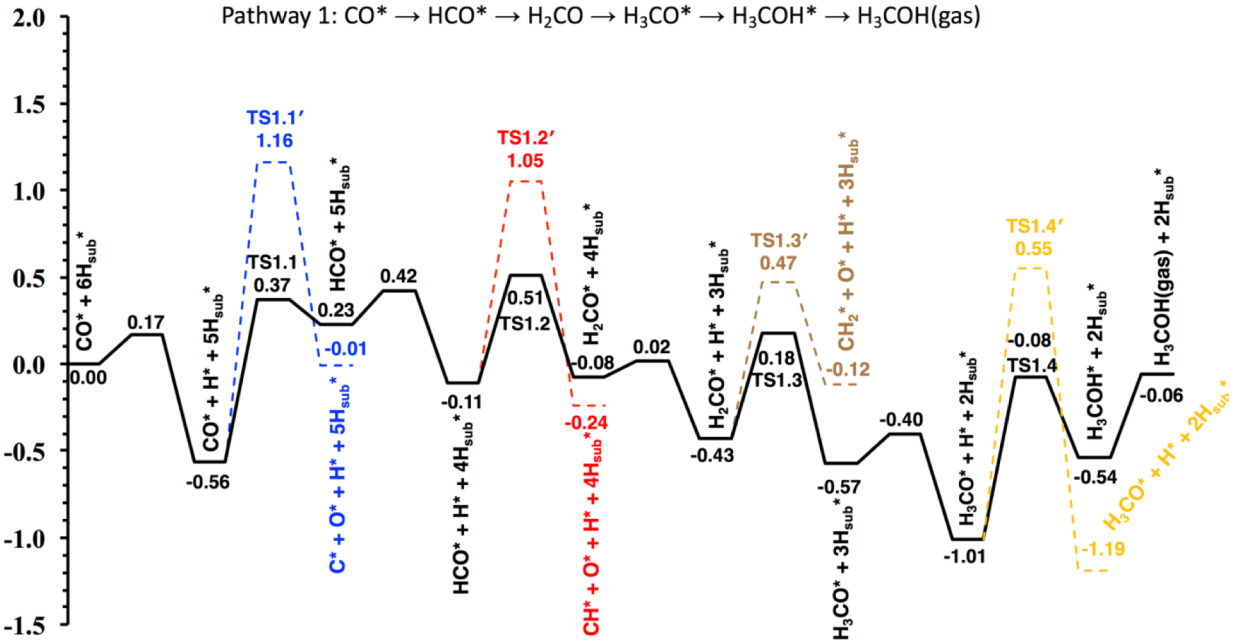

Figure 5.3. Energy diagram for Pathway 1 when subsurface hydrogen is initially present as a full (6-atom) monolayer and emerges to the surface before becoming a reactant.

5.3.2.1 Pathway 1

The relative energetics of the surface and subsurface cases for Pathway 1 are shown in Figures 5.2 and 5.3. We first note that, in both the surface and subsurface cases, at each step, the barrier to hydrogenation is always lower than the barrier to C-O bond breaking, which indicates that Pathway 1 favors methanol formation. We also see that formaldehyde, H_2CO, is a possible intermediate along this pathway. The binding energy of formaldehyde to the Ni(110) surface (-1.25 eV), given in Table 5.2, is lower than the binding energies of all other intermediates listed there, but it is higher than the barrier to either C-hydrogenation to give H_3CO (0.65 eV) or C-O dissociation (0.91 eV). This suggests that while some formaldehyde may desorb, formaldehyde should not be expected to be a significant product of Pathway 1.

The first possible step in Pathway 1 could either be C-hydrogenation of CO to give HCO (Figure 5.4a) or C-O bond breaking of CO (Figure 5.5a) to give C + O. Hydrogenation of CO to HCO through TS1.1 has a barrier of 1.08 eV without H_{sub} and 0.93 eV with H_{sub}. In this step, CO begins in a short-bridge site, while H is in a pseudo-threefold site. As H approaches CO, CO shifts away from H into a pseudo-threefold site, with O tilted further away from H. Interestingly, H moves to the side as it approaches CO, binding at an angle and then sliding back to form a straight line H-C-O from the top-down perspective. The reverse of this reaction step is thermodynamically favorable and has a very low barrier (0.14 and 0.28 eV with and without H_{sub}, respectively). C-O bond breaking of CO through TS1.1′ has a barrier of 1.72 eV both with and without H_{sub}, although the total energy of the step is 0.87 eV without H_{sub} but only 0.55 eV with H_{sub}, presumably due to

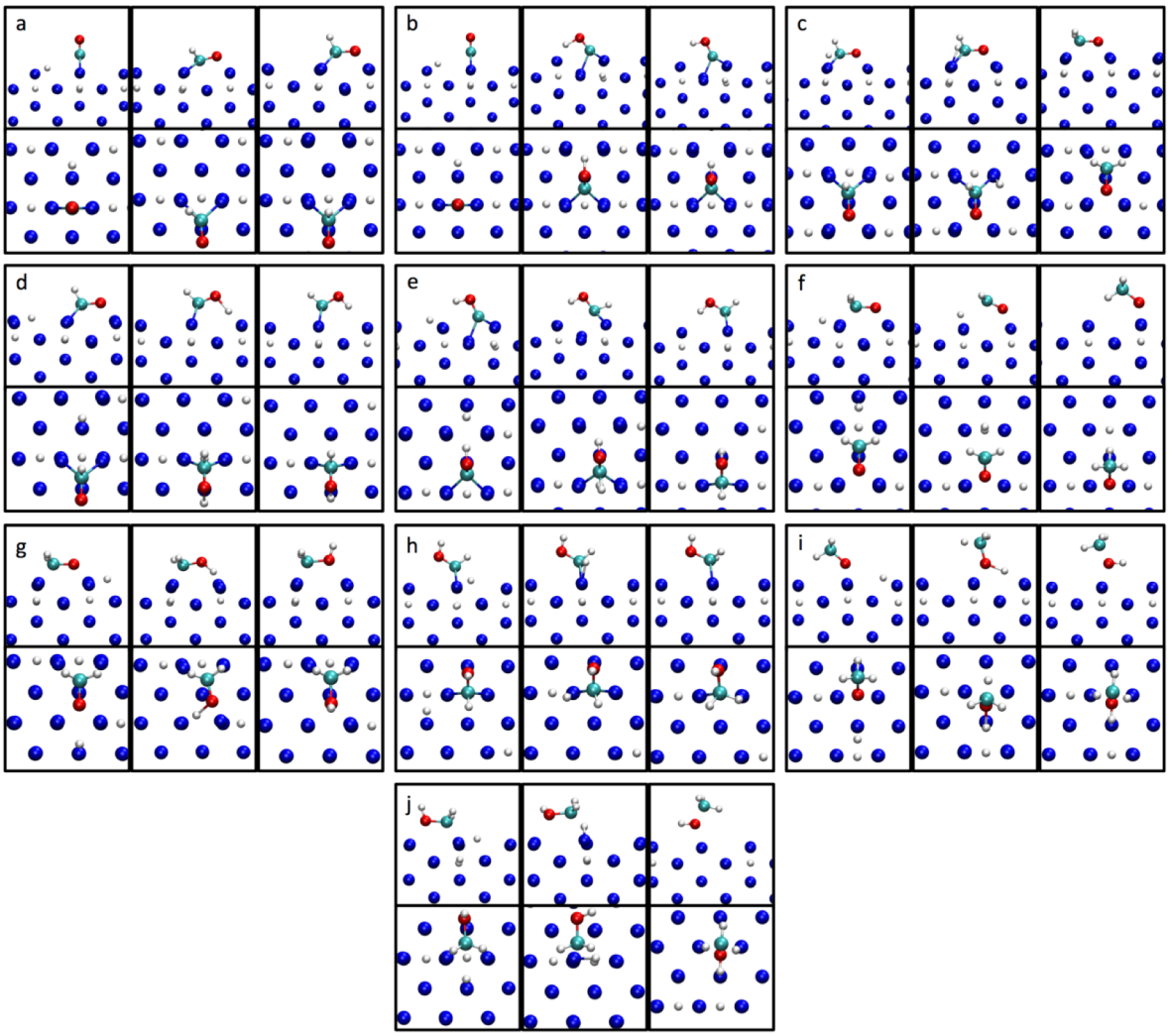

Figure 5.4. Initial, transition, and final states for each of the hydrogenation steps possible for CO and its intermediates along the pathway to H_3COH, specifically, hydrogenation of (a) CO to HCO, (b) CO to COH, (c) HCO to H_2CO, (d) HCO to HCOH (trans), (e) COH to HCOH (trans), (f) H_2CO to H_3CO, (g) H_2CO to H_2COH (cis), (h) HCOH (cis) to H_2COH (cis), (i) H_3CO to H_3COH, and (j) H_2COH (cis) to H_3COH. Only reactions in the presence of H_{sub} are shown, as there are no substantive visual differences between the surface and subsurface cases.

H_{sub} stabilizing C + O to a greater extent than it stabilizes CO. In this reaction process, CO shifts from its short-bridge site into a nearby hollow site, and then the C-O bond breaks as shown in Figure 5.5a, with C remaining in the hollow site and O moving to a long-bridge site. While the C-

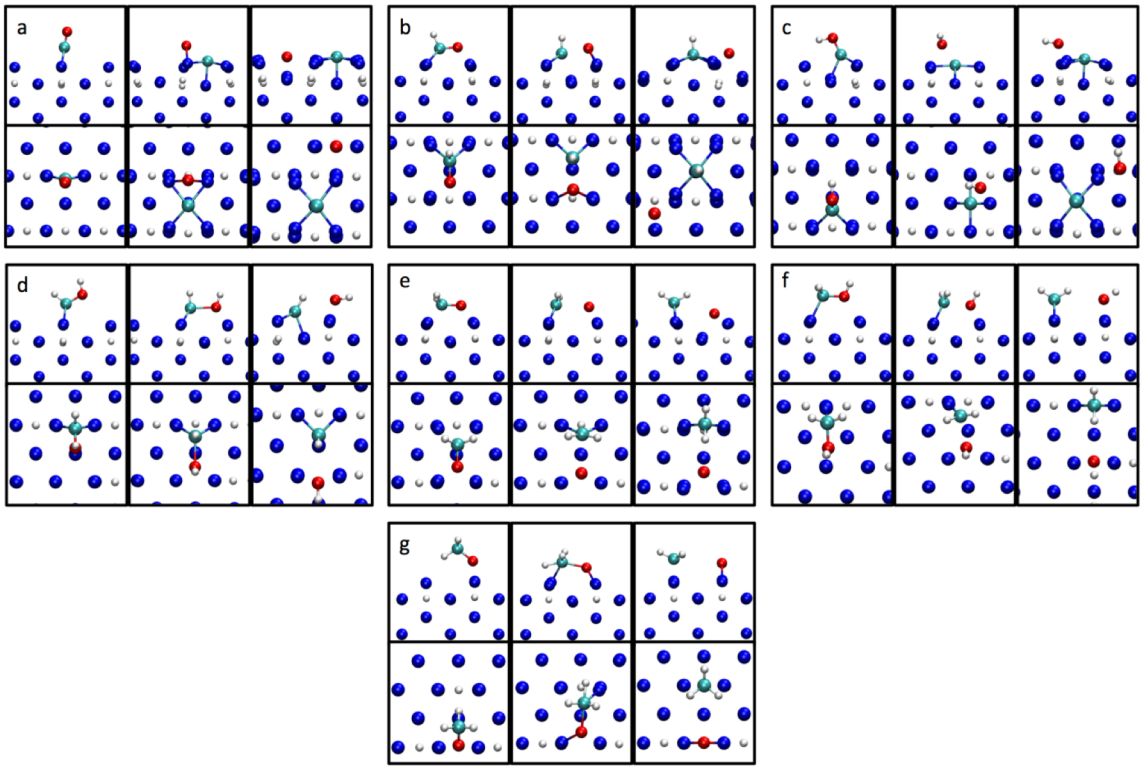

Figure 5.5. Initial, transition, and final states for C-O bond breaking reactions for each of the intermediates along Pathways 1, 2, 3, and 4. Specifically: (a) CO to C + O, (b) HCO to CH + O, (c) COH to C + OH, (d) HCOH (cis) to CH + OH, (e) H_2CO to CH_2 + O, (f) H_2COH (cis) to CH_2 + OH, and (g) H_3CO to CH_3 + O. Only reactions in the presence of H_{sub} are shown.

O cleavage process is not competitive with or without H_{sub}, the reverse barrier is significantly higher in the presence of H_{sub}. We see here that in Pathway 1 (as will be the case as well in Pathways 2 and 3) C-hydrogenation of CO is favored over C-O bond breaking.

The next possible steps in Pathway 1 are C-hydrogenation of HCO to H_2CO through TS1.2 (Figure 5.4c) and C-O cleavage of HCO to give CH + O through TS1.2′ (Figure 5.5b). C-hydrogenation of HCO has a barrier of 0.53 eV without H_{sub} and 0.62 eV with H_{sub}. In this step, H approaches HCO from an adjacent pseudo-threefold site, moving sideways from the top-down perspective. The other possibility, C-O cleavage to give CH + O, has a barrier of 0.94 eV without H_{sub} and 1.16 eV with H_{sub}. HCO begins bound through both C and O in pseudo-threefold sites, as

seen in the initial state shown in Figure 5.5b. Then, the C-O bond breaks as O shifts into a short-bridge site, followed by O shifting further away from CH as well as CH sliding into a hollow site. Again, both with and without H_{sub}, further hydrogenation along Pathway 1 is favored over C-O cleavage.

After this, H_2CO can undergo either C-hydrogenation to H_3CO through TS1.3 (Figure 5.4f) or C-O cleavage through TS1.3′ to CH_2 + O (Figure 5.5e). The C-hydrogenation of H_2CO has a 0.65 eV barrier without H_{sub} and a 0.61 eV barrier with H_{sub}. H_2CO begins "flat" on the Ni(110) surface, bound through both O and C in pseudo-threefold sites, as H approaches from another pseudo-threefold site. As H approaches, O shifts towards a short-bridge site and C moves up away from the surface as H binds to it. The C-O bond breaking of H_2CO through TS1.3′ has a barrier of 0.89 eV without H_{sub} and 0.90 eV with H_{sub}. This bond-breaking reaction is relatively simple (Figure 5.5e) – H_2CO begins bound to Ni(110) through C and O, with both in pseudo-threefold sites. Then, CH_2 pulls away into the nearby short-bridge site and twists such that C is bound tetrahedrally to two Ni atoms and two H atoms, while O remains in its pseudo-threefold site. Yet again, hydrogenation in this step is favored over C-O dissociation.

Finally, H_3CO can undergo O-hydrogenation to H_3COH through TS1.4 (Figure 5.4i) or C-O bond breaking through TS1.4′ to give CH_3 + O (Figure 5.5g). O-hydrogenation of H_3CO has a 1.04 eV barrier without H_{sub} and a 0.93 eV barrier with H_{sub}. In this step, H_3CO begins bound through O in a short-bridge site, with H in a pseudo-threefold site. As H approaches, O shifts into a pseudo-threefold site to meet H. Once H binds to O, O shifts slightly back towards the short-bridge site, but remains somewhere between the two. The C-O bond breaking of H_3CO has a barrier of 1.91 without H_{sub} and 1.56 eV with H_{sub}. In this C-O cleavage process, H_3CO begins bound through O to a short-bridge site. The molecule bends down to bring CH_3 closer to the surface while

O shifts over into a pseudo-threefold site. In the transition state, the H atom furthest from O stretches away from C such that it is loosely bound to the surface itself as well as to C, and then finally CH_3 ends up bound to a short-bridge site while O remains in its original short-bridge site. As the relative energetics of these two possible reaction steps show, the H_3CO intermediate is very likely to further react to produce methanol rather than methane.

Pathway 1 favors methanol production over methane production, as well as production of some amount of formaldehyde depending on the reaction conditions.

5.3.2.2 Pathway 2

We next consider Pathway 2, the relative energetics of which are shown in Figures 5.6 and 5.7. Pathway 2 only diverges from Pathway 1 after H_2CO is produced, and thus methane formation up to that point is not favored over continued hydrogenation. In Pathway 2, H_2CO undergoes O-hydrogenation to give H_2COH through TS2.3 rather than C-hydrogenation as in Pathway 1. The O-hydrogenation of H_2CO (Figure 5.4g) has a barrier of 1.13 eV without H_{sub} and 1.10 eV with H_{sub}. In the O-hydrogenation, H_2CO lays flat as above, and H approaches O from a pseudo-threefold site. As H approaches here, the C-O bond rotates slightly, parallel to the surface, to allow H to initially bind to O such that the O-H bond is parallel to the surface. The O-H bond then rotates such that H is above O. This competes with C-O bond breaking of H_2CO, which, as described in the context of Pathway 1, has a barrier of 0.89 eV without H_{sub} and 0.90 eV with H_{sub}. Here we see that C-O bond breaking is actually favored over O-hydrogenation, and that C-hydrogenation, with barriers of 0.65 and 0.61 eV without and with H_{sub}, is favored over both of these. Thus it is more likely for H_2CO to either dissociate into CH_2 and O or to undergo C-hydrogenation to join Pathway 1 than it is for O-hydrogenation to occur to form H_2COH.

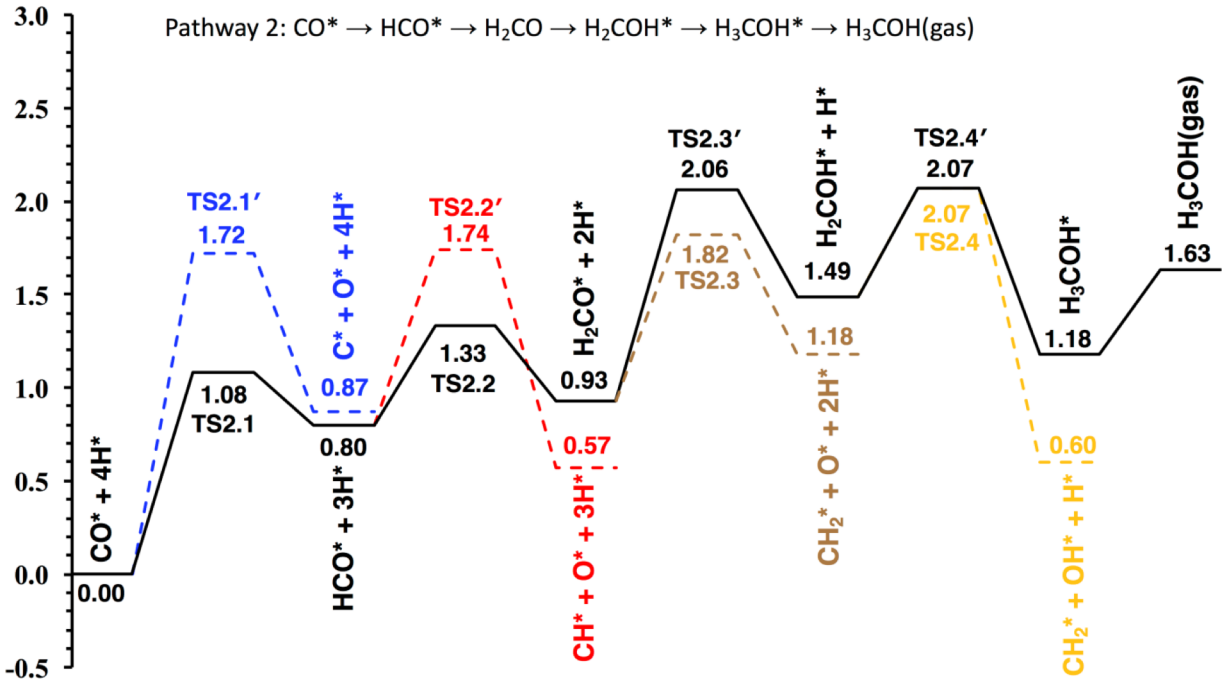

Figure 5.6. Energy diagram for Pathway 2 when subsurface hydrogen is not present.

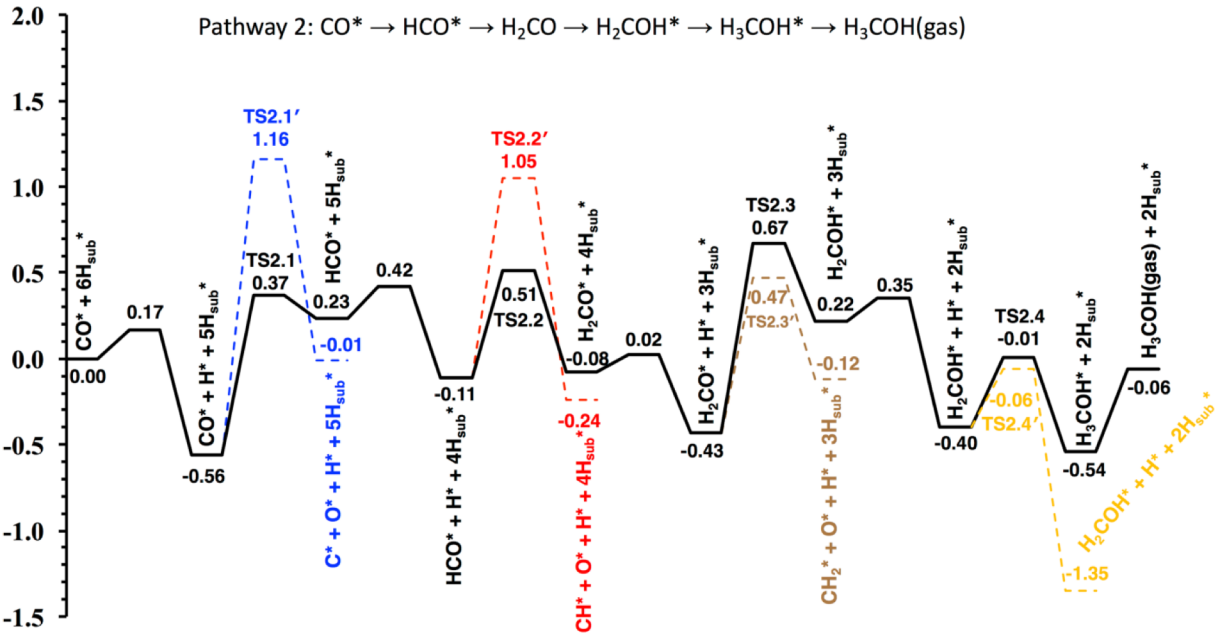

Figure 5.7. Energy diagram for Pathway 2 when subsurface hydrogen is initially present as a full (6-atom) monolayer and emerges to the surface before becoming a reactant.

If H_2COH does form, then there are two additional possibilities. First, H_2COH can undergo C-hydrogenation to give H_3COH through TS2.4 (Figure 5.4j), or the C-O bond can break to give CH_2 and OH through TS2.4′ (Figure 5.5f). C-hydrogenation to H_3COH has a barrier of 0.58 eV without H_{sub} and 0.41 eV with H_{sub}. H_2COH shifts such that C and O are both nearly in atop sites. Then as H approaches from a pseudo-threefold site, H_2COH begins to shift back somewhat, until H is loosely bound to both the Ni surface and C. Then H becomes strongly bound to C, and C lifts up from the Ni surface. Finally, O shifts back into the part-short-bridge/part-pseudo-threefold site described above. We find that C-hydrogenation to H_3COH and C-O bond breaking have identical barriers without H_{sub} (0.58 eV for both, as shown in Table 5.3), but with H_{sub}, C-O bond breaking is slightly favored (0.34 eV for C-O breaking against 0.41 eV for hydrogenation). In the C-O dissociation process, H_2COH shifts from its initial state in which C and O are both bound to pseudo-threefold sites to the first state shown in Figure 5.5f, in which both are closer to atop sites. The C-O bond then breaks as C and O each shift into short-bridge sites. Without H_{sub} these two reaction steps have identical barriers, although C-O bond breaking to CH_2 + OH has a much higher reverse reaction barrier. When H_{sub} is present, C-O dissociation has not only a higher reverse barrier than C-hydrogenation but also a lower forward barrier. As such, H_2COH is in either case more likely to yield methane than methanol, although the difference is not particularly large.

Overall, at H_2CO, where Pathways 1 and 2 diverge, C-hydrogenation to follow Pathway 1 is more favorable to O-hydrogenation to follow Pathway 2. Ignoring the possibility of shifting onto other pathways, Pathway 2 favors methane formation from C-O dissociation in both H_2CO and H_2COH, where dissociation is favored over hydrogenation.

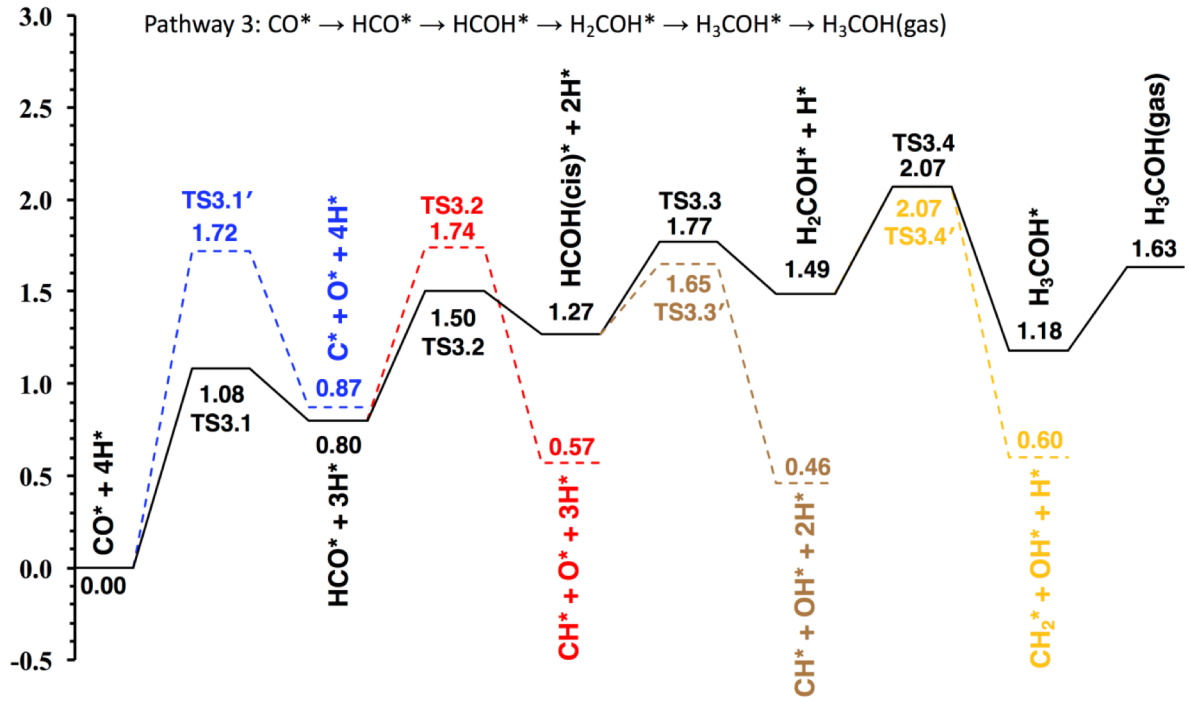

Figure 5.8. Energy diagram for Pathway 3 when subsurface hydrogen is not present.

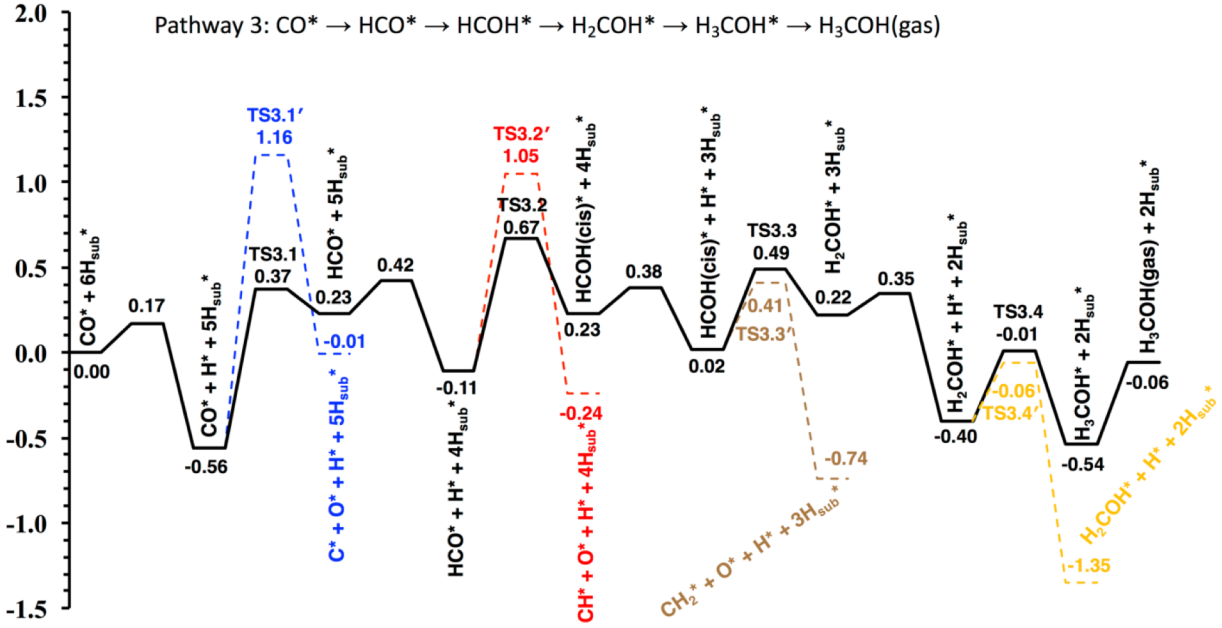

Figure 5.9. Energy diagram for Pathway 3 when subsurface hydrogen is initially present as a full (6-atom) monolayer and emerges to the surface before becoming a reactant.

5.3.2.3 Pathway 3

The relative energetics of Pathway 3 are shown in Figures 5.8 and 5.9. Pathway 3 diverges from Pathways 1 and 2 at HCO, where the adsorbate undergoes O-hydrogenation rather than C-hydrogenation. However, it rejoins Pathway 2 after HCOH undergoes C-hydrogenation to give H_2COH. As with Pathway 2, we will only discuss in detail here the few reaction steps that are unique to Pathway 3.

The O-hydrogenation of HCO through TS3.2 to give HCOH (Figure 5.4d) has a barrier of 0.70 eV without H_{sub} and 0.78 eV with H_{sub}, and involves the movement of H into a pseudo-threefold site beneath O, followed by HCO bending downwards to allow O to bind to H. O-hydrogenation has a lower barrier than does C-O bond breaking (0.94 eV without H_{sub}, 1.16 eV with H_{sub}), but a slightly higher barrier than C-hydrogenation (0.53 eV without H_{sub}, 0.62 eV with H_{sub}). The most energetically favorable step available to HCO is C-hydrogenation to continue with Pathways 1 and 2, where for each subsequent step hydrogenation to move along Pathway 1 towards methanol formation is energetically preferred.

It should be noted that HCOH is initially formed in its *trans* configuration, as shown in Figure 5.4d. However, we have found that barriers to both C-hydrogenation and C-O dissociation are substantially lower for the *cis* configuration of HCOH than they are for *trans*, and flipping HCOH from *trans* to *cis* also has a lower barrier than any further reaction for the *trans* configuration. Thus, in a subsequent step not shown above, HCOH flips from *trans* to *cis*. The barrier for this process is 0.55 eV without H_{sub} (ΔE = 0.25 eV) and 0.60 eV with H_{sub} (ΔE = 0.27 eV).

The *cis* conformer of HCOH can then undergo either C-hydrogenation through TS3.3 (Figure 5.4h) to give H_2COH or C-O dissociation through TS3.3′ (Figure 5.5d) to give CH + OH.

The barrier for C-hydrogenation is 0.50 eV without H_{sub} and 0.47 eV with H_{sub}. Here, HCOH begins in the *cis* configuration, with H at an adjacent pseudo-threefold site. H approaches C by moving towards the near Ni atom to which C is bound. In TS3.3 H is weakly bound simultaneously to both Ni and C, and then shifts to be bound more closely to C. Unlike the hydrogenation of HCO to HCOH, which first forms a stable trans conformer, hydrogenation of HCOH to H_2COH has no trans intermediate. The barrier for C-O bond breaking of HCOH (*cis*) is 0.38 eV without H_{sub} and 0.39 eV with H_{sub}. In this process, HCOH begins bound only through C in a short-bridge site. The molecule shifts such that C is in a pseudo-threefold site and O is also bound through a pseudo-threefold site, as shown in Figure 5.5d. Finally, the C-O bond breaks and CH ends up in a hollow site, while OH rests in a pseudo-threefold site. Both with and without H_{sub}, the barrier for C-O bond breaking is lower than that for C-hydrogenation, suggesting that methane is a more likely product than methanol should HCOH form. If HCOH does undergo C-hydrogenation, then the rest of Pathway 3 is identical to the corresponding portion of Pathway 2.

Again, it is more energetically favorable to remain on Pathway 1 than it is to diverge by having HCO undergo O-hydrogenation rather than C-hydrogenation. If only considered in isolation, Pathway 3 is more likely to give methane than methanol as a result of C-O dissociation in HCOH (*cis*) and H_2COH, but as with Pathway 2, the differences in energetics between steps leading to methane and those leading to methanol are not particularly large.

5.3.2.4 Pathway 4

Finally, we consider Pathway 4, the relative energetics of which are shown in Figures 5.10 and 5.11. Pathway 4 diverges from Pathways 1, 2, and 3 immediately, with CO undergoing O-hydrogenation rather than C-hydrogenation and giving COH rather than HCO. However, after

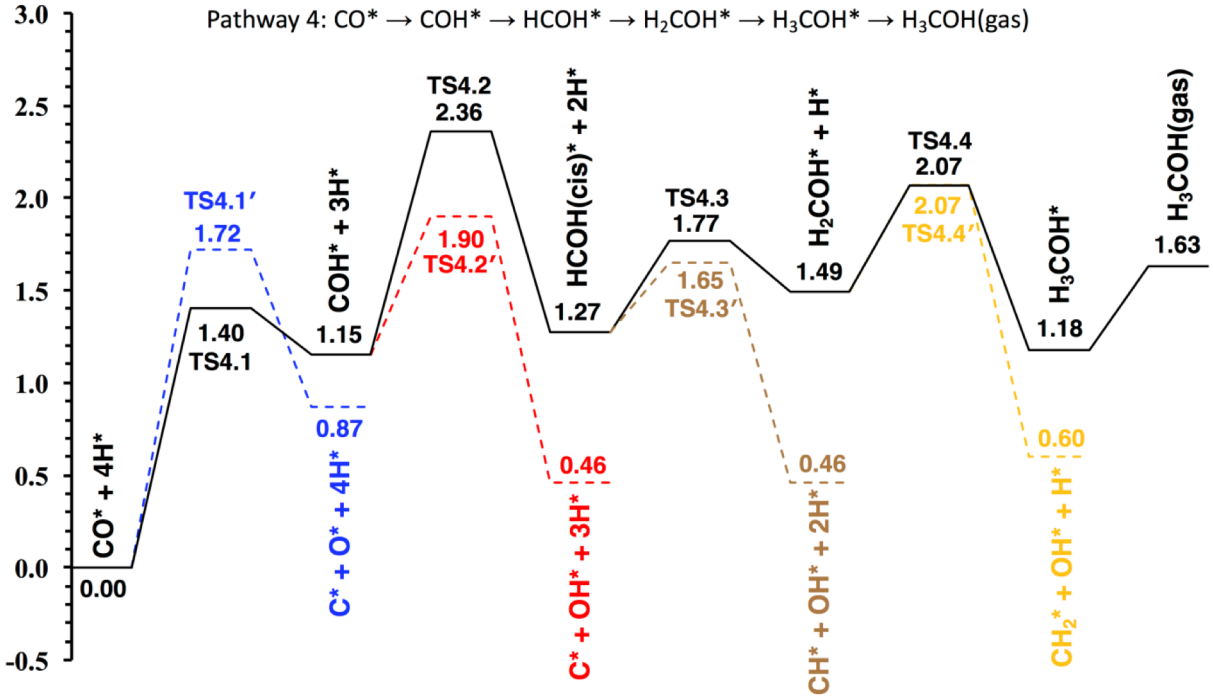

Figure 5.10. Energy diagram for Pathway 4 when subsurface hydrogen is not present.

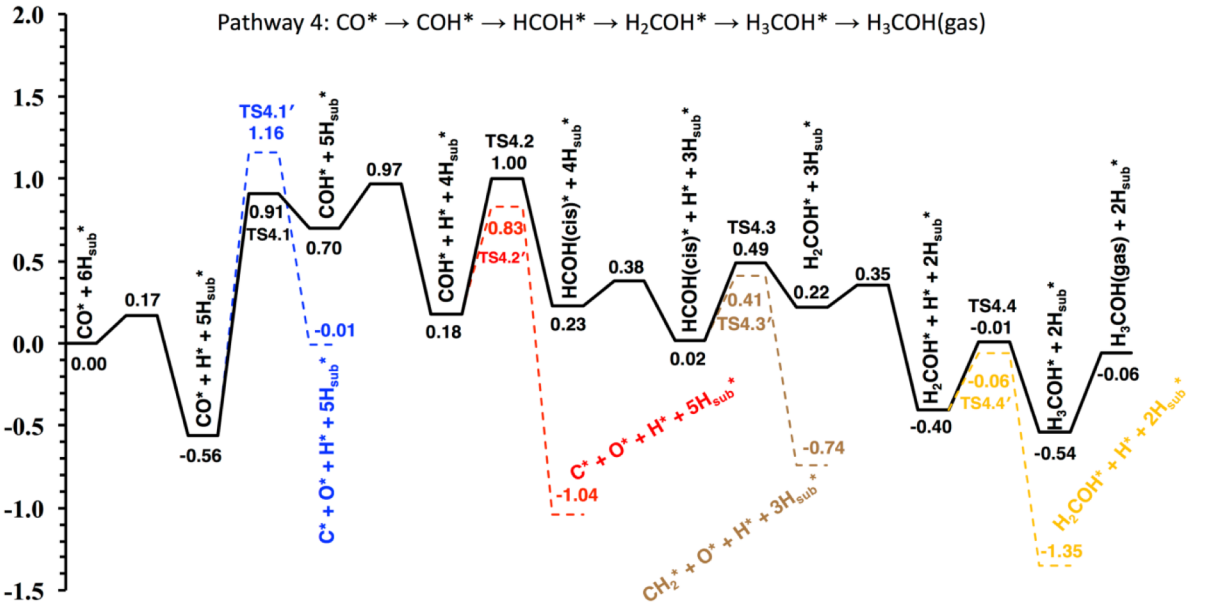

Figure 5.11. Energy diagram for Pathway 3 when subsurface hydrogen is initially present as a full (6-atom) monolayer and emerges to the surface before becoming a reactant.

COH undergoes O-hydrogenation to give HCOH, the remainder of Pathway 4 is identical to Pathway 3.

Initially, CO can either undergo O-hydrogenation through TS4.1 to COH (Figure 5.4b) or C-O dissociation through TS4.1′ to C + O (Figure 5.5a), the latter of which has already been described in our discussion of Pathway 1 (this same transition state was referred to then as TS1.1′). The barrier for O-hydrogenation of CO is 1.40 eV without H_{sub} and 1.47 eV with H_{sub}. In this step, CO begins in a short-bridge site and shifts towards H into a pseudo-threefold site as the C-O bond tilts downwards to allow O to bind to H in TS4.1, and then returns to a mostly upright position, still in the pseudo-threefold site. As with the hydrogenation of CO to HCO, the reverse of this reaction is thermodynamically favorable and must overcome only a small barrier (0.25 eV). Here, the reaction barrier is raised by the presence of H_{sub}. If we compare O-hydrogenation to the two other possible steps, C-hydrogenation and C-O dissociation, we find that while O-hydrogenation is certainly favorable relative to C-O dissociation, C-hydrogenation is still favored over both alternatives. Thus, as with Pathways 2 and 3, it is favorable to remain in Pathway 1 than to diverge into Pathway 4.

COH can undergo C-hydrogenation to give HCOH (formed as *trans* but then flipping to *cis*) through TS4.2 (Figure 5.4e) or C-O bond breaking to give C + OH through TS4.2′ (Figure 5.5c). C-hydrogenation of COH has a barrier of 1.21 eV without H_{sub} and 0.82 eV with H_{sub}, a remarkable difference and indeed the largest observed in this study. In this case, H_{sub} appears to alter the favored position of COH in TS4.2. Without H_{sub}, C is somewhere between a short-bridge and pseudo-threefold site in TS4.2, while with H_{sub} C is further towards pseudo-threefold, perhaps allowing H to approach while introducing less strain to the system. C-O dissociation of COH has a barrier of 0.75 eV without H_{sub} and 0.65 eV with H_{sub}. This process involves COH shifting from

its pseudo-threefold site to a long-bridge site, and then the C-O bond breaking to leave C in a hollow site and OH in a short-bridge site (Figure 5.5c). C-O dissociation is more favorable than C-hydrogenation of COH without H_{sub}. As the barrier to C-hydrogenation is lowered much more substantially than that for C-O dissociation when H_{sub} is present, continuing on toward HCOH and rejoining Pathway 3 is far more likely in the presence of H_{sub}. Still, even with H_{sub}, C-O dissociation remains favorable.

The first step along Pathway 4, the O-hydrogenation of CO, is particularly unfavorable, and thus Pathway 4 is not preferred – again, as seen in each pathway examined, Pathway 1 is at every turn the most favorable. In isolation, Pathway 4 is more likely to result in methane than in methanol, particularly without H_{sub} present to lower the barrier of C-hydrogenation of COH.

Table 5.3. Activation and reaction energies for each reaction step, both with and without subsurface hydrogen.

Reaction	$E_{act,\ no\ sub}$ (eV)	$E_{react,\ no\ sub}$ (eV)	$E_{act,\ sub}$ (eV)	$E_{react,\ sub}$ (eV)
CO* → C* + O*	1.72	0.87	1.72	0.55
CO* + H* → HCO*	1.08	0.80	0.93	0.79
CO* + H* → COH*	1.40	1.15	1.47	1.26
HCO* → CH* + O*	0.94	-0.23	1.16	-0.13
HCO* + H* → H_2CO*	0.53	0.13	0.62	0.09
HCO* + H* → HCOH* (trans)	0.70	0.22	0.78	0.34
COH* → C* + OH*	0.75	-0.69	0.65	-1.22

COH* + H* → HCOH* (trans)	1.21	0.02	0.82	0.05
HCOH* (cis) → CH* + OH*	0.38	-0.81	0.39	-0.76
HCOH* (cis) + H* → H_2COH* (cis)	0.50	0.22	0.51	0.20
H_2CO* → CH_2* + O*	0.89	0.25	0.90	0.31
H_2CO* + H* → H_3CO*	0.65	-0.13	0.61	-0.14
H_2CO* + H* → H_2COH* (cis)	1.13	0.51	1.10	0.65
H_2COH* (cis) → CH_2* + OH*	0.58	-0.89	0.34	-0.95
H_2COH* (cis) + H* → H_3COH*	0.58	-0.31	0.41	-0.14
H_3CO* → CH_3* + O*	1.91	-0.16	1.56	-0.18
H_3CO* + H* → H_3COH*	1.04	0.49	0.93	0.48

Ultimately, both with and without subsurface hydrogen, our results suggest that hydrogenation of CO on a Ni(110) surface is more likely to yield methanol than methane, as Pathway 1 towards methanol is at each step the most favorable pathway. However, if they are accessed, Pathways 2, 3, and 4 are each at least slightly more likely to yield methane than they are methanol. Of Pathways 2, 3, and 4, the most energetically favorable is Pathway 3. It diverges from Pathways 1 and 2 at HCO, where HCOH is produced rather than H_2CO. The difference in barriers between these two possibilities is less than 0.2 eV both with and without H_{sub}. For each subsequent step, Pathway 3 actually has lower barriers than does Pathway 1. Therefore, Pathway 3 should be

somewhat competitive with Pathway 1. In general, the effect of subsurface hydrogen on the question of methane vs. methanol production is muddled, as in some cases subsurface hydrogen promotes C-O dissociation and thus methane formation and in others it suppresses C-O dissociation.

In comparison with similarly-calculated results for other catalyst surfaces for CO hydrogenation, we find that Ni(110), with or without H_{sub}, occupies a middle ground between Cu and Co in terms of the favored product. On Co(111), the total reaction barrier for methanol formation is 2.59 eV, compared with 0.51 eV on Cu(111), 2.83 eV on Ni(111), 0.43 eV on Cu(211), and 1.85 eV on Ni(110) as reported in the present work (without H_{sub}). In contrast, the lowest total reaction barrier for CO dissociation on Co(111) is 1.83 eV, compared with 2.31 eV on Cu(111), 2.29 eV on Ni(111), and 1.72 eV in the present work (again, without H_{sub}).[128,150]

We also find that our results are consistent with those of the recent experimental study by Roiaz et al.,[134] if not with its conclusions. Employing infrared-visible sum frequency generation (IR-vis SFG) spectroscopy as well as X-ray photoelectron spectroscopy (XPS), Roiaz et al. investigated the surface-adsorbed species during the CO hydrogenation reaction and reported the presence of a measurable amount of carbon, suggesting C-O dissociation and therefore CO methanation. However, our results suggest that, while C-O dissociation is certainly a possibility, methanol production should be more favorable, and the most notable intermediates of the methanol production pathway have far lower binding energies to Ni(110) than do C atoms. Thus, we suggest that methanol may in fact be a significant product of this reaction, but may not be measured by the techniques employed by the authors, who observed intermediates bound to the surface rather than the products that desorbed from the surface.

5.4. Conclusions

We studied the relative energetics of several reaction pathways for the hydrogenation of CO on a Ni(110) surface to yield methanol, with and without subsurface hydrogen. For the various intermediates along those pathways we also investigated the relative energetics of C-O bond breaking, which would lead to methane rather than methanol production. We found that while subsurface hydrogen uniformly increased binding energies of the adsorbates, the degree to which they were increased was inconsistent, leading to a mixed effect on reaction barriers and reaction energies. However, we did find several reaction steps for which the difference in barrier height between the surface and subsurface cases was nearly as high as 0.4 eV, which suggests that it cannot be safely assumed that the impact of subsurface hydrogen will be small.

The most favorable pathway, with and without subsurface hydrogen, was found to be Pathway 1, in which CO undergoes sequential hydrogenation of C to give H_3CO (passing through a formaldehyde intermediate), followed by hydrogenation of O to give methanol. The other pathways that were studied all appeared likely to give either a roughly even mix of methane and methanol or slightly more methane than methanol. We also found that some small amount of formaldehyde would probably be formed from desorption of the H_2CO intermediate, but that both methane and methanol formation from H_2CO were more energetically favorable than desorption. Our study provides useful insight into the various mechanisms by which methane and methanol can be produced from CO and H_2 on a Ni(110) surface.

CHAPTER 6

Surface Passivation and Doping of Black Phosphorus with Lewis Acids

6.1 Introduction

Black phosphorus (BP) is an allotrope of phosphorus, and is analogous in many ways to graphite. Like graphite, BP is a layered material in which individual layers are only weakly bound to one another through van der Waals forces.[151] Also like graphite, the single- and few-layer forms of BP (often called phosphorene in analogy to graphene), as well as forms thick enough to be considered thin films, are of great interest as 2D semiconductors. Unlike graphene, however, individual layers of BP are not planar. Rather, they have a puckered geometry as shown in Figure 6.1. BP is a promising 2D semiconductor material that represents a compromise between the high carrier mobility but low on/off current ratio of graphene and the high on/off ratio but lower carrier mobility of transition metal dichalcogenides.[152]

BP was first synthesized in 1914 by Percy Williams Bridgman by conversion of white phosphorus at high pressure and temperature.[153] Bulk BP, however, was not particularly interesting, and from its discovery in 1914 to the beginning of 2014 the authors of one review paper estimate there were only about 100 publications written about BP.[152] Those same authors estimate that, after the first few papers were published proposing BP as a 2D semiconductor material in early 2014,[154,155] there were more than 100 new publications on the subject within the following year.[152] BP is of particular interest due to its layer-dependent band gap, which can vary

between 0.3 and 2.0 eV based on the thickness of the material,[156,157] as well as its anisotropic thermal and electrodynamic properties.[158]

As with many semiconductor materials, one of the largest impediments to the use of BP as a 2D semiconductor in everyday devices is that it degrades easily when exposed to air. It has been shown that this degradation is due to the formation of PO_x compounds at the air-semiconductor interface when the BP surface is exposed to both O_2 and H_2O from the atmosphere.[159] There have been a number of methods proposed and developed for passivating the exposed BP surface and thereby protecting it from degradation. One such proposed method is atomic layer deposition of AlO_x overlayers on the BP surface, which has been shown to preserve device performance in BP-based field effect transistors even when exposed to ambient conditions.[159]

Functionalization of BP presents an opportunity to simultaneously passivate the BP surface to protect device performance and dope BP to increase that performance. In 2016, Ryder et al.[13] demonstrated that the BP surface could be functionalized with anisole and nitrobenzene via aryl diazonium chemistry. The authors found that not only did this protect the BP against degradation from ambient exposure, but it also resulted in p-type doping of the BP surface and a corresponding increase in performance in BP-based field-effect transistors.

It may be possible to achieve this simultaneous passivation and doping through binding with Lewis acids. Each phosphorus atom in BP is sp^3 hybridized and has five valence electrons, with three electrons involved in bonding to its neighbors and the other two in a lone pair. Just as phosphorus atoms are Lewis bases, so too should a BP surface act as a Lewis base, with a lone pair hanging off of each P atom. Binding Lewis acids to the BP surface may present another means of passivating the surface, and with the right Lewis acid it may be possible to achieve a greater

degree of p-type doping, and therefore a greater increase in performance, than that found when phenyl species are bound.

Borane is an interesting candidate as an adsorbate to both passivate and dope BP surfaces. Adducts of borane and phosphine, a Lewis acid and Lewis base, respectively, have long been of interest in the study of coordination complexes, and borane and related species are often used as protecting groups during the synthesis of phosphines.[160] As mentioned in the previous paragraph, phosphorus atoms that are sp^3 hybridized have a lone pair. The boron atom in borane and related species is two electrons short of a complete octet of valence electrons. Thus, the two form what is called a dative bond, in which both electrons involved in bonding are donated by the same atom, in this case phosphorus. Borane is not the only Lewis acid capable of forming a dative bond with phosphorus, as we will show, but it is by far the best-known.

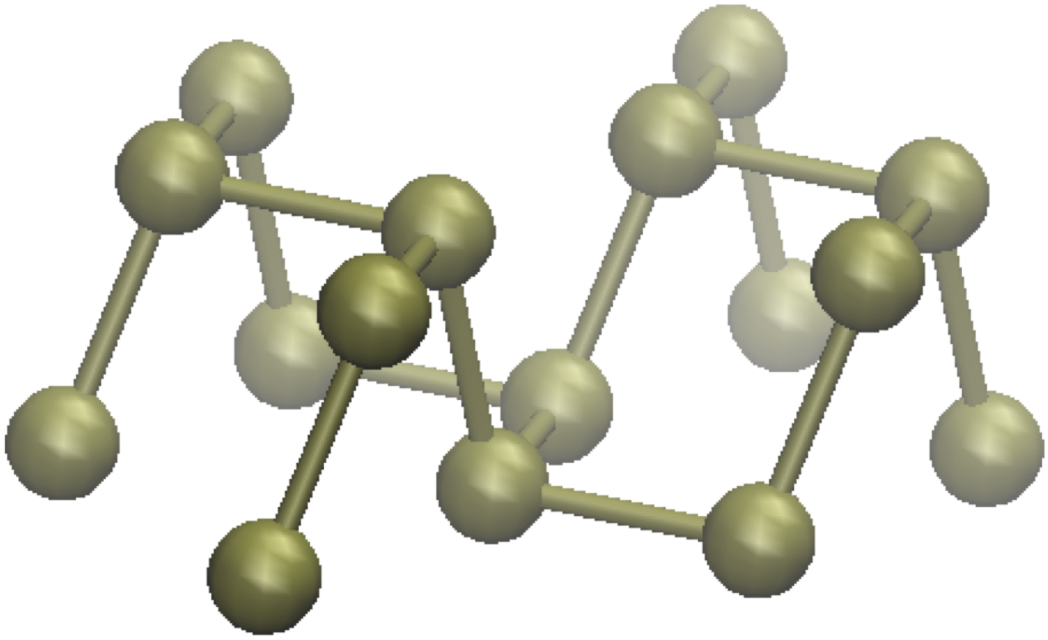

Figure 6.1. The P_{16} unit cell used to represent the phosphorene monolayer.

The strength of a bond between a Lewis acid and Lewis base, as well as the simple matter of whether or not a bond will form at all, is often explained using a model called HSAB theory, which means "hard and soft acids and bases." The fundamental concept of HSAB theory is that Lewis acids and bases can be either hard or soft. Hard acids and bases tend to be smaller and be more weakly polarizable, while soft acids and bases are larger and more strongly polarizable. In HSAB theory, it is predicted that hard Lewis acids bind more readily to hard Lewis bases, and soft Lewis acids bind more readily to soft Lewis bases. While HSAB theory was originally developed as a purely qualitative model that was capable of explaining and predicting trends in binding,[161] the concept of chemical hardness has since been quantified.[162,163]

In this chapter, we present a theoretical study of the surface doping of BP with a variety of Lewis acids. Specifically, we focus on borane and related species and methylene and related species bound to a phosphorene monolayer and to a phosphine molecule. We calculate the bond lengths, binding energies, and net charge transfer for each Lewis acid we study. For select Lewis acids we also examine how binding energies and net charge transfers change with increasing adsorbate converage on the phosphorene monolayer. We find that, like phosphine, the phosphorene monolayer acts as a soft Lewis base. As predicted by HSAB theory, phosphorene binds more strongly with soft Lewis acids like BH_3 and CH_2 than with hard Lewis acids such as BF_3 and BCl_3, with which the phosphorene monolayer does not bind at all. Of borane and its related species, borane and $B(SiH_3)_3$ were found to bind the most strongly to the phosphorene monolayer, but both were found to result in only negligible charge transfer and thus negligible doping. Of methylene and its related species, methylene and $C(CF_3)_2$ were found to bind most strongly, with both resulting in very significant electron transfer from the phosphorene monolayer into the adsorbate.

Finally, we demonstrate that between methylene and $C(CF_3)_2$, $C(CF_3)_2$ is the better candidate, as it distorts the BP surface less and raises rather than lowers BP's band gap.

6.2 Computational Methods

All calculations in this chapter were performed using plane-wave density functional theory (DFT) with periodic boundary conditions as implemented in version 5.3.5 of the VASP software package.[142,143] The PBE exchange-correlation functional was used,[144] while projector-augmented wave (PAW) potentials[145,146] were used to model electron-ion interactions. The DFT-D3 dispersion correction method of Grimme et al.[164] was used to model van der Waals interactions. Structural relaxation calculations were performed using the conjugate gradient method.

Charge analysis was performed using the Bader method[165] as implemented in VASP by the Henkelman group.[166–168] The net charge transfer, Δe, for each system was calculated using the formula

$$\Delta e = q_{BP,\ pristine} - q_{BP,\ adsorbate} \tag{6.1}$$

where $q_{BP,pristine}$ is the sum of the electron charges on each atom in a pristine phosphorene monolayer slab and $q_{BP,adsorbate}$ is the same sum but in the presence of one or more adsorbates. A positive Δe value implies transfer of electron density from the monolayer into the adsorbate(s) and thus suggests p-type doping.

The phosphorene monolayer studied in this chapter was modeled by a slab consisting of 2 by 2 units of 4 P atoms each, resulting in a P_{16} slab as shown in Figure 6.1. The unit cell also contained about 27 Å of vacuum vertically between each phosphorene monolayer to prevent interactions between vertically-neighboring images. A 5x5x1 Monkhorst-Pack grid was used for **k**-sampling of the Brillouin zone.[149]

6.3 Results and Discussion

6.3.1 Borane and related species

We first discuss the binding of borane and related species to the phosphorene monolayer. As discussed above, borane and its related species are often found to bind to phosphine and its related species quite strongly, forming a dative bond in which the two electrons involved in binding both come from the same atom, in this case phosphorus.

We placed single molecules of borane and various substituted boranes on the phosphorene monolayer and performed a structural relaxation. Many of the species did not bind normally, and instead simply moved away from the surface until the system reached an acceptable minimum energy. In theory this would be in some position where the species in question was loosely bound to the surface at some longer distance by van der Waals forces, but in our calculations an energy minimum was typically found such that there was no binding at all. Some other species, however, did successfully bind. Data on each molecule that was tried as an adsorbate on the phosphorene monolayer is given in Table 6.1, including binding energy, P-B bond length, Δe, and the resulting band gap of the system. It should be noted that DFT is notoriously inaccurate when calculating band gaps. We provide calculated band gaps here only to show how the band gap changes when adsorbates are added, not to predict with any certainty the experimental band gap of such a system. We also give the same data for a phenyl radical bound to the surface. In the previous experimental study by Ryder et al.[13] demonstrated BP functionalization and passivation via aryl diazonium chemistry, it was found the binding of anisole and nitrobenzene to the BP surface resulted in notable p-type doping. We use the phenyl radical, which is essentially anisole or nitrobenzene without any substituents, as a simple point of reference against which we can compare borane and its related species. As a point of comparison for the phosphorene-bound species we also present

bond lengths, binding energies and net charge transfers for these same species bound to phosphine, given in Table 6.2.

Table 6.1. Binding energies, X-P bond lengths, Δe values, and band gaps for single adsorbates bound to the phosphorene monolayer. A "–" either indicates that the adsorbate in question did not bind to phosphorene or that there is no adsorbate.

	E_b (eV)	$R_{X–P}$ (Å)	Δe (e)	Band gap (eV)
Pristine	–	–	–	0.89
BH_3	-1.137	1.968	0.0885	1.08
BH_2F	-0.3329	2.220	0.1738	1.06
BHF_2	–	–	–	–
BF_3	–	–	–	–
BCl_3	–	–	–	–
$B(CH_3)_3$	–	–	–	–
$B(SiH_3)_3$	-1.510	1.916	-0.048	1.25
$B(CF_3)_3$	-0.6483	2.208	0.414	0.96
$B(C_6F_5)_3PH_3$	–	–	–	–
C_6H_5	-3.012	1.860	0.382	0.90

We first note that simple borane, BH_3, does not bind nearly as strongly to phosphorene as does the phenyl radical, with binding energies of -1.14 and -3.01 eV, respectively. In addition, the Δe for borane is substantially lower than that of the phenyl radical, at 0.09 e against 0.38 e. Finally, borane increases the band gap of phosphorene from 0.89 to 1.08 eV, while the phenyl radical increases the gap negligibly, from 0.89 to 0.90 eV. The binding properties of borane adducted with phosphine are found to be very similar to those of borane bound to phosphorene. Ultimately, we find that borane itself is a poor candidate.

Table 6.2. Binding energies, X-P bond lengths, Δe values, and band gaps for various borane-related species adducted with phosphine, PH_3.

	E_b (eV)	R_{X-P} (Å)	Δe (e)
BH_3PH_3	-1.404304	1.912	0.0870
BH_2FPH_3	-0.480035	2.046	0.1523
BHF_2PH_3	-0.074712	2.402	0.1673
BF_3PH_3	–	–	–
BCl_3PH_3	-0.3000	1.999	0.2279
$B(CH_3)_3PH_3$	-0.247314	2.003	0.08910
$B(SiH_3)_3PH_3$	-1.8412	1.874	0.0436
$B(CF_3)_3PH_3$	-1.885668	1.636	0.2632
$B(C_6F_5)_3PH_3$	-0.5445	1.968	0.2566

We next explore a series of substituted boranes, attempting to tune both binding energy and Δe. Borane is a soft Lewis acid and phosphine (and by extension phosphorene) is a soft Lewis base.[161] Borane can be substituted in a number of different ways to make it more electron-withdrawing, and thus result in a larger Δe, even if the resulting molecule may be less soft as a Lewis acid. The simplest substitution that can be made is the replacement of H with halides, in particular fluoride and chloride. Trifluoroborane, or BF_3, should be expected to be extremely electron-withdrawing, but it is also well-known as a hard Lewis acid. Unsurprisingly, we find that it does not bind to phosphorene. To strike a balance between softness and electron-withdrawing character, we also attempted to bind BHF_2 and BH_2F to phosphorene. Only BH_2F successfully bound, with a very low binding energy of -0.33 eV but nearly double the Δe of BH_3. The low binding energy of BH_2F makes it impractical. Trichloroborane, BCl_3, also failed to bind. We also

find that most of these same species bind slightly more strongly to phosphine than to phosphorene, and that BCl_3 and BHF_2, which fail to bind to phosphorene, do bind to phosphine, although both bonds are weak and, in the case of BHF_2, extremely weak. This difference in binding, in which phosphine performs better across the board than does phosphorene, is likely attributable to steric interactions between substituents on borane and the phosphorene monolayer, as well as the individual P atoms in phosphorene being weaker nucleophiles than the P atom in PH_3.

Next we model binding of trimethylborane, $B(CH_3)_3$ and trisilylborane, $B(SiH_3)_3$ to phosphorene. Trimethylborane is known as a borderline Lewis acid, in that it is somewhere between a hard and soft Lewis acid. We find that trimethylborane is unable to bind to phosphorene, likely due to a combination of hardness and steric interaction between the methyl groups and the phosphorene surface. Trisilylborane is not a commonly-used or -studied molecule by any means, but it was included in a theoretical study by Plumley and Evanseck[169] of Lewis acidity, where it was found to actually donate electrons to ammonia in B-N adducts. Surprisingly, we find that binds more strongly to phosphorene than does borane, but that, as suggested by the findings of Plumley

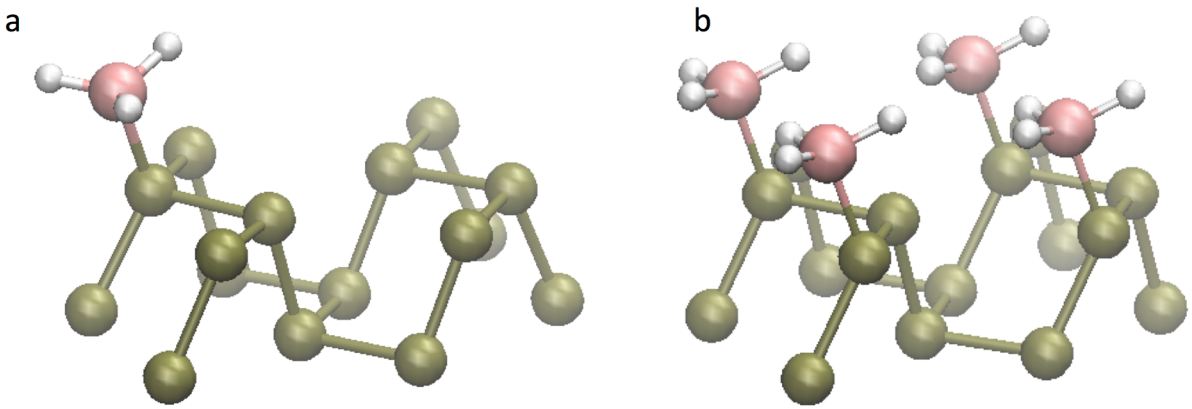

Figure 6.2. The phosphorene monolayer with (a) one and (b) four boranes bound per P_{16} unit cell.

and Evanseck, it results in an increase in electron density on phosphorene rather than a decrease, and thus n-type rather than p-type doping. Trimethylborane does bind to phosphine, although quite weakly, and we see that trisilylborane binds more strongly to phosphine than it does to phosphorene. Interestingly, while when bound to the phosphorene monolayer trisilylborane results in a negative Δe, it results in a positive Δe when bound to phosphine.

The final borane related species we examine bound to phosphorene are bis(trifluoromethyl)borane, $B(CF_3)_3$, and $B(C_6F_5)_3$, tris(pentafluorophenyl)borane. Bis(trifluoromethyl)borane is both a soft Lewis acid and highly electron-withdrawing. However, we find that its binding energy to phosphorene is lower than that of BH_3. In the case of phosphine binding, we find that $B(CF_3)_3$ in fact binds much more strongly, suggesting that it is steric hindrance due to the large size of the CF_3 substituents on $B(CF_3)_3$ that is responsible for the relatively weaker binding to the phosphorene surface. While the binding energy of $B(CF_3)_3$ to phosphorene, -0.65 eV, is weak, we do find a very substantial Δe value at 0.41 e, even higher than the 0.38 e of the phenyl radical. We also find that despite its much stronger binding energy when bound to phosphine, the $B(CF_3)_3PH_3$ adduct has a significantly smaller Δe value, 0.26 e, than does the same adduct with the phosphorene monolayer. This may be due to the limited availability of electron density in phosphine – in comparison, as electron density is withdrawn from a P atom in phosphorene, it can be partially replenished by donations from the surrounding P atoms. We also find that $B(C_6F_5)_3$ fails to bind to phosphorene, but does bind somewhat weakly to phosphine. Again, this difference is almost certainly due to steric interactions, as the three C_6F_5 substituents on this Lewis acid are very bulky.

Table 6.3. Comparison of binding and electron transfer properties of BH_3 at two different surface concentrations, along with the pristine phosphorene monolayer.

	E_b (eV) per adsorbate	Δe (e) per adsorbate	Δe (e)	Band gap (eV)
Pristine	–	–	–	0.89
One BH_3	-1.137	0.0885	0.0885	1.08
Four BH_3s	-0.6647	0.0267	0.1067	1.06

Lastly, we consider the effects of higher surface coverages of borane. Borane does not bind nearly as strongly to the phosphorene surface as does the phenyl radical, and it does not withdraw nearly as much electron density, but it does have the advantage of being smaller, potentially allowing a greater surface coverage. We compare a single borane molecule adsorbed to the surface with four borane molecules adsorbed in Table 6.3, with the coverages illustrated in Figure 6.2. Note that we do not consider the case of eight boranes bound to the monolayer, with four on each side. The purpose of this study is to gain insight into the behavior and effects of Lewis acid adsorbates on a BP surface. Thus, even though the system we model is a monolayer of phosphorene in which both sides are exposed, we only consider binding to one side. We do find that, overall, the Δe of the phosphorene layer bound to four borane molecules is higher than that of a single molecule. However, this effect is not particularly large, and we see that the Δe per adsorbed borane drops from 0.089 with one borane to 0.027 with four, and the binding energy per adsorbed borane drops from -1.14 to -0.66. We find that while borane may be able to achieve greater surface coverage than the phenyl radical, this provides little advantage and in fact makes individual borane atoms more likely do desorb.

6.3.2 Methylene and related species

Methylene, CH_2, and its substituted species are far less-commonly used as Lewis acids. However, methylene is a soft Lewis acid, and thus we explored it as an alternative to borane. We found that it worked extremely well for our purposes, and thus we went on to explore a number of its related species as well. Because methylene has two electrons not involved in bonding as well as two empty orbitals, methylene can exist in either singlet or triplet states.[170] In the singlet state the two electrons are spin-paired, while in the triplet state they are unpaired. In methylene itself, the triplet state is slightly more stable, but when methylene undergoes substitution the singlet state is typically stabilized and thus becomes the ground state. For ease of comparison, we consider

Table 6.4. Binding energies, X-P bond lengths, Δe values, and band gaps for single adsorbates related to methylene bound to the phosphorene monolayer. A "–" either indicates that the adsorbate in question did not bind to phosphorene or that there is no adsorbate.

Adsorbate	E_b (eV)	$R_{X–P}$ (Å)	Δe	Band gap (eV)
Pristine	–	–	–	0.89
CH_2	-3.535	1.677	0.8114	0.83
CF_2	-0.4848	1.907	0.4601	1.20
CCl_2	-1.310	1.787	0.6645	1.03
CBr_2	-1.384	1.795	0.5551	1.09
$C(CH_3)_2$	-2.222	1.731	0.5667	0.823
$C(CF_3)_2$	-2.784	1.733	0.9895	1.12
C_6H_5	-3.012	1.860	0.382	0.90

Table 6.5. Binding energies, X-P bond lengths, Δe values, and band gaps for various methylene-related species adducted with phosphine, PH_3.

Adduct	E_b (eV)	R_{X-P} (Å)	Δe
CH_2PH_3	-3.342	1.661	0.8112
CF_2PH_3	-0.2199	2.056	0.3165
CCl_2PH_3	-0.9745	1.661	0.9356
CBr_2PH_3	-1.144	1.747	0.8921
$C(CH_3)_2PH_3$	-1.8502	1.511	0.8654
$C(CF_3)_2PH_3$	-3.6470	1.476	1.0996

every methylene-related species in this section to be in the singlet state, even though this is not quite the ground state for methylene itself.

The binding energies, bond lengths, Δe values, and band gaps for methylene and its related species bound to phosphorene are shown in Table 6.4. As with borane, we also present similar data for the same species adducted with phosphine in Table 6.5. Methylene itself binds very strongly to the phosphorene surface with a -3.54 eV binding energy, stronger even than the -3.01 eV binding energy of the phenyl radical. We also find that methylene withdraws more than twice as much electron density as does the phenyl radical and nearly ten times as much as does borane, with a Δe value of 0.81. Unlike the phenyl radical and borane, however, the binding of methylene to the phosphorene surface results in a decrease in band gap rather than in increase.

We next explore a number of species related to methylene. Unsurprisingly, we find that the halide-substituted methylenes CF_2, CCl_2, and CBr_2 all bind more weakly to phosphorene, with their binding energies scaling in accordance with their hardness as Lewis acids. Surprisingly, however, we find that the addition these electron-withdrawing groups actually results in a decrease

in Δe rather than an increase, perhaps due to weaker binding. Thus, methylene is a more attractive candidate than any of these halide-substituted variants.

Next, we compare these results to those obtained with $C(CH_3)_2$ and $C(CF_3)_2$. We find that $C(CH_3)_2$ binds less strongly to phosphorene than does methylene and also, has a lower Δe value. This is likely due to $C(CH_3)_2$ being a harder Lewis acid than methylene as well as the methyl groups being electron-donating rather than electron-withdrawing. $C(CF_3)_2$, the methylene analogue to the interesting $B(CF_3)_3$ species, is more promising. Its binding energy is not as high as that of methylene, but it is still quite high at -2.78 eV, and it withdraws even more electron density, with a Δe value of 0.99. Also, perhaps most significantly, the binding of $C(CF_3)_2$ to the phosphorene surface results in a substantial increase in band gap, rather than a decrease.

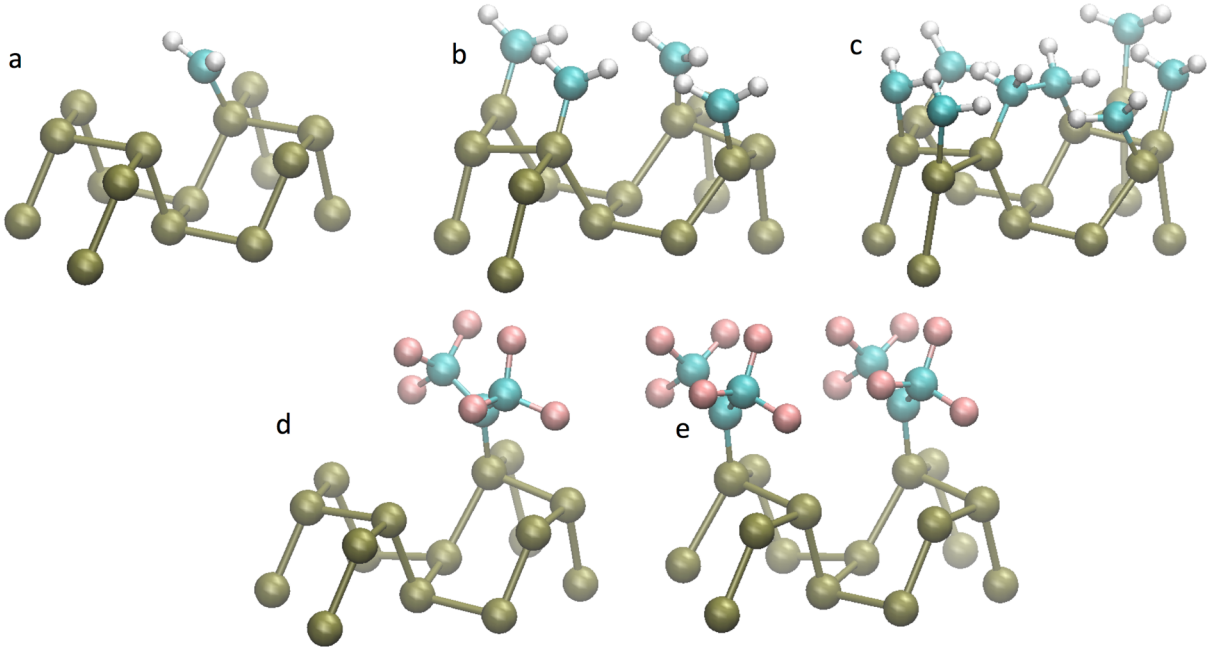

Figure 6.3. The phosphorene monolayer with (a) one, (b) four, and (c) eight methylenes adsorbed per P_{16} unit cell, as well as (d) one and (e) two $C(CF_3)_2$ adsorbates per P_{16} unit cell.

In adducts with phosphine, we find that for nearly every methylene-related species, including methylene itself, binding to phosphine is weaker than to phosphorene. The only Lewis acid in this section that binds more strongly to phosphine than to phosphorene is $C(CF_3)_2$, which, as in the case of its borane-based counterpart, is likely due to steric interactions between the CF_3 substituents and the phosphorene monolayer. Interestingly, we find that while Δe is smaller for the CF_2 phosphine adduct than the CF_2 phosphorene adduct, Δe is larger for nearly every other substituted methylene phosphine adduct.

Finally, as with the borane species, we consider the effects of surface coverage. Methylene is even smaller than borane, and it is possible to fit as many as eight methylene adsorbates into one unit cell in our model. Again, as before, we consider only binding to one of the two sides of the phosphorene monolayer, which limits us to eight methylenes. $C(CF_3)_2$ is also small enough that we can fit two on a single unit cell. The results of this study are shown in Table 6.6, with the various coverages illustrated in Figure 6.3. As methylene surface coverage increases from one to four per unit cell, we find that both binding energy per adsorbate and Δe per adsorbate hold relatively steady, while the overall Δe of the system increases dramatically, from 0.81 to 3.11, which suggests that methylene is capable of very substantial p-type doping. However, we also find that the band gap of the system decreases from 0.83 eV with one methylene adsorbate to 0.35 eV with four. When coverage increases from four to eight, binding energy per adsorbate actually increases, perhaps due to stabilizing interactions between neighboring carbon atoms. However, Δe per adsorbate drops by more than half, from 0.79 e to 0.38 e, and the band gap of the system drops even further, from 0.35 eV to 0.25 eV. In addition, with eight methylene molecules adsorbed the phosphorene layer begins to distort noticeably, which may have a highly detrimental effect on the semiconductor performance of phosphorene.

Table 6.6. Comparison of binding and electron transfer properties of methylene and $C(CF_3)_2$ different surface concentrations, along with the pristine phosphorene monolayer.

	E_b (eV) per adsorbate	Δe per adsorbate	Δe (total)	Band gap (eV)
Pristine	–	–	–	0.89
One CH_2	-3.535	0.8112	0.8112	0.83
Four CH_2s	-3.328	0.7781	3.1124	0.35
Eight CH_2s	-4.036	0.3792	3.0336	0.25
One $C(CF_3)_2$	-2.784	0.9895	0.9895	1.12
Two $C(CF_3)_2$s	-2.651	0.8980	1.796	1.09

$C(CF_3)_2$ offers a less destructive alternative to methylene. It cannot reach high enough surface concentrations to distort the structure of phosphorene, and it has been shown to increase rather than decrease the system band gap. When the surface concentration of $C(CF_3)_2$ is increased from one to two, we see that binding energy per adsorbate and Δe per adsorbate decrease only mildly, while band gap stays roughly the same. Only two $C(CF_3)_2$ atoms can bind per unit cell in our model, meaning that the total possible Δe per unit cell for $C(CF_3)_2$, 1.80 e, is barely more than half that of methylene, 3.11 e. Regardless, $C(CF_3)_2$ appears to be more efficient, is unlikely to distort the phosphorene structure, and increases rather than lowers the band gap of phosphorene.

6.4 Conclusions

To determine the suitability of various Lewis acids as candidates for passivation and functionalization of BP semiconductors, we performed periodic DFT calculations to predict the binding behavior and net charge transfer of a number of Lewis acids on a phosphorene monolayer,

particularly those related to borane and methylene. We found that binding energy between phosphorene and Lewis acids follows trends predicted by HSAB theory, although in some cases steric interactions between Lewis acids and the phosphorene surface also may play a role. We found that neither borane nor any of its related species bind particularly strongly to the phosphorene surface, and that of these the species that binds the most strongly, borane itself, barely withdraws any electron density from the phosphorene monolayer. We also found that methylene binds very strongly to phosphorene and results in significant electron withdrawal, but also that methylene binding results in a significant decrease in band gap and potential surface distortion. Finally, we found that bis(trifluoromethyl)methylene, $C(CF_3)_2$, also binds quite strongly, withdraws even more electron density than does methylene, and increases rather than decreases the phosphorene band gap, and is therefore the best candidate in this study.

References

(1) Kelly, K. L.; Coronado, E.; Zhao, L. L.; Schatz, G. C. *J. Phys. Chem. B* **2003**, *107*, 668-677.

(2) Mayer, K. M.; Hafner, J. H. *Chem. Rev.* **2011**, *111*, 3828-3857.

(3) Puišo, J.; Laurikaitienė, J.; Adlienė, D.; Prosyčevas, I. *Radiat. Prot. Dosim.* **2010**, *139*, 353-356.

(4) Saha, K.; Agasti, S. S.; Kim, C.; Li, X.; Rotello, V. M. *Chem. Rev.* **2012**, *112*, 2739-2779.

(5) Lu, G.; Hou, L.; Zhang, T.; Liu, J.; Shen, H.; Luo, C.; Gong, Q. *J. Phys. Chem. C* **2012**, *116*, 25509-25516.

(6) Lee, K. S.; El-Sayed, M. A. *J. Phys. Chem. B* **2006**, *110*, 19220-19225.

(7) Clavero, C. *Nat. Photon.* **2014**, *8*, 95-103.

(8) Li, J.; Cushing, S. K.; Bright, J.; Meng, F.; Senty, T. R.; Zheng, P.; Bristow, A. D.; Wu, N. *ACS Catal.* **2012**, *3*, 47-51.

(9) Yao, Y.; Kats, M. A.; Genevet, P.; Yu, N.; Song, Y.; Kong, J.; Capasso, F. *Nano Lett.* **2013**, *13*, 1257-1264.

(10) Dry, M. E. *Appl. Catal., A* **1996**, *138*, 319-344.

(11) Wang, W.; Wang, S.; Ma, X.; Gong, J. *Chem. Soc. Rev.* **2011**, *40*, 3703-3727.

(12) Lin, W.; Stocker, K. M.; Schatz, G. C. *J. Phys. Chem. C* **2016**, *120*, 23061-23068.

(13) Ryder, C. R.; Wood, J. D.; Wells, S. A.; Yang, Y.; Jariwala, D.; Marks, T. J.; Schatz, G. C.; Hersam, M. C. *Nat. Chem.* **2016**, *8*, 597-602.

(14) McQuarrie, D. A. *Quantum Chemistry*; University Science Books: Sausalito, CA, 2008;

(15) Burke, K.; Wagner, L. O. *Int. J. Quantum Chem.* **2013**, *113*, 96-101.

(16) Marques, M. A. L.; Gross, E. K. U. *Annu. Rev. Phys. Chem.* **2004**, *55*, 427-455.

(17) Payne, M. C.; Teter, M. P.; Allan, D. C.; Arias, T. A.; Joannopoulos, J. D. *Rev. Mod. Phys.*

1992, *64*, 1045-1097.

(18) Runge, E.; Gross, E. K. U. *Phys. Rev. Lett.* **1984**, *52*, 997-1000.

(19) Casida, M. E. *Recent Advances in Computational Chemistry* **1995**, *Volume 1*, 155-192.

(20) Linic, S.; Christopher, P.; Ingram, D. B. *Nat. Mater.* **2011**, *10*, 911-921.

(21) Ringe, E.; Langille, M. R.; Sohn, K.; Zhang, J.; Huang, J.; Mirkin, C. A.; Van, D., Richard P.; Marks, L. D. *J. Phys. Chem. Lett.* **2012**, *3*, 1479-1483.

(22) Zhang, Q.; Large, N.; Nordlander, P.; Wang, H. *J. Phys. Chem. Lett.* **2014**, *5*, 370-374.

(23) Jensen, L.; Aikens, C. M.; Schatz, G. C. *Chem. Soc. Rev.* **2008**, *37*, 1061-1073.

(24) Chakraborty, I.; Bag, S.; Landman, U.; Pradeep, T. *J. Phys. Chem. Lett.* **2013**, *4*, 2769-2773.

(25) Lee, A.; Andrade, G. F. S.; Ahmed, A.; Souza, M. L.; Coombs, N.; Tumarkin, E.; Liu, K.; Gordon, R.; Brolo, A. G.; Kumacheva, E. *J. Am. Chem. Soc.* **2011**, *133*, 7563-7570.

(26) Willets, K. A.; Van Duyne, R. P. *Annu. Rev. Phys. Chem.* **2007**, *58*, 267-297.

(27) Blaber, M. G.; Arnold, M. D.; Ford, M. J. *J. Phys. Condens. Matter* **2010**, *22*, 143201-143215.

(28) Blaber, M. G.; Engel, C. J.; Vivekchand, S. R.; Lubin, S. M.; Odom, T. W.; Schatz, G. C. *Nano Lett.* **2012**, *12*, 5275-5280.

(29) West, P. R.; Ishii, S.; Naik, G. V.; Emani, N. K.; Shalaev, V. M.; Boltasseva, A. *Laser Photon. Rev.* **2010**, *4*, 795-808.

(30) Zhang, J. Z. *J. Phys. Chem. Lett.* **2010**, *1*, 686-695.

(31) Abramczyk, H.; Brozek-Pluska, B. *Chem. Rev.* **2013**, *113*, 5766-5781.

(32) Turcheniuk, K.; Boukherroub, R.; Szunerits, S. *J. Mater. Chem. B* **2015**, *3*, 4301-4324.

(33) Lohse, S. E.; Murphy, C. J. *J. Am. Chem. Soc.* **2012**, *134*, 15607-15620.

(34) Hao, E.; Schatz, G. C. *J. Chem. Phys.* **2004**, *120*, 357-366.

(35) Jensen, T.; Kelly, L.; Lazarides, A.; Schatz, G. C. *J. Cluster Sci.* **1999**, *10*, 295-317.

(36) McMahon, J. M.; Wang, Y.; Sherry, L. J.; Van, D., Richard P.; Marks, L. D.; Gray, S. K.; Schatz, G. C. *J. Phys. Chem. C* **2009**, *113*, 2731-2735.

(37) Ross, M. B.; Schatz, G. C. *J. Phys. Chem. C* **2014**, *118*, 12506-12514.

(38) Mie, G. *Ann. Phys.* **1908**, *330*, 377-445.

(39) Wriedt, T. *Springer Ser. Opt. Sci.* **2012**, *169*, 53-71.

(40) Liebsch, A. *Phys. Rev. B* **1993**, *48*, 11317.

(41) Peña, O.; Pal, U. *Comput. Phys. Commun.* **2009**, *180*, 2348-2354.

(42) McMahon, J. M.; Schatz, G. C.; Gray, S. K. *Phys. Chem. Chem. Phys.* **2013**, *15*, 5415-5423.

(43) Draine, B. T.; Flatau, P. J. *J. Opt. Soc. Am. A* **1994**, *11*, 1491-1499.

(44) Hao, F.; Nordlander, P. *Chem. Phys. Lett.* **2007**, *446*, 115-118.

(45) Peng, S.; McMahon, J. M.; Schatz, G. C.; Gray, S. K.; Sun, Y. *Proc. Natl. Acad. Sci. U.S.A.* **2010**, *107*, 14530-14534.

(46) Fedrigo, S.; Harbich, W.; Buttet, J. *Phys. Rev. B* **1993**, *46*, 10706-10715.

(47) Aikens, C. M.; Li, S.; Schatz, G. C. *J. Phys. Chem. C* **2008**, *112*, 11272-12279.

(48) Madison, L. R.; Ratner, M. A.; Schatz, G. C. *QSCP Proc. XVIII* **2015**, 37-52.

(49) Guidez, E. B.; Aikens, C. M. *Phys. Chem. Chem. Phys.* **2014**, *16*, 15501-15509.

(50) Guidez, E. B.; Aikens, C. M. *Nanoscale* **2014**, *6*, 11512-11527.

(51) Guidez, E. B.; Aikens, C. M. *J. Phys. Chem. C* **2013**, *117*, 21466-21475.

(52) Brack, M. *Rev. Mod. Phys.* **1993**, *65*, 677-732.

(53) Kurkina, L. I.; Farberovich, O. V. *Phys. Rev. B* **1996**, *54*, 14791-14795.

(54) Beck, D. E. *Phys. Rev. B* **1987**, *35*, 7325-7333.

(55) Han, B.; Wang, E. *Anal. Bioanal. Chem.* **2012**, *402*, 129-138.

(56) Choi, S.; Dickson, R. M.; Yu, J. *Chem. Soc. Rev.* **2012**, *41*, 1867-1891.

(57) Liu, X.; Wang, F.; Aizen, R.; Yehezkeli, O.; Willner, I. *J. Am. Chem. Soc.* **2013**, *135*, 11832-11839.

(58) Zheng, K.; Yuan, X.; Goswami, N.; Zhang, Q.; Xie, J. *RSC Adv.* **2014**, *4*, 60581-60596.

(59) Wu, C. H.; Cook, J.; Emelianov, S.; Sokolov, K. *Adv. Funct. Mater.* **2014**, *24*, 6862-6871.

(60) Piccini, G.; Havenith, R. W. A.; Broer, R.; Stener, M. *J. Phys. Chem. C* **2013**, *117*, 17196-17204.

(61) Fihey, A.; Maurel, F.; Perrier, A. *J. Phys. Chem. C* **2014**, *118*, 4444-4453.

(62) Tlahuice-Flores, A.; Whetten, R. L.; Jose-Yacaman, M. *J. Phys. Chem. C* **2013**, *117*, 20867-20875.

(63) Lozano, X. L.; Barron, H.; Mottet, C.; Weissker, H. *Phys. Chem. Chem. Phys.* **2014**, *16*, 1820-1823.

(64) Bae, G. T.; Aikens, C. M. *J. Phys. Chem. C* **2015**, *119*, 23127-23137.

(65) Gieseking, R. L.; Ratner, M. A.; Schatz, G. C. *J. Phys. Chem. A* **2016**, *120*, 4542-4549.

(66) Aikens, C. M. *J. Phys. Chem. A* **2009**, *113*, 10811-10817.

(67) Aikens, C. M. *J. Phys. Chem. C* **2008**, *112*, 19797-19800.

(68) Zhu, M.; Aikens, C. M.; Hollander, F. J.; Schatz, G. C.; Jin, R. *J. Am. Chem. Soc.* **2008**, *130*, 5883-5885.

(69) Aikens, C. M. *J. Phys. Chem. Lett.* **2011**, *2*, 99-104.

(70) Malola, S.; Lehtovaara, L.; Häkkinen, H. *J. Phys. Chem. C* **2014**, *118*, 20002-20008.

(71) Weerawardene, K. L. D. M.; Aikens, C. M. *J. Am. Chem. Soc.* **2016**, *138*, 11202-11210.

(72) Wang, Z.; Senanayake, R.; Aikens, C. M.; Chen, W.; Tung, C. H.; Sun, D. *Nanoscale* **2016**, *8*, 18905-18911.

(73) Weissker, H.-C.; Mottet, C. *Phys. Rev. B* **2011**, *84*, 165443.

(74) Malola, S.; Lehtovaara, L.; Enkovaara, J.; Hakkinen, H. *ACS Nano* **2013**, *7*, 10263-10270.

(75) Bae, G.-T.; Aikens, C. M. *J. Phys. Chem. C* **2012**, *116*, 10356-10367.

(76) Kuisma, M.; Sakko, A.; Rossi, T. P.; Larsen, A. H.; Enkovaara, J.; Lehtovaara, L.; Rantala, T. T. *Phys. Rev. B* **2015**, *91*, 115431.

(77) Baseggio, O.; De Vetta, M.; Fronzoni, G.; Stener, M. *J. Phys. Chem. C* **2016**, *120*, 12773-12782.

(78) Johnson, H. E.; Aikens, C. M. *J. Phys. Chem. A* **2009**, *113*, 4445-4450.

(79) Vosko, S. H.; Wilk, L.; Nusair, M. *Can. J. Phys.* **1980**, *58*, 1200-1211.

(80) Gritsenko, O. V.; Schipper, P. R. T.; Baerends, E. J. *Chem. Phys. Lett.* **1999**, *302*, 199-207.

(81) Schipper, P. R. T.; Gritsenko, O. V.; van, G., S. J. A.; Baerends, E. J. *J. Chem. Phys.* **2000**, *112*, 1344-1352.

(82) Van Gisbergen, S. J. A.; Snijders, J. G.; Baerends, E. J. *Comput. Phys. Commun.* **1999**, *118*, 119-138.

(83) Rosa, A.; Baerends, E. J.; van Gisbergen, S. J. A.; van Lenthe, E. *J. Am. Chem. Soc.* **1999**, *121*, 10356-10365.

(84) van Lenthe, E.; Baerends, E. J.; Snijders, J. G. *J. Chem. Phys.* **1993**, 4597-4610.

(85) van Lenthe, E.; Baerends, E. J.; Snijders, J. G. *J. Chem. Phys.* **1994**, 9783-9792.

(86) van Lenthe, E.; Ehlers, A.; Baerends, E. J. *J. Chem. Phys.* **1999**, 8943-8953.

(87) Rodríguez, J. I.; Bader, R. F. W.; Ayers, P. W.; Michel, C.; Götz, A. W.; Bo, C. *Chem. Phys. Lett.* **2009**, *472*, 149-152.

(88) Rodríguez, J. I. *J. Comput. Chem.* **2013**, *34*, 681-686.

(89) te Velde, G.; Bickelhaupt, F. M.; Baerends, E. J.; Fonseca Guerra, C.; van Gisbergen, S. J.

A.; Snijders, J. G.; Ziegler, T. *J. Comput. Chem.* **2001**, *22*, 931-967.

(90) Fonseca Guerra, C.; Snijders, J. G.; te Velde, G.; Baerends, E. J. *Theor. Chem. Acc.* **1998**, *99*, 391-403.

(91) ADF2013, SCM, Theoretical Chemistry, Vrije Universiteit, Amsterdam, The Netherlands, http://www.scm.com.

(92) ADF2014, SCM, Theoretical Chemistry, Vrije Universiteit, Amsterdam, The Netherlands, http://www.scm.com.

(93) Walter, M.; Akola, J.; Lopez-Acevedo, O.; Jadzinsky, P. D.; Calero, G.; Ackerson, C. J.; Whetten, R. L.; Grönbeck, H.; Häkkinen, H. *Proc. Natl. Acad. Sci. U.S.A.* **2008**, *105*, 9157-9162.

(94) Joshi, C. P.; Bootharaju, M. S.; Alhilaly, M. J.; Bakr, O. M. *J. Am. Chem. Soc.* **2015**, *137*, 11578-115781.

(95) Heaven, M. W.; Dass, A.; White, P. S.; Holt, K. M.; Murray, R. W. *J. Am. Chem. Soc.* **2008**, *130*, 3754-3755.

(96) Pei, Y.; Gao, Y.; Shao, N.; Zeng, X. C. *J. Am. Chem. Soc.* **2009**, *131*, 13619-13621.

(97) Ning, C. G.; Xiong, X. G.; Wang, Y. L.; Li, J.; Wang, L. S. *Phys. Chem. Chem. Phys.* **2012**, *14*, 9323-9329.

(98) Jiang, D.; Walter, M. *Nanoscale* **2012**, *4*, 4234-4239.

(99) MacDonald, M. A.; Zhang, P.; Qian, H.; Jin, R. *J. Phys. Chem. Lett.* **2010**, *1*, 1821-1825.

(100) Jiang, D. *Chem. Eur. J.* **2011**, *17*, 12289-12293.

(101) Yang, H.; Wang, Y.; Huang, H.; Gell, L.; Lehtovaara, L.; Malola, S.; Häkkinen, H.; Zheng, N. *Nat. Commun.* **2013**, *4*, 1-8.

(102) Desireddy, A.; Conn, B. E.; Guo, J.; Yoon, B.; Barnett, R. N.; Monahan, B. M.; Kirschbaum,

K.; Griffith, W. P.; Whetten, R. L.; Landman, U.; Bigioni, T. P. *Nature* **2013**, *501*, 399-402.

(103) Bernadotte, S.; Evers, F.; Jacob, C. R. *J. Phys. Chem. C* **2013**, *117*, 1863-1878.

(104) Casanova, D.; Matxain, J. M.; Ugalde, J. M. *J. Phys. Chem. C* **2016**, *120*, 12742-12750.

(105) Krauter, C. M.; Bernadotte, S.; Jacob, C. R.; Pernpointner, M.; Dreuw, A. *J. Phys. Chem. C* **2015**, *119*, 24564-24573.

(106) Gieseking, R. L.; Ratner, M. A.; Schatz, G. C. *J. Phys. Chem. A* **2016**, *120*, 9324-9329.

(107) Gieseking, R. L.; Ratner, M. A.; Schatz, G. C. *J. Phys. Chem. A* **2016**, *120*, 9878-9885.

(108) Gieseking, R. L.; Ratner, M. A.; Schatz, G. C. *Farad. Discuss.* **2017**.

(109) Gieseking, R.; Ratner, M. A.; Schatz, G. C. *Farad. Discuss.* **2017**.

(110) Habteyes, T. G.; Dhuey, S.; Kiesow, K. I.; Vold, A. *Opt. Express* **2013**, *21*, 21607-21617.

(111) Hastings, S. P.; Swanglap, P.; Qian, Z.; Fang, Y.; Park, S. J.; Link, S.; Engheta, N.; Fakhraai, Z. *ACS Nano* **2014**, *8*, 9025-9034.

(112) Yong, Z.; Lei, D. Y.; Lam, C. H.; Wang, Y. *Nanoscale Res. Lett.* **2014**, *9*.

(113) Lee, H. C.; Li, C. T.; Chen, H. F.; Yen, T. J. *Opt. Lett.* **2015**, *40*, 5152-5155.

(114) ADF2016, SCM, Theoretical Chemistry, Vrije Universiteit, Amsterdam, The Netherlands, http://www.scm.com.

(115) Leeuwen, R. V.; Baerends, E. J. *Phys. Rev. A* **1994**, *49*, 2421-2431.

(116) Perdew, J. P.; Burke, K.; Ernzerhof, M. *Phys. Rev. Lett.* **1996**, *77*, 3865-3868.

(117) Guidez, E. B.; Aikens, C. M. *Nanoscale* **2012**, *4*, 4190-4198.

(118) López-Lozano, X.; Barron, H.; Mottet, C.; Weissker, H. C. *Phys. Chem. Chem. Phys.* **2014**, *16*, 1820-1823.

(119) Ashwell, A. P.; Ratner, M. A.; Schatz, G. C. *Advances in Quantum Chemistry* **2017**, *75*, 117-145.

(120) Alhilaly, M. J.; Bootharaju, M. S.; Joshi, C. P.; Besong, T. M.; Emwas, A. H.; Juarez-Mosqueda, R.; Kaappa, S.; Malola, S.; Adil, K.; Shkurenko, A.; Häkkinen, H.; Eddaoudi, M.; Bakr, O. M. *J. Am. Chem. Soc.* **2016**, *138*, 14727-14732.

(121) Juarez-Mosqueda, R.; Kaappa, S.; Malola, S.; Häkkinen, H. J. *J. Phys. Chem. C* **2016**, *121*, 10698-10705.

(122) Dry, M. E. *J. Chem. Technol. Biotechnol.* **2002**, *77*, 43-50.

(123) Lapidus, A. L.; Gaidai, N. A.; Nekrasov, N. V.; Tishkova, L. A.; Agafonov, Y. A.; Myshenkova, T. N. *Pet. Chem.* **2007**, *47*, 91-98.

(124) Marwood, M.; Doepper, R.; Renken, A. *Appl. Catal., A* **1997**, *151*, 223-246.

(125) Dombek, B. D. *Adv. Catal.* **1983**, *32*, 325-416.

(126) West, N. M.; Miller, A. J. M.; Labinger, J. A.; Bercaw, J. E. *Coord. Chem. Rev.* **2011**, *255*, 881-898.

(127) Song, Q.; Xiao, R.; Li, Y.; Shen, L. *Ind. Eng. Chem. Res.* **2008**, *47*, 4349-4357.

(128) Wang, J.; Kawazoe, Y.; Sun, Q.; Chan, S.; Su, H. *Surf. Sci.* **2016**, *645*, 30-40.

(129) Goodman, D. W. *Acc. Chem. Res.* **1984**, *17*, 194-200.

(130) Rostrup-Nielsen, J. R. *Volume 5* **1983**, *Catalysis, Science and Technology*, 1-117.

(131) Fajín, J. L. C.; Gomes, J. R. B.; Cordeiro, M. N. D. S. *J. Phys. Chem. C* **2015**,

(132) Remediakis, I. N.; Abild-Pedersen, F.; Nørskov, J. K. *J. Phys. Chem. B* **2004**, *108*, 14535-14540.

(133) Andersson, M. P.; Abild-Pederson, F.; Remediakis, I. N.; Bligaard, T.; Jones, G.; Engbaek, J.; Lytken, O.; Horch, S.; Nielsen, J. H.; Sehested, J.; Rostrup-Nielsen, J. R.; Nørskov, J. K.; Chorkendorff, I. *J. Catal.* **2008**, *255*, 6-19.

(134) Roiaz, M.; Monachino, E.; Dri, C.; Greiner, M.; Knop-Gericke, A.; Schlögl, R.; Comelli, G.;

Vesselli, E. *J. Am. Chem. Soc.* **2016**, *138*, 4146-4154.

(135) Johnson, A. D.; Daley, S. P.; Utz, A. L.; Ceyer, S. T. *Science* **1992**, *257*, 223.

(136) Maynard, K. J.; Johnson, A. D.; Daley, S. P.; Ceyer, S. T. *Faraday Discuss. Chem. Soc* **1991**, *91*, 437-449.

(137) Johnson, A. D.; Maynard, K. J.; Daley, S. P.; Yang, Q. Y.; Ceyer, S. T. *Phys. Rev. Lett.* **1991**, *67*, 927-930.

(138) Ceyer, S. T. *Acc. Chem. Res.* **2001**, *34*, 737-744.

(139) Bürgi, T.; Trautman, T. R.; Gostein, M.; Lahr, D. L.; Haug, K. L.; Ceyer, S. T. *Surf. Sci.* **2002**, *501*, 49-73.

(140) Peng, G.; Sibener, S. J.; Schatz, G. C.; Mavrikakis, M. *Surf. Sci.* **2012**, *606*, 1050-1055.

(141) Peng, G.; Sibener, S. J.; Schatz, G. C.; Ceyer, S. T.; Mavrikakis, M. *J. Phys. Chem. C* **2012**, *116*, 3001-3006.

(142) Kresse, G.; Furthmüller, J. *Phys. Rev. B* **1996**, *54*, 11169-11186.

(143) Kresse, G.; Furthmüller, J. *Comp. Mat. Sci.* **1996**, *6*, 15-50.

(144) Perdew, J. P.; Burke, K.; Ernzerhof, M. *Phys. Rev. Lett.* **1996**, *77*, 3865-3868.

(145) Blöchl, P. E. *Phys. Rev. B* **1994**, *50*, 17953-17979.

(146) Kresse, G.; Joubert, D. *Phys. Rev. B* **1999**, *59*, 1758-1775.

(147) Henkelman, G.; Jónsson, H. *J. Chem. Phys.* **2000**, *113*, 9978-9985.

(148) Henkelman, G.; Uberuaga, B. P.; Jónsson, H. *J. Chem. Phys.* **2000**, *113*, 9901-9904.

(149) Monkhorst, H. J.; Pack, J. D. *Phys. Rev. B* **1976**, *13*, 5188-5192.

(150) Studt, F.; Abild-Pedersen, F.; Wu, Q.; Jensen, A. D.; Temel, B.; Grunwaldt, J. D.; Nørskov, J. K. *J. Catal.* **2012**, *293*, 51-60.

(151) Kou, L.; Chen, C.; Smith, S. C. *J. Phys. Chem. Lett.* **2015**, *6*, 2794-2805.

(152) Ling, X.; Wang, H.; Huang, S.; Xia, F.; Dresselhaus, M. S. *Proc. Natl. Acad. Sci. U.S.A.* **2015**, *112*, 4523-4530.

(153) Bridgman, P. W. *J. Am. Chem. Soc.* **1914**, *36*, 1344-1363.

(154) Li, L.; Yu, Y.; Ye, G. J.; Ge, Q.; Ou, X.; Wu, H.; Feng, D.; Chen, X. H.; Zhang, Y. *Nat. Nanotechnol.* **2014**, *9*, 372-377.

(155) Rodin, A. S.; Carvalho, A.; Neto, A. H. C. *Phys. Rev. Lett.* **2014**, *112*, 176801.

(156) Li, L.; Kim, J.; Jin, C.; Ye, G. J.; Qiu, D. Y.; da Jornada, F. H.; Shi, Z.; Chen, L.; Zhang, Z.; Yang, F.; Watanabe, K.; Taniguchi, T.; Ren, W.; Louie, S. G.; Chen, X. H.; Zhang, Y.; Wang, F. *Nat. Nanotechnol.* **2017**, *12*, 21-26.

(157) Das, S.; Zhang, W.; Demarteau, M.; Hoffmann, A.; Dubey, M.; Roelofs, A. *Nano Lett.* **2014**, *14*, 5733-5739.

(158) Cho, K.; Yang, J.; Lu, Y. *J. Mater. Res.* **2017**, 1-9.

(159) Wood, J. D.; Wells, S. A.; Jariwala, D.; Chen, K. S.; Cho, E.; Sangwan, V. K.; Liu, X.; Lauhon, L. J.; Marks, T. J.; Hersam, M. C. *Nano Lett.* **2014**, *14*, 6964-6970.

(160) Staubitz, A.; Robertson, A. P. M.; Sloan, M. E.; Manners, I. *Chem. Rev.* **2010**, *110*, 4023-4078.

(161) Pearson, R. G. *J. Am. Chem. Soc.* **1963**, *85*, 3533-3539.

(162) Pearson, R. G. *Inorg. Chim. Acta.* **1995**, *240*, 93-98.

(163) Pearson, R. G. *J. Chem. Sci.* **2005**, *117*, 369-377.

(164) Grimme, S.; Antony, J.; Ehrlich, S.; Krieg, H. *J. Chem. Phys.* **2010**, *132*, 154104.

(165) Bader, R. F. W. *Atoms in Molecules - A Quantum Theory*; Oxford University Press: Oxford, UK, 1990;

(166) Henkelman, G.; Arnaldsson, A.; Jónsson, H. *Comp. Mat. Sci.* **2006**, *36*, 354-360.

(167) Sanville, E.; Kenny, S. D.; Smith, R.; Henkelman, G. *J. Comput. Chem.* **2007**, *28*, 899-908.

(168) Tang, W.; Sanville, E.; Henkelman, G. *J. Phys. Condens. Matter* **2009**, *21*, 084204.

(169) Plumley, J. A.; Evanseck, J. D. *J. Phys. Chem. A* **2009**, *113*, 5985-5992.

(170) Kirmse, W. *Angew. Chem. Int. Ed. Engl.* **2003**, *42*, 2117-2119.

Appendix A

Original Research Proposal: Modeling the Effects of Nitrate Spectator Ions on NaCl Nucleation

A.1 Abstract

The presence of nitrate anions in marine aerosol particles suppresses nucleation of NaCl, overall resulting in an increase in aqueous surface area in the atmosphere upon which heterogeneous chemistry can occur. We propose to study the mechanism by which nitrate anions affect NaCl nucleation in aqueous solution through the use of molecular dynamics (MD) simulations. In particular, we will study growth and structure of NaCl clusters in solution in the presence of some spectator ion, and we will observe how different spectator ions, including nitrate, alter cluster growth and behavior. The elucidation of the mechanism by which nitrate affects NaCl nucleation will lead to a greater understanding of the role of human-made pollutants on atmospheric chemistry, as well as a greater understanding of nucleation processes in general.

A.2 Background

Sea salt aerosol particles make up a substantial portion of the various aerosol particles present in the troposphere. They are typically generated via sea spray, and are quickly swept up into the atmosphere.[A1] Sea salt aerosols contain a mixture of electrolytes representative of those present at the upper levels of the oceans, primarily Na^+ and Cl^-, although Mg^{2+}, SO_4^{2-}, Ca^{2+}, Br^-, and K^+ are present in nontrivial amounts as well.[A2] NO_3^- anions, which will be a focus of this study, are typically a very small portion of the ions present in seawater, but reactions on aerosol surfaces between NO_x pollutants and NaCl can lead to both expulsion of Cl in various gaseous forms and an increase in NO_3^- concentration within the aerosol.[A3]

The phase of a sea salt aerosol particle is dependent on both the relative humidity of the surrounding air and the salt composition of the particle. Importantly, the rates of many atmospheric reactions that occur on aerosol surfaces depend strongly on aerosol phase, with reactions typically occurring much more quickly on aqueous surfaces. As sea salt aerosols come from the ocean they begin in the aqueous phase, eventually transitioning to the solid phase as they rise in the atmosphere and encounter lower relative humidities. The transition of an aerosol particle from the aqueous to the solid phase, called efflorescence, is a kinetically-limited process that depends on successful salt nucleation, typically beginning with nucleation of NaCl in the case of sea salt aerosols. In general, the presence of salts other than NaCl suppresses efflorescence, requiring a greater degree of supersaturation before nucleation can successfully occur.[A4,A5]

Nitrate anions are particularly effective in suppressing efflorescence.[A5,A6] The effect of the presence of nitrate ions on efflorescence in sea salt aerosols has been modeled using a semiempirical model built on classical nucleation theory,[A5] but the exact mechanism by which NO_3^- affects NaCl nucleation is not known.

A.3 Scientific Objectives

The aim of this research is to develop a fundamental understanding of the impact of spectator ions on the nucleation of NaCl. Specifically, we are interested in understanding the mechanism by which nitrate anions impede the nucleation of NaCl. This greater understanding will aid in the development and application of more complex nucleation models to predict the effects of increased nitrate concentration on aerosol particles in the atmosphere and, ultimately, on the Earth as a whole.

It is hypothesized that nitrate anions disrupt the NaCl nucleation process by binding to NaCl clusters as they grow. As $NaNO_3$ and NaCl have different crystal structures, the presence of NO_3^- on a NaCl cluster should impede further growth on that area of the cluster. We hypothesize as well that Br^- anions and K^+ cations are not so disruptive, as NaBr and KCl also have a rock salt structure. Thus, NaCl should be able to continue to grow around any Br^- and K^+ defects, although perhaps at a reduced rate.

A.4 Previous Work

A simple theory for homogeneous nucleation was first put forth by Willard Gibbs in 1877, who described the free energy of a droplet of liquid in terms of surface tension between the liquid and gas phases.[A7] This model has been used by analogy to describe nucleation of solid crystals from ions in supersaturated solutions. The solid phase is more stable than the liquid phase, but the creation of a solid cluster inside the liquid phase introduces a solid/liquid interface, introducing a free energy that is proportional to the surface area of the cluster. As a result, small clusters typically do not last long and return to the liquid phase quickly. As cluster size increases the surface-to-

volume ratio falls, and above some critical cluster radius the decrease in free energy from the solid-to-liquid transformation becomes more significant than the increase in free energy from the solid/liquid interface. Once this condition is met, the cluster typically grows in size unabated until the phase transition is complete.[A8]

Molecular dynamics simulations have been widely used to study nucleation. One of the first such studies was published in 2004 by Zahn,[A9] the results of which suggested that the "centers of stability" of early NaCl clusters are desolvated Na^+ ions octahedrally coordinated with six Cl^- ions. The study of clusters, rather than solely of large-scale nucleation events, allows researchers to derive insight into the nucleation process from MD simulations, as full-scale nucleation events occur very rarely.

Further insight was gained in 2008, when Nahtigal et al.[A10] ran molecular dynamics simulations of supersaturated NaCl solutions with much longer simulation times than those in the study of Zahn. Nahtigal et al. found that the critical cluster size for nucleation dropped with increasing density of Na^+ and Cl^- ions, that cluster-cluster fusion events appeared play a significant role in NaCl nucleation, and that initially-formed clusters are relatively amorphous rather than highly ordered. This last result, that of amorphous clusters, was expanded upon by the work of Cakraborty and Patey,[A11] who demonstrated a two-step mechanism for NaCl nucleation from solution. The first step involves a large increase in local concentration of Na^+ and Cl^- via some fluctuation, and the second step then involves spatial ordering of those ions into the appropriate crystal structure.

Zimmermann et al.[A12] combined data from molecular dynamics simulations with classical nucleation theory to study NaCl nucleation rates and attachment kinetics in supersaturated NaCl solutions using a seeding model. The authors found that the nucleation rate is limited not by the

rate of diffusion of ions through the solution but by the rate of desolvation of those ions. Notably, Zimmermann et al. also found nucleation rates of NaCl far higher than those measured experimentally, by as many as 30 orders of magnitude. The origins of this discrepancy are unclear, with several possible sources, including possible errors or false assumptions in both theory and experiment.

Recently, Lanaro and Patey[A13] published a paper in which they studied NaCl nucleation by observing the formation, growth, and dissolution of NaCl clusters in a supersaturated solution. Lanaro and Patey ran a series of MD simulations on very large systems, comprising roughly 25,000 water molecules and 14,000 ions, and did so for a very long time, roughly 500 ns. They were able to determine a relationship between the crystallinity of NaCl clusters – that is, how close in structure each cluster is to the NaCl bulk crystal structure – and NaCl cluster growth and lifetime. How long a cluster holds together in solution, as well as the propensity of that cluster to grow, are directly related to the probability that that cluster will undergo nucleation. As such, the authors were able to prove the importance of cluster structure to the probability of nucleation.

Researchers have also employed MD simulations to study nucleation in other contexts. Pereyra et al.[A14] studied the nucleation of ice crystals in supercooled water with varying initial conditions and established the quantitative relationship between system temperature and the critical radius for an ice crystal necessary for nucleation to proceed. In another example, Salvalaglio et al.[A15] have recently studied cluster growth in urea from aqueous solution, finding that urea nucleation appears to occur in a two-step process similar to that of NaCl and that two separate polymorphs of crystal urea compete with one another.

A.5 Proposed Research

To achieve the scientific objectives of this project, we will employ classical MD simulations. In general, we aim to gain a better fundamental understanding of the role of spectator ions in the nucleation of NaCl. Specifically, we aim to better understand the mechanism by which NO_3^- spectator ions impede nucleation of NaCl, and how they do so to a greater degree than other monovalent anions such as Br^-. We will do this by modeling the growth, lifetime, and crystallinity of NaCl clusters[A13] in seeded multicomponent solutions in which NaCl is supersaturated.

We will run a large number of MD simulations with varying initial conditions. We expect to run all MD simulations using the GROMACS software, which is easily run on GPUs and therefore more efficient than CPU-based MD calculations. One approach to the problem of observing a rare event in a time-limited MD simulation, which was employed by Lanaro and Patey in their study of NaCl nucleation in a single-component solution and discussed above,[A13] is to start with a very large number of ions and water molecules (roughly 25,000 water molecules and 14,000 ions in their study). These ions and molecules begin in randomized but relaxed initial positions, and they then take part in an MD simulation that runs for a very long time (roughly 500 ns with 0.04 ns time steps). The large system size and long simulation time are in this case both necessary to ensure that a large number of NaCl clusters are formed and thereafter studied. While this approach gives a great deal of information and allows one to study the rate of cluster formation, it is also extremely expensive computationally. Our research will necessitate the use of force fields that can accurately describe interactions between not just two but three types of ions. To employ the methodology described above using these more complex force fields would almost certainly be impossible due to the computational cost.

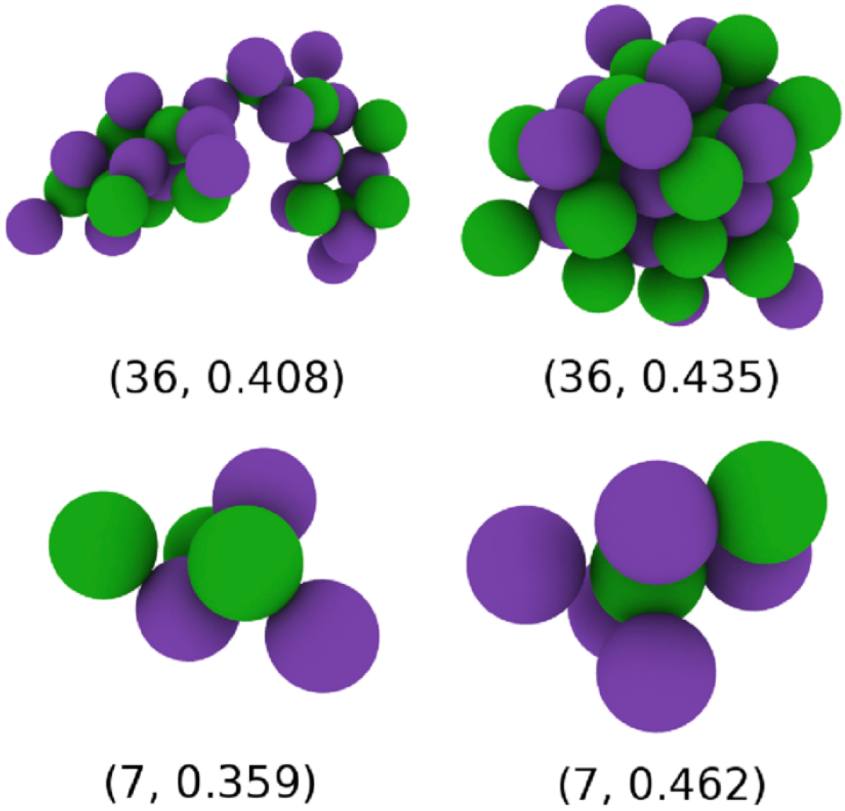

Figure A.1. Examples of clusters of different sizes and crystallinities, with size and crystallinity given below each cluster. Clusters with higher crystallinity values, in particular the example shown at top right, tend to be more compact, while those with lower crystallinities have more elongated structures, such as that at top left. Reproduced with permission from Lanaro, G.; Patey, G. N. *J. Phys. Chem. B* **2016**, 120, 9076-9087. Copyright 2016 American Chemical Society.

Instead, we will study much smaller systems at much shorter timescales using a seeding method. In a seeding method, the initial system already contains one or more cluster seeds. These may be small NaCl clusters of maybe 5 to 10 atoms, or they may be proto-clusters of 2 or 3 atoms. They also may or may not have an above-average concentration of Na^+ and Cl^- ions in their immediate vicinity. These cluster seeds greatly increase the likelihood of cluster formation and growth, allowing us to use much smaller systems and to run simulations for much less time and

still see at least one event of interest. We will determine system size, simulation time, and the ideal seeding method to use through extensive testing.

The results of each simulation will be analyzed by identification and characterization of clusters. Clusters can be identified by analyzing the bond order parameters of each ion in solution to determine whether they are in solid-like or liquid-like environments. This involves not just the density of ions but also how crystalline their arrangement relative to each other is. We can then determine whether or each solid-like ion is part of a cluster by looking at the number of nearby solid-like ions and their distances to the ion in question, and we can then group these ions into specific clusters. Then, we need to connect clusters in different time steps to one another based on the number of ions they have in common and how close in time they are to one another. With all this done, we will be able to determine cluster properties such as size and crystallinity, which is the average bond order parameter for the ions in a cluster. Crystallinity is in this case essentially a metric of how close to the NaCl rock salt structure a given cluster is, and will allow us to differentiate easily between amorphous and ordered clusters. We will be able to study both the effects of system composition on cluster crystallinity and the effects of cluster crystallinity on cluster growth and lifetime.

In addition to this study of cluster properties, we will also study the environment of each cluster. Specifically, we will develop and apply a metric to describe the relative concentrations of the various ions around each cluster, which will give us insight into the effects of various ions on cluster growth and lifetime. Finally, we will account for the possible presence of ions other than Na^+ and Cl^- in clusters, and observe particularly how this presence affects cluster growth.

In applying this methodology, we will first have to determine the suitability of given force fields and water models for the systems we intend to study. As discussed above, a number of

studies have employed molecular dynamics to study multicomponent solutions, usually in the context of ion behavior at the air/water interface. The force fields used in this studies are an ideal starting point, specifically those employed in the work of Richards-Henderson et al., in which multicomponent solutions of NaCl, NaBr, and $NaNO_3$ were studied. Small "toy" systems will be tested first with short simulation times, both seeded and unseeded, to observe the performance of various force fields. Our first priority will be to identify sets of force fields and water models to optimally describe NaCl/NaBr and NaCl/$NaNO_3$ solutions, with NaCl/KCl a lower priority case that may be revisited later. From this data we will choose our preferred force fields and water models for each solution.

Once force fields and water models are chosen, we will continue to work with small, seeded systems and short simulations to determine optimal parameters for cluster identification. First, we will need to choose a bond order parameter cutoff value. Ions with bond order parameter values above this cutoff will be considered to be in solid-like environments, and those below this cutoff will be considered to be in liquid-like environments. And next, we will need to determine cutoffs for cluster size (number of ions) and interionic distance. We will start with the values used by Lanaro and Patey for all three cutoffs and then determine the suitability of those particular cutoffs to the systems being studied. We will also experiment with system size and simulation time to determine just how large and long our systems and simulations can be while still maintaining a reasonable level of computational expense that allows for iteration.

Finally, after we have determined optimal force fields, water models, parameters, system size, and simulation length, we will begin running simulations aimed at producing usable data. We will first consider a supersaturated single-component solution of NaCl as a reference point. This will allow us to compare NaCl cluster behavior with and without spectator ions. In Lanaro and

Patey the mole fraction of NaCl most often considered was 0.22, more than two times greater than the experimental saturation mole fraction of NaCl of ~0.10. We will experiment with various degrees of supersaturation, but most likely we will use the 0.22 NaCl mole fraction value. Outside of the cluster seeds placed in each system, we will randomize the positions of the remaining ions and water molecules and then relax the system before beginning each simulation.

We will then run simulations of NaCl/NaBr and NaCl/$NaNO_3$ where the molar ratio of NaCl to NaBr/$NaNO_3$ is 1:0.1, 1:0.2, 1:0.3, 1:0.4, and 1:0.5. We will maintain the same degree of NaCl supersaturation as was present in the single-component NaCl solution, accounting for the reduced solubility resulting from the common ion effect. As before, ion and molecule positions outside of the cluster seeds will be randomized. This will lead to varying initial ionic environments for the cluster seeds, allowing us to study as well the impact of ionic environment on cluster behavior. For each mixture and ratio, we will aim to perform tens of simulations, the results of which will then be averaged to make up for the small system sizes and short simulation times. Of key interest will be the comparison between the effects of NO_3^- and Br^- anions.

As the initial ionic environments of the cluster seeds are likely to have a significant impact on our results, we will also run a few simulations at each mixture ratio with a longer timescale to observe how the ions in solution partition to or away from clusters over time. This will help us to determine how to set up the initial ionic environments of each cluster seed, as the use of a seeding method will require us to predetermine the ionic environment.

If the computational expense of the simulations is low enough, we may also vary the size of the cluster seeds in the initial state of each system. Small cluster seeds would allow us to study the early stages of cluster growth, but as the chance of the cluster either failing to grow or even breaking apart is likely quite high, a great many simulations may be required to obtain sufficient

data. Larger cluster seeds, even using clusters of 20 or more ions, would allow us to more clearly study the later stages of cluster growth, but we would also be studying in detail an event that may be quite rare. Thus, it would be ideal to study a range of cluster seed sizes.

Of particular interest would be the binding of ions other than Na^+ and Cl^- to the clusters, and how that binding affects cluster growth and lifetime. NaCl, NaBr, and KCl crystals all have rock salt structures, while $NaNO_3$ does not. NO_3^- anions may impede cluster growth to a greater degree than either K^+ or Br^- due to these incompatible crystal structures. If an NO_3^- anion joins a cluster of NaCl, it may effectively render growth on one side of the cluster impossible. This scenario may arise frequently in the simulations we will run, or it may come up barely if at all. If this does not happen frequently enough to be studied, we will run simulations in which we add at least one ion other than Na^+ or Cl^- to the side of a cluster seed in order to observe the effect on cluster behavior.

Finally, if time permits, we will also run studies on seeded and supersaturated single-component solutions of KCl, $NaNO_3$, and NaBr to study behavior of their own clusters in comparison with those of NaCl. It would also be particularly interesting to compare cluster behavior of $NaNO_3$ with the behaviors of NaBr and KCl. As NaCl, NaBr, and KCl are all rock salt structures while $NaNO_3$ can be either trigonal or rhombohedral, one would expect the relationship between cluster crystallinity and cluster growth and lifetime to differ between the two crystal structures.

A.6 Summary and Conclusions

In summary, we will use MD simulations to study the effects of spectator ions, and nitrate anions in particular, on the nucleation of NaCl. We will model the behavior of NaCl clusters in

seeded and supersaturated NaCl solutions with and without the presence of spectator ions and observe how spectator ions affect cluster growth and lifetime. Specifically, we will explore the ways in which nitrate anions interact with NaCl clusters and compare those interactions with those of Br^- and K^+ ions, and from our understanding of those interactions we will draw conclusions as to the mechanisms by which nitrate suppresses the nucleation of NaCl. This knowledge will lead to improved modeling and prediction of the impact of human-made pollutants on the rates of atmospheric chemistry.

A.7 References

(A1) O'Dowd, C. D.; Smith, M. H.; Consterdine, I. E.; Lowe, J. A. *Atmos. Environ.* **1997**, *31*, 73-80.

(A2) Kester, D. R.; Duedall, I. W.; Connors, D. N.; Pytkowicz, R. M. *Limnol. Oceanogr.* **1967**, *12*, 176-179.

(A3) Finlayson-Pitts, B. J.; Hemminger, J. C. *J. Phys. Chem. A* **2000**, *104*, 11463-11477.

(A4) Woods, E.; Chung, D.; Lanney, H. M.; Ashwell, B. A. *J. Phys. Chem. A* **2010**, *114*, 2837-2844.

(A5) Woods, E.; Heylman, K. D.; Gibson, A. K.; Ashwell, A. P.; Rossi, S. R. *J. Phys. Chem. A* **2013**, *117*, 4214-4222.

(A6) Hoffman, R. C.; Laskin, A.; Finlayson-Pitts, B. J. *J. Aerosol Sci.* **2004**, *35*, 869-887.

(A7) Sosso, G. C.; Chen, J.; Cox, S. J.; Fitzner, M.; Pedevilla, P.; Zen, A.; Michaelides, A. *Chem. Rev.* **2016**, *116*, 7078-7116.

(A8) Erdemir, D.; Lee, A. Y.; Myerson, A. S. *Acc. Chem. Res.* **2009**, *42*, 621-629.

(A9) Zahn, D. *Phys. Rev. Lett.* **2004**, *92*, 040801.

(A10) Nahtigal, I. G.; Zasetsky, A. Y.; Svishchev, I. M. *J. Phys. Chem. B* **2008**, *112*, 7537-7543.

(A11) Chakraborty, D.; Patey, G. N. *Chem. Phys. Lett.* **2013**, *587*, 25-29.

(A12) Zimmermann, N. E. R.; Vorselaars, B.; Quigley, D.; Peters, B. *J. Am. Chem. Soc.* **2015**, *137*, 13352-13361.

(A13) Lanaro, G.; Patey, G. N. *J. Phys. Chem. B* **2016**, *120*, 9076-9087.

(A14) Pereyra, R. G.; Szleifer, I.; Carignano, M. A. *J. Chem. Phys.* **2011**, *135*, 034508.

(A15) Salvalaglio, M.; Perego, C.; Giberti, F.; Mazzotti, M.; Parrinello, M. *Proc. Natl. Acad. Sci. U.S.A.* **2015**, *112*, E6-E14.